Analyses for a Modernized GNSS Radio Occultation Receiver

by

Erin R. Griggs

B.S., Colorado School of Mines, 2007

M.S., Colorado School of Mines, 2008

A thesis submitted to the

Faculty of the Graduate School of the

University of Colorado in partial fulfillment

of the requirements for the degree of

Doctor of Philosophy

Department of Aerospace Engineering Sciences

2015

UMI Number: 3704709

UMI®
Dissertation Publishing

UMI 3704709

ProQuest®

ProQuest LLC.
789 East Eisenhower Parkway
P.O. Box 1346
Ann Arbor, MI 48106 – 1346

This thesis entitled:
Analyses for a Modernized GNSS Radio Occultation Receiver
written by Erin R. Griggs
has been approved for the Department of Aerospace Engineering Sciences

_____
Prof. Dennis Akos

_____
Prof. Judah Levine

Date _____

The final copy of this thesis has been examined by the signatories, and we find that both the content and the form meet acceptable presentation standards of scholarly work in the above mentioned discipline.

Griggs, Erin R. (Ph.D., Aerospace Engineering Sciences)

Analyses for a Modernized GNSS Radio Occultation Receiver

Thesis directed by Prof. Dennis Akos

Global Navigation Satellite System (GNSS) radio occultation (RO) is a remote sensing technique that exploits existing navigation signals to make global, real-time observations of the Earth's atmosphere. A specialized RO receiver makes measurements of signals originating from a transmitter onboard a GNSS spacecraft near the Earth's horizon. The radio wave is altered during passage through the Earth's atmosphere. The changes in the received signals are translated to the refractivity characteristics of the intervening medium, which enable the calculation of atmospheric pressure, temperature, and humidity.

Current satellite missions employing GNSS RO have provided invaluable and timely information for weather and climate applications. Existing constellations of occultation satellites, however, are aging and producing fewer quality measurements. Replacement fleets of RO satellites are imperative to sustain and improve the global coverage and operational impact achieved by the current generation of RO satellites. This dissertation describes studies that facilitate the development of next generation RO receivers and satellite constellations. Multiple research efforts were conducted that aim to improve the quantity and quality of measurements made by a future satellite-based RO collection system.

These studies range in magnitude and impact, and begin with a receiver development study using ground-based occultation data. Future RO constellations and collection opportunities were simulated and autonomous occultation prediction and scheduling capabilities were implemented. Finally, a comprehensive study was conducted to characterize the stability of the GNSS atomic frequency standards. Oscillator stability for a subset of satellites in the GNSS was found to be of insufficient quality at timescales relevant to RO collections and would degrade the atmospheric profiling capabilities of an RO system utilizing these signals. Recommendations for a high-rate clock

correction network are proposed, which provides significant improvement to the fractional errors in the derived refractivity, pressure, and temperature values caused by the oscillator instabilities.

Dedication

This thesis is dedicated to my Fizeks Grandpa, for without his early inspiration, tutelage, and encouragement in my educational endeavors, I would not have found my passion for outer space.

Acknowledgements

There are a number of people without whom this thesis might not have been finished, and to whom I am greatly indebted. I would like to express my deepest appreciation for my committee chair, Professor Dennis Akos. He has continually pushed and stretched me beyond my limitations, but has always been in my corner to back me up. I would also like to thank Dr. E. Robert Kursinksi and Dr. Judah Levine for their invaluable input and continued guidance in the areas of radio occultation and oscillator stability. Thank you to my committee members, Professor Penina Axelrad and Professor George Born, for their support and expertise in all things GNSS and orbit determination.

My thanks to Chris McCormick and Broad Reach Engineering for their considerable support and invested interest in bettering humanity with scientific endeavors. I am greatly indebted to both the ARCS Foundation and the Colorado Space Business Roundtable for their generous support and great networking opportunities.

Thank you Staffan Backén, Elliot Barlow, and Jordan Riggs for your great company and assistance for the mountain-based collection campaigns. My thanks to William Diener, Stephan Esterhuizen, and Larry Young for your input, assistance, and allowing me to use your facilities at JPL for needed data collections. Many thanks to my family, especially Dan and Mary Griggs and Bonnie LaFleur, for proof reading my papers and patiently letting me practice my presentations for them.

And finally, thank you to my hockey family for keeping me sane.

Contents

Chapter

Tables

Table

Figures

Figure

Abbreviations

1WCP	One Way Carrier Phase
3CH	Three Cornered Hat
AD	Allan Deviation
AFS	Atomic Frequency Standard
AHM	Active Hydrogen Maser
C/A	Coarse Acquisition
C/N_0	Carrier to Noise Density Ratio
CDDIS	Crustal Dynamics Data Information System
CDMA	Code Division Multiple Access
CFS	Cesium Frequency Standard
CODE	Center for Orbit Determination in Europe
COSMIC	Constellation Observing System for Meteorology, Ionosphere, and Climate
COTS	Commercial Off-The-Shelf
CU	University of Colorado
DC	Direct Current
DS-SS	Direct-Sequence Spread Spectrum
ECEF	Earth-Centered, Earth-Fixed
ECI	Earth-Centered, Inertial
EKF	Extended Kalman Filter

FDMA	Frequency Division Multiple Access
FF	Flicker Frequency
FLL	Frequency-Locked Loop
GRAS	GNSS Receiver for Atmospheric Sounding
GLONASS	GLObalnaya NAvigatsionnaya Sputnikovaya Sistema
GNSS	Global Navigation Satellite System
GPS	Global Positioning System
ICD	Interface Control Document
ID	Identification
IF	Intermediate Frequency
IGOR	Integrated GPS Occultation Receiver
IGS	International GNSS Service
IOV	In-Orbit Validation
IRNSS	Indian Regional Navigation Satellite System
JPL	Jet Propulsion Laboratory
LEO	Low-Earth Orbit
LNA	Low Noise Amplifier
LOS	Line Of Sight
MAD	Modified Allan Deviation
MATLAB	MATrix LABoratory

MEO	Medium-Earth Orbit
NASA	National Aeronautics and Space Administration
NIST	National Institute of Standards and Technology
NOAA	National Oceanic and Atmospheric Administration
NWP	Numerical Weather Prediction
OD	Orbit Determination
OL	Open-Loop
PAD	Pre-filtered Allan Deviation
PHM	Passive Hydrogen Maser
PLL	Phase-Locked Loop
POD	Precise Orbit Determination
PRN	Pseudo-Random Noise
QZSS	Quasi-Zenith Satellite System
RF	Radio Frequency
RFI	Radio Frequency Interference
RFS	Rubidium Frequency Standard
RIC	Radial, In-track, Cross-track
RMS	Root Mean Square
RO	Radio Occultation
SDR	Software Defined Radio

SNR   Signal-to-Noise Ratio

SP3   Standard Product 3

STK   Systems (Satellite) Tool Kit

SVN   Satellite Vehicle Number

TKS   Time Keeping System

UCAR   University Corporation for Atmospheric Research

USRP   Universal Software Radio Peripheral

UTC   Coordinated Universal Time

VCXO   Voltage Controlled Crystal Oscillator

VSM   Variance Summation Method

WF   White Frequency

Chapter 1

INTRODUCTION

Timely, global atmospheric data sets are one of many requirements for the comprehensive models that interpret and predict weather and climate change. Observations of pressure, refractivity, temperature, and water vapor content in the lower layers of the atmosphere are key to a better understanding of the Earth's meteorological system. The spatial and temporal resolution of these measurements are critical to the quality of the models and future predictions. Therefore, timely and worldwide observations are necessary.

Presently, different measurement methods and systems are used to collect atmospheric data, including ground-based radars and radiosondes. These systems, however, lack global coverage and are subject to spatial and temporal inhomogeneity errors because of their irregular distribution [47]. Another effective data collection technique utilizes the atmospheric distortion to incoming radio signals to infer characteristics about the intervening atmosphere. Radio occultation (RO) refers to a sounding method in which a radio wave from a transmitter propagates through an intervening planetary atmosphere before arriving at the space-based receiver. The atmosphere causes perturbations to the known signal characteristics, which can be related to the vertical profiles of refractivity, pressure, temperature, and humidity of the intervening atmosphere [51, 92].

An RO observation profile consists of a sequence of carrier phase and amplitude observations of a known signal measured by a receiver over the course of an occultation episode. Current missions that employ RO, listed in Table 1.1, use receivers onboard low-Earth orbiting (LEO) spacecraft to observe signals from the Global Positioning System (GPS) satellites in medium-Earth orbit (MEO).

To perform GPS-based RO, the specialized receiver must capture raw GPS signal parameters for either real-time onboard RO data processing or transmission to ground stations for post-processing. Exploitation of existing signals (such as those from the GPS satellites) eliminates the development, launch, and operational costs of dedicated transmitters, greatly reducing the overall cost of an atmospheric profiling system. An illustration of a typical GPS RO event and the atmosphere values derived from the technique are shown in Figure 1.1.

Table 1.1: Previous and future occultation collection missions utilizing navigation signals and their respective launch dates.

Mission	Launch
GPS/Meteorology (GPS/MET)	1995
Challenging Minisatellite Payload (CHAMP)	2001
Satelite de Aplicaciones Cientificas-C (SAC-C)	2001
Gravity Recovery and Climate Experiment (GRACE)	2006
Constellation Observing System for Meteorology, Ionosphere, and Climate (FORMOSAT-3/COSMIC)	2006
MetOp-A	2006
TerraSAR-X	2007
Communications/Navigation Outage Forecasting System (C/NOFS)	2008
TanDEM-X	2010
MetOp-B	2012
Constellation Observing System for Meteorology, Ionosphere, and Climate 2 (FORMOSAT-7/COSMIC-2)	2015
Community Initiative for Continuous Earth Remote Observation (CICERO)	2015
Spire	2015
PlanetiQ	2016
MetOp-C	2018

GPS RO has become one of the most important data sets for numerical weather prediction [13]. It has proven to be valuable for hurricane forecasting, analysis of the atmospheric boundary layer, and ionospheric and space weather model testing [84]. As new constellations of navigation satellites emerge, new signals and satellites are available as possible sources of occultation measurements. Accuracy, resolution, and the global distribution of occultation measurements are
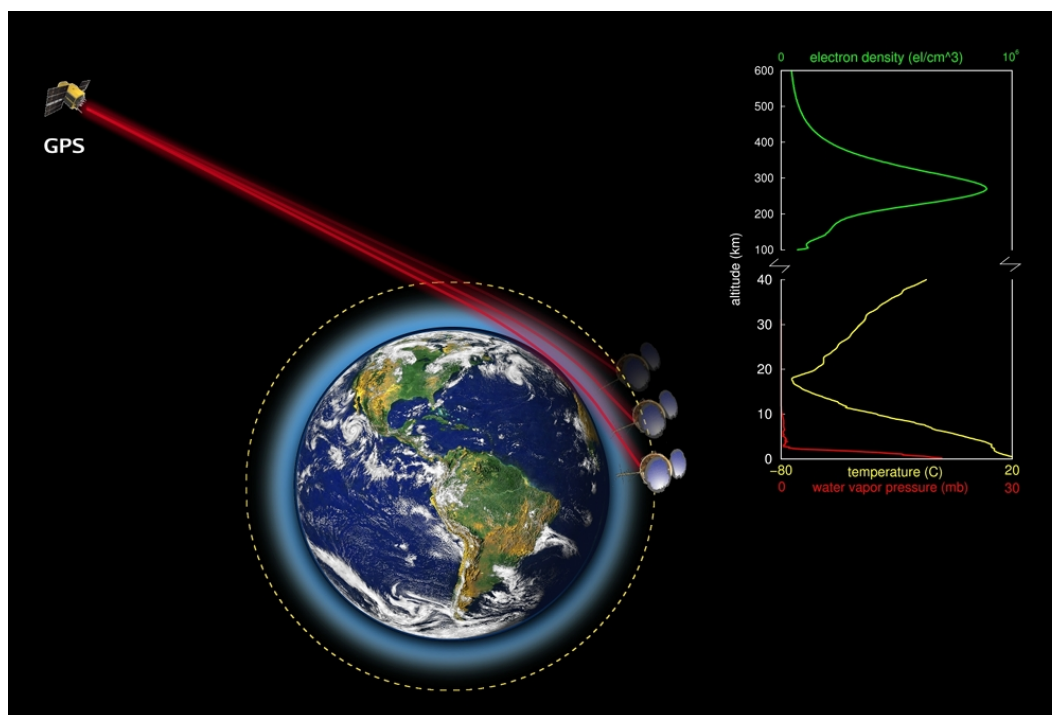
Figure 1.1: Visualization of a GPS RO event and derived atmospheric parameters as a function of altitude above the Earth's surface. Illustration reproduced from COSMIC Program Office [85].

key factors in the design of a RO system. The studies described in this thesis provide valuable insight for the development of a modernized space-based RO system capable of collecting higher fidelity signals thus enabling higher quality atmospheric data for climate and weather prediction applications.

1.1   History of Radio Occultation

1.1.1   Interplanetary Occultations

Remote sensing via occultation has been used by scientists for hundreds of years. In lieu of expensive chronometers, lunar occultations of distant stars were used for accurate time keeping at sea in the eighteenth century. More recently, the lunar limb was used to obtain diffraction patterns from quasars, as the fringe spacing and amplitude of the diffraction pattern provided unique information of the angular distribution of radiant intensity [57]. Occultations of stellar light

reveal characteristics such as atmospheric scale height and thickness for planets in our solar system [50].

Following the development of interplanetary satellites, the use of radio signals to conduct occultation experiments allowed for better knowledge and control of the characteristics of the initial radio waves. A signal generated onboard a spacecraft permits a deeper analysis of the atmosphere of interest as the source signal characteristics are typically better known and optimized for particular sensing experiments. Timing of a specific collection event is more conveniently obtained with satellite generated signals, as opposed to natural light phenomenon.

The first RO mission utilizing signals from a satellite took place in 1964, when telecommunications signals from Mariner IV were occulted by the Martian atmosphere before reception at Earth. Using ray theory methodology borrowed from seismology, the occultation collection allowed for successful construction of vertical refractivity profiles of the Martian atmosphere, as well as the associated density and pressure information [57]. The Voyager missions collected RO measurements to probe the ionospheres, atmospheres, and rings of the gas giants. The one-way signal transmission system developed for Voyager used dual-frequency signals and temperature controlled quartz oscillators to provide better quality occultation measurements. The RO data collected by the Voyager missions resulted in better characterization of Saturn's rings, an in-depth study of the planetary atmosphere, discovery of Saturn's magnetic field, and significant improvement to the estimate of Titan's radius [81].

1.1.2   Earth Occultation Missions

The success of interplanetary occultation missions led to the application of RO to probe the Earth's atmosphere. To study the Earth's atmosphere, early RO experiments were performed by a satellite-to-satellite tracking link. With precise knowledge of the location of the receiver and transmitter, the RO technique allows for examination of an intervening medium through measurement of the time delay of arrival of the refracted signal. Collections by the space station, Mir, from a geostationary satellite and between GEOS-3 and ATS-6 were among the first attempts [57].

The GPS constellation has been utilized for an occultation signal source for twenty years. A near-ideal transmitting system, GPS consists of 32 satellites that continuously broadcast dual-frequency signals towards the Earth. RO satellite systems incur no cost to use these signals as they are a service provided by the U.S. government. A GPS RO event occurs when a receiver detects a signal from a GPS satellites as it ascends or descends behind the Earth's limb, as shown in Figure 1.2. The radio signal experiences an increased optical path, delayed in terms of expected arrival as compared to signal propagation through a vacuum. The relative motion between the LEO and GPS satellite causes the signal path to slice through different vertical layers of the atmosphere during the occultation event.
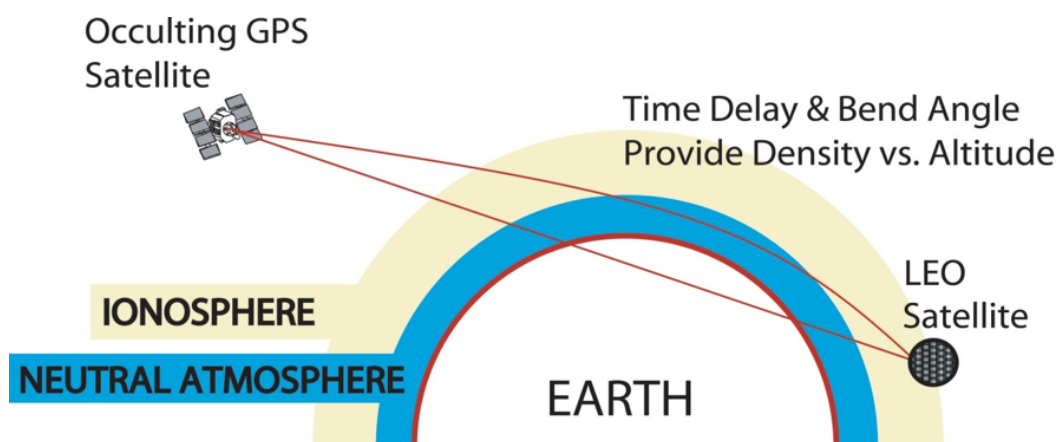
Figure 1.2: Geometry of GPS radio occultation event. The signal transmitted by the GPS satellite is delayed as it travels through the Earth's ionosphere and neutral atmosphere. The time delay and bending angle provide density as a function of altitude. Illustration courtesy of Broad Reach Engineering [11].

The fundamental quantity measured in a GPS RO event is the time delay to the signal, which varies as a function of the index of refraction of the medium through which the signal is traversing. Although RO is conceptually simple, isolation of the atmospheric influence on the signal is difficult. The motion of the satellites, receiver and transmitter clock stability, and relativistic effects must be accounted for to completely characterize the signal. It is even more difficult to define proper boundary conditions, use appropriate smoothing intervals and interpolation schemes

(to avoid artificial structures in the atmosphere), and to detect and correct phase measurement errors introduced by sharp refractivity gradients [34]. By combining the simple time delay effects and correctly accounting for these additional complicating elements, using techniques described in more detail in Chapter 2, a very accurate atmospheric measurement can be derived.

Many applications make use of RO data, including meteorology, weather prediction, and global climate change studies. The incorporation of occultation data allows for the fine structure of the refractivity boundaries to be determined. It also provides a better understanding of the energy transportation and exchange processes across the tropopause. Occultation measurements are incorporated into the study of gravity waves and their effects on wind velocity, temperature, and density of the atmosphere [33]. Occultation observations near the Earth's surface provide constraints on water vapor levels, which is an important factor in determining the energy transfer and balance processes in the atmosphere and aerosol growth and cloud formation [48]. RO measurements could also be used to detect increased water vapor content and variability in the tropics, changes to the water vapor in the upper troposphere, and warming in the lower troposphere polar regions [57].

Stability, accuracy, fine vertical resolution, and global coverage of the occultation measurements are unique to RO and important for incorporation into weather and climate modeling. Numerical weather prediction (NWP) systems have assimilated vertical bending angle and refractivity profiles from RO observations and have reported positive impacts on weather forecasts [15, 38]. The assimilation of RO results from CHAMP and GPS/MET satellites improved the NWP analyses and forecasts in the upper troposphere and lower stratosphere when compared against radiosonde measurements [38]. Detecting subtle signatures of climate trend changes over long periods of time is a challenge. Spatial averaging is possible with the sheer number of daily occultation observations, allowing for the detection of secular trends in climate. Warming or cooling trends are revealed through averaged temperature profiles across the tropopause. Harnisch et al. (2013) indicates an increased impact on forecasting ability with increased RO observations [35].

Among the most successful RO missions is COSMIC, a constellation dedicated to making continuous occultation collections. At its peak performance, the joint Taiwan-U.S. venture pro-

duced as many as 2,500 RO profiles per day from six spacecraft in LEO. More than 600 researchers from 42 countries utilize the occultation products, which include electron counts in the ionosphere and atmospheric soundings of temperature, moisture, and pressure in the troposphere [84].

1.2   Motivation

1.2.1   Future of Radio Occultation

Radio occultation measurements utilizing GPS signals have proven to be very useful for both weather and climate prediction applications. The existing constellations of occultation satellites, however, are aging and producing fewer quality measurements. As of April 2014, COSMIC reports that 1,600 to 1,800 soundings are collected daily, with solar panel complications limiting two of the six COSMIC satellites to 50-66% of their power capacity [39]. Replacement fleets of occultation satellites are imperative to sustain the operational impact achieved by the COSMIC constellation. In addition, global coverage can be dramatically improved by increasing the number of GNSS RO receivers in orbit as well as the number of GNSS satellites they track.

The follow-on mission to COSMIC, FORMOSAT-7/COSMIC-2, plans to launch six satellites in late 2016 and another six are scheduled to launch 2018 to replace the current COSMIC constellation [84]. These satellites will be equipped with the TriG Radio Occultation System Space science payload, which is being developed by the National Aeronautics and Space Administration (NASA) Jet Propulsion Laboratory (JPL) and manufactured by Moog Broad Reach [55]. This receiver is the follow-on to JPL's BlackJack receiver (used on CHAMP, SAC-C, GRACE, TanDEM-X, TerraSAR-X, and COSMIC [91]) and is stated to provide support for the GPS L1 coarse acquisition (C/A), L2 semi-codeless, L2C, and L5 signals, as well as signals from the other GNSS constellations. The TriG will also be capable of real-time centimeter level positioning and millimeter per second velocity estimations for orbit determination [63]. The custom phased antenna array design onboard the COSMIC-2/FORMOSAT-7 will provide an additional 10 dB of gain in comparison to the antennas on the previous COSMIC mission, which is a significant improvement in quality of occultation

signals received [80].

Improvements and modifications are necessary for a new generation of GNSS occultation receivers, such as the TriG. Of highest priority is the increase to the quantity of observations made by the receiver. Although heritage RO missions only utilize the GPS signals on the L1 and L2 frequencies for observations, the occultation data retrieval technique is not limited to these signals. The GNSS consists of constellations of navigation satellites from the United States (GPS), Russia (GLONASS), European Union (Galileo), and China (BeiDou), as well as several satellite-based augmentation systems. Subsequently, the RO technique can be generalized to apply to all satellites and signals within the GNSS. Although the RO technique is not limited to navigation signals, the GNSS constellations provide an easily available and free signal source for occultation missions. Utilization of all GNSS signals will increase the number of occultations and thus provide better global coverage for weather and climate science.

The quality of the measurements made by the receiver should also be improved in comparison to previous RO missions. Better quality occultation observations can be made by collecting higher powered signals, such as the GPS L5 signals or Galileo signals, or with signals with better modulation structures, such as the GPS L2C signals. Erroneous influences to the signal carrier phase, such as satellite clock instability, can be better characterized and removed as well, leaving better estimates of excess frequency and amplitude and improved refractivity profiles of the atmosphere.

Further improvements to the quantity and quality of occultation measurements can be made through modifications to the occultation satellite orbital parameters and constellation configuration. Alterations to the inclination and altitude of the occultation satellite will increase the coverage in typically undersampled or remote areas. More inclined orbits will result in additional observations in the higher latitudes. Occultation antenna/receiver packages can also be considered for payloads on other spacecraft, as this will increase the number of atmospheric data sources, but only if these missions are able to provide the occultation data in real time.

1.2.2   Signal Sources

The GNSS consists of constellations of satellites that provide positioning and timing information for users on Earth or in orbit about the Earth. The United States initiated the first navigation system, GPS, and has maintained full operability since 1995 [26]. GPS consists of at least 24 satellites in approximately 12-hour orbits in six orbital planes. The Russian Federation also operates a full GNSS constellation called GLONASS. After a period of disrepair in the early 1990s, the constellation has fully recovered and boasts 24 satellites in three orbital planes at an orbital period of 11 hours and 16 minutes. Galileo is the constellation of GNSS satellites under development by the European Union as an alternative to the Russian and U.S. systems. By 2020, 30 spacecraft are planned in three orbital planes with an orbital period of 14 hours and 5 minutes. As of March 2015, the Galileo system contains four validation satellites, and two full operational capability satellites [22]. BeiDou (or Compass) is the Chinese navigation satellite system that will consist of 30 MEO spacecraft and five geostationary satellites. A 14-satellite regional navigational constellation was finished in 2012 and completion of BeiDou Phase III is planned for 2017 [25]. A detailed description of the respective GNSS signals and their structures is given in Gleason and Gebre-Egziabher (2009).

The GNSS also includes several satellite-based augmentation systems, including the U.S. Wide Area Augmentation System (WAAS), the European Geostationary Overlay Service (EGOS), the Quasi-Zenith Satellite System (QZSS) operated by Japan, and the Indian Regional Navigation Satellite System (IRNSS), among others not mentioned here. Although these systems provide navigation signals and messages to users similar to those produced by GPS, GLONASS, Galileo, and the BeiDou MEOs, the augmentation satellites reside in geostationary or geostationary-like orbits. This allows for continuous coverage over regional areas by these augmentation systems. The antenna coverage patterns of the geostationary satellites, however, are not wide enough to provide signals towards the Earth's limb, thus negating the applicability of the RO technique to these augmentation systems.
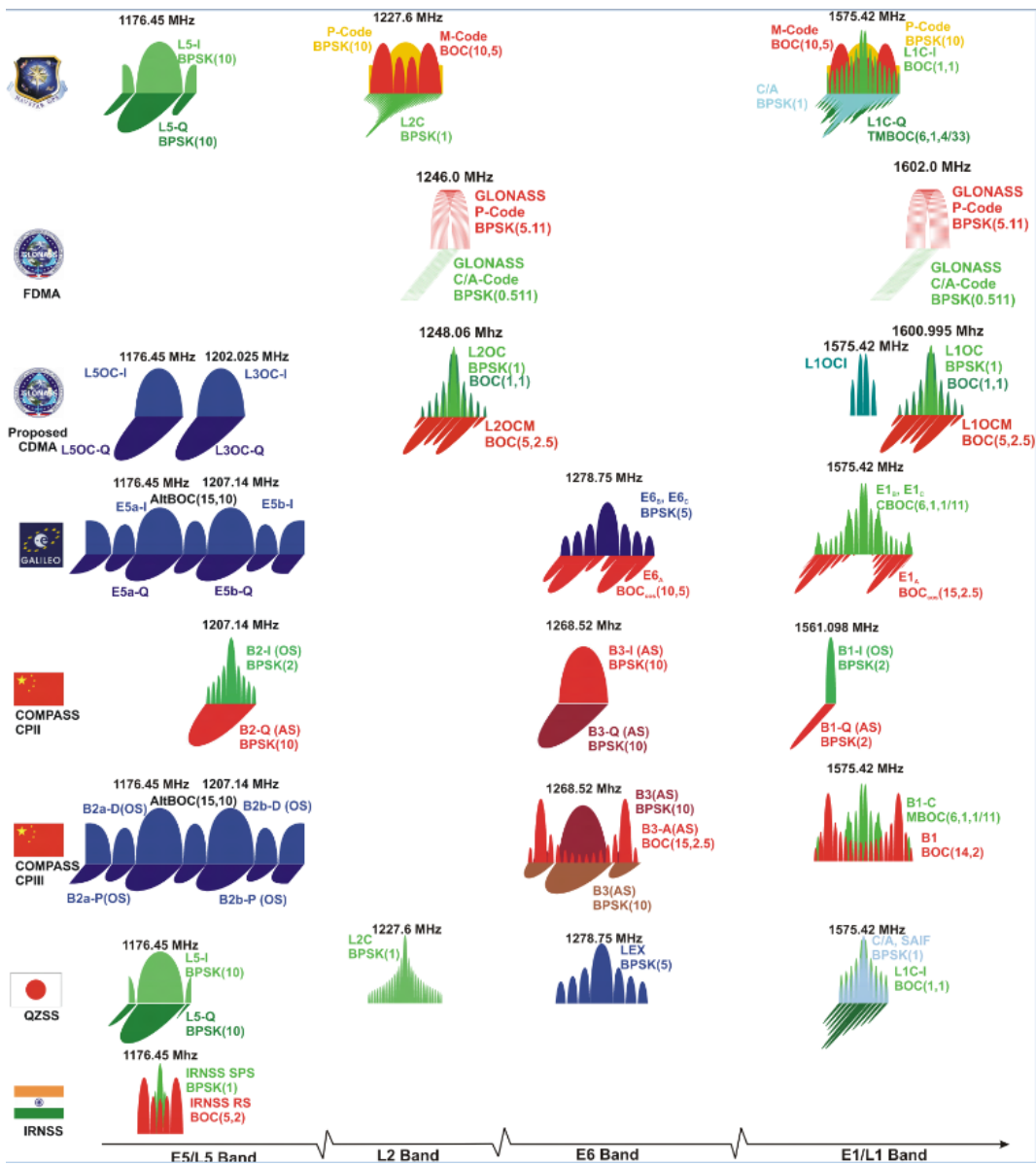
Figure 1.3: Frequency spectrum of signals from the GPS, GLONASS, Galileo, BeiDou (Compass), and augmentation systems (the Japanese QZSS and Indian IRNSS). Image reproduced from Navipedia [89].

The GNSS satellites provide a myriad of signal properties and characteristics, both beneficial and detrimental to the RO approach. Use of multiple constellations will increase the possible occultation opportunities while on orbit; however, the signals themselves are broadcast on varying frequencies. Figure 1.3 shows the frequency spectrums of the primary GNSS signals. The highest

overlap between constellations occurs at L1 = 1575.42 MHz, where civil signals from GPS, Galileo, Phase III BeiDou, and the future code division multiple access (CDMA) signals from GLONASS exist. Slightly offset from this frequency, both the GLONASS frequency division multiple access (FDMA) signals and the BeiDou B2 signals are found. With a sufficiently wide bandwidth for the receiver front end, signals from all GNSS constellations can be captured about L1.

As dual-frequency signals are needed for the first-order ionosphere estimation, a second frequency within the GNSS spectrum must be chosen. As shown in Figure 1.3, it is challenging to find a common value between the different constellations. As few options exist for overlapping spectra between constellations, a decision must be made for the best option for signal combinations for dual-frequency observations. Other than the differences in broadcast frequencies, the GNSS signals offer different modulations, structures, strength, and stability. The premise of this thesis is that, even given necessary differences in signal types, a global GNSS RO system can be designed in order to create an optimal solution for future occultation missions.

1.3   Thesis Synopsis

This thesis describes studies conducted to assist in the development of a next generation RO receiver and constellation. Several elements have been identified for consideration in the planning and design of future RO missions, which include:

- An understanding of the new GNSS signals with respect to their structure, power, and modulation for implementation and use in an RO-like scenario

- The possible orbital parameters and configurations that provide optimal coverage and collection opportunities for a future RO constellation

- The prediction and scheduling of occultation collections from a RO satellite with the new and upcoming GNSS satellites

- The quality of the GNSS signals, in terms of their stability performance, at timescales relevant to RO collections

Ultimately, the goal of this research is to improve the quantity and quality of measurements made by a future RO collection system. The research areas provided in the previous list provide an outline to the studies conducted for this thesis. The focus of this thesis is not to propose the entire architecture of a new occultation mission but rather recommend components of a modernized receiver and constellation that have desirable characteristics for RO collections.

The improvements to the RO mission architecture addressed in this thesis range from a micro-to-global scale. To better understand and resolve these research questions for a modernized RO receiver and constellation, the following studies were conducted:

- A ground-based occultation collection experiment was conducted to develop a software-based RO receiver and to demonstrate the abilities of this receiver to track and produce measurements as would a space-based RO receiver. Frequency observations recorded by the software receiver were translated into accumulated phase measurements and compared between the different signal modulations (Chapter 3).

- Simulations of coverage and occultation opportunities were conducted with the future GNSS constellations. These simulations varied the number of RO satellites and their respective inclinations, altitudes, and antenna behavior, while trying to optimize global coverage and the number of per satellite occultations (Chapter 4).

- Autonomous prediction and scheduling algorithms were implemented to assist with the timing and resource management for an occultation satellite. With the assumption of a sufficiently accurate navigation solution for the occultation satellite in real time, an autonomous occultation prediction and scheduling routine was developed that allows collection of signals from all GNSS constellations solely from their broadcast ephemeris messages (Chapter 5).

- A comprehensive study was undertaken to provide an in-depth characterization of the GNSS signal quality in terms of the transmitting clock stability, as the GNSS oscillator stability affects all future occultation missions. The variations from precision oscillators

of all GNSS satellites were isolated and compared at time scales relevant to RO events. Oscillator instabilities were translated to errors in the occultation products and possible correction schemes are suggested (Chapters 6 and 7).

Chapter 2 provides a brief overview of the general RO technique, and Chapter 8 summarizes the thesis and provides the key contributions found in these studies.

Chapter 2

THE GNSS RADIO OCCULTATION PROCESS

This chapter serves as the fundamental background information for the RO collection process. To obtain accurate atmosphere retrievals, the signal must first be calibrated to isolate the atmospheric contribution from the satellite kinematics and various clock influences. The signal time delay is the main RO observation and is translated to physical characteristics of the atmosphere. As mentioned in Chapter 1, multiple Earth sensing missions already employ RO techniques in some form; therefore the algorithms to process measurements from an RO event are well known. During an occultation collection event, values of the signal carrier phase and amplitude are recorded from the space-based receiver in LEO. The excess Doppler frequency and signal-to-noise ratio (SNR) are then measured and used to calculate the ray impact parameter, a, and bending angle profile $\alpha(a)$. Finally, the bending angle profile is inverted to give the refractivity profile. Temperature (T), pressure (P), and water vapor content (P_w) are directly related to the refractivity, and can be inferred from the vertical refractivity profiles.

General descriptions for these processes follow in the next sections. A more detailed account of the bending angle can be found in Gleason and Gebre-Egziabher (2009), Melbourne (2005), and Hajj et al. (2002). Refer to Kursinski et al. (2000) for omitted technical details concerning the transformation between occultation measurements and atmospheric properties. The error in the estimated values for temperature, pressure, and water vapor, in addition to other quantities, is characterized in Kursinski et al. (1997).

2.1 Generic Occultation Event

During an occultation event, the signal propagation between two satellites is delayed because of atmospheric interference. The total measured delay of the signal between the two satellites, in units of length, is modeled as [26]:

$$L = -\frac{c}{f}\phi = r + \gamma + C_t + C_r + \nu \tag{2.1}$$

where c is the speed of light in vacuum, f is the carrier frequency for the source signal in Hz, ϕ is the recorded phase in cycles, r is the geometrical range between the transmitter and receiver, γ contains the excess delay due to the Earth's atmosphere, C_t and C_r are the respective clock errors for the transmitter and receiver, and ν is the additional measurement noise.

The goal of the RO process is to isolate and extract γ as accurately as possible. Then specific principles of atmospheric science theory are applied to relate the atmospheric delay to physical characteristics and structures in the atmosphere. Generally, the phase of the occulted signal will change for the following three reasons: the relative motion of the two satellites, the drift of the clocks driving the transmitting and receiving hardware, and/or the refractive bending and propagation velocity changes in the ionosphere and neutral atmosphere [70]. The phase accumulation from relative satellite motion can be accounted for through precision orbit determination of each of the respective satellites. The clock errors in the transmitter and receiver are resolved by differencing, solving for the clock error in the filter, or using high-rate clock products. After resolution of the geometric range and clock contributions, the excess phase from atmospheric refraction and additional measurement noise remain.

2.2 Calculation of Excess Delay

From the perspective of the occultation receiver aboard the LEO satellite, the first step in an RO event is the collection of the signal. The raw electromagnetic energy transmitted by the source satellite is transformed to carrier phase and amplitude measurements, necessary for the occultation calculations. The GPS satellites have been the primary signal source for occultation missions in

the past twenty years; consequently, the development here will focus on the GPS signals and their characteristics. The descriptions can be generalized to other signal sources with sufficient signal power and Earth coverage.

GPS signals are spread spectrum signals, meaning the signal is deliberately spread in the frequency domain to occupy a bandwidth greater than the rate of the data being transmitted. The spreading method, or Direct Sequence Spread Spectrum (DS-SS), is accomplished by modulation of the carrier wave with a high frequency pseudorandom noise (PRN) spreading signal [26]. The signal is despread in the receiver by multiplication with a synchronized replica of the spread code signal, resulting in the recovery of the desired data signal. The recovered signal will also contain errors from thermal noise, atmospheric, and multipath contributions during signal propagation.

The PRN code also serves as a unique identifier for each satellite. The PRN codes have the quality that they correlate well with themselves but not with other PRN codes. Therefore to determine the identity of the source GPS satellite, the receiver needs only to correlate the incoming signal with all known PRN codes to find the pair that best match. Once the identity of the satellite is known, the geometric range between the receiver and GPS satellite is determined through decoding the signal and processing the satellite ephemeris.

The signals arriving at the receiver have an inherent delay due to the distance between the transmitter and receiver and an additional Doppler effect due to the relative motion of the spacecraft. During signal acquisition, the receiver must perform correlation operations with the known PRN codes in both frequency and chip delay search spaces, which is a computationally expensive operation. The signal acquisition process can be aided or even skipped with a-priori knowledge of the GPS constellation status. At this point in the receiver processing, initial estimates of the carrier frequency and chip delay are approximate and refined further in tracking loops.

GPS receivers rely on delay lock loops to maintain lock on the code phase of the signal. These loops continuously adjust the rate of the replica PRN code to maintain correlation with the code on the incoming signal [58]. When aligned, the PRN code is wiped from the signal, leaving behind the carrier of the signal modulated by the navigation data bits. GPS receivers generally use phase

lock loops (PLL) or frequency lock loops (FLL) to better estimate the carrier frequency and phase of the incoming signal. In positioning applications, the carrier phase is wiped from the signal, and the remaining navigation message is decoded. This message provides the ephemeris of the source satellite and a lower quality almanac of the entire constellation. The precise ranges to each of the incoming signals are calculated from the ephemeris information, and the receiver position and timing are solved for using a least squares solution.

The PLL is routinely used for carrier phase tracking in GPS receivers, as it is well-suited for tracking narrow-band signals with sufficient SNR. The PLL is limited, however, for tracking signals of an RO event, as the carrier phase is subject to large phase and amplitude variations due to atmospheric structures. The traditional tracking loops in a GPS receiver extract the phase or frequency of a signal in real time and make a projection of the expected phase/frequency observation ahead. The measurement residual is used to update the tracking model for the next sampling interval. In the case of GPS RO measurements, the atmospheric influence to the signal causes additional errors to the phase observations. As the errors in the phase/frequency extraction process increase, the projection of the next measurement becomes less accurate until the receiver eventually loses lock on the signal. The use of PLL tracking in RO collections has led to significant refractivity inversion errors [78].

To avoid these errors, model-aided open-loop (OL) tracking is used in many of the current RO receivers. Similar to the traditional acquisition process, the signal is subject to direct raw sampling and correlation with the replica signals for the duration of the occultation. To reduce the costly frequency search space during correlation, estimations of the received signal frequency are made with precise Doppler modeling. The OL tracking results in signal strength (or amplitude) estimates and an accumulated phase difference, or excess phase, from the modeled Doppler.

2.3   Bending Angle Calculation

The excess phase delay and SNR/amplitude measurements accumulated by the occultation receiver in the tracking loops are used to calculate the bending angle profile, $\alpha(a)$, where a is the

ray impact parameter, as depicted in Figure 2.1 [26, 34]. The following relationship relates the excess Doppler frequency, Δf, or equivalently the time derivative of the phase measurements, to a geometric representation of the signal propagation.

$$\lambda \Delta f = \mathbf{v_t} \cdot \hat{\mathbf{k}}_\mathbf{t} - \mathbf{v_r} \cdot \hat{\mathbf{k}}_\mathbf{r} - (\mathbf{v_t} - \mathbf{v_r}) \cdot \hat{\mathbf{k}} \qquad (2.2)$$

$\mathbf{v_t}$ and $\mathbf{v_r}$ are the transmitter and receiver velocities, $\hat{\mathbf{k}}_\mathbf{t}$ and $\hat{\mathbf{k}}_\mathbf{r}$ are the unit vectors corresponding to the transmitter and receiver ray directions, λ is the wavelength, and $\hat{\mathbf{k}}$ is the unit vector from the transmitter to receiver.
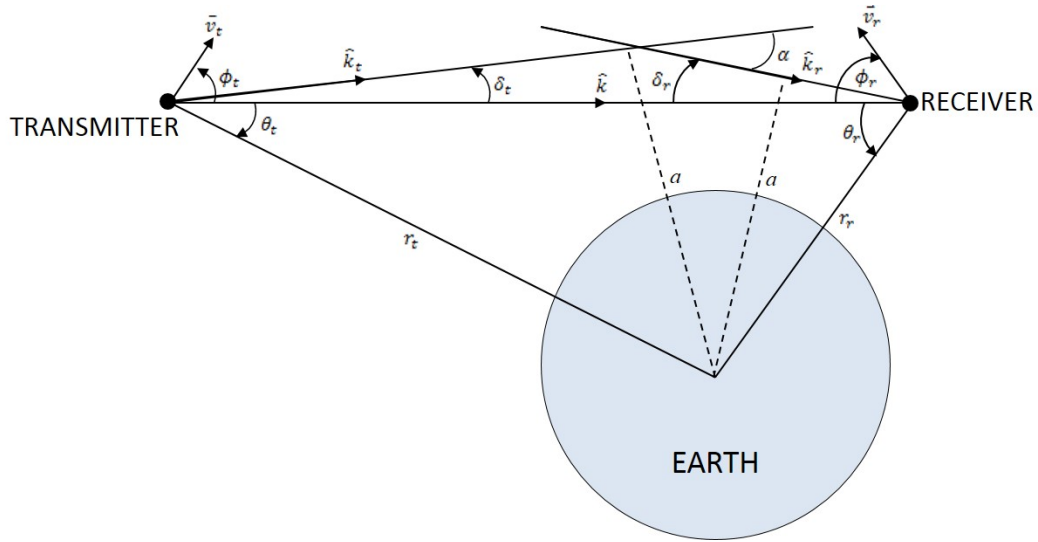
Figure 2.1: Geometry for deriving the bending angle and unique impact parameter from the excess Doppler frequency. The subscript t represents "transmitter", while the r subscripted terms are associated with the "receiver". $\mathbf{v_t}$ and $\mathbf{v_r}$ are the velocities, $\hat{\mathbf{k}}_\mathbf{t}$ and $\hat{\mathbf{k}}_\mathbf{r}$ are the unit vectors corresponding to the ray directions, λ is the wavelength, a is the impact parameter, α is the bending angle, and $\hat{\mathbf{k}}$ is the unit vector from the transmitter to receiver. The assumption of a spherically symmetric atmosphere allows for the simplification to planar geometry. Adapted from Gleason and Gebre-Egziabher [26].

If the assumption of a spherically symmetric neutral atmosphere is made, then the ray path is confined to a plane, simplifying Equation 2.2 to the following.

$$\lambda \Delta f = v_t \cos(\phi_t - \delta_t) - v_r \cos(\phi_r - \delta_r) - (v_t \cos \phi_t - v_r \cos \phi_r) \qquad (2.3)$$

where v_r and v_t are now scalar values, and ϕ_t and ϕ_r are angles represented in Figure 2.1. The

formula of Bouguer (equivalent to Snell's law in a spherically symmetric medium) is used to determine the impact parameter, a, and is shown in Equation 2.4. The impact parameter is an invariant property of the ray as long as there are no horizontal gradients in the refractivity [26].

$$a = n(r_t)r_t \sin(\theta_t + \delta_t) = n(r_r)r_r \sin(\theta_r + \delta_r) \tag{2.4}$$

The indices of refraction for the transmitter and receiver are given by $n(r_t)$ and $n(r_r)$. At the approximate height of the transmitting GPS satellite and the receiver in LEO, the indices of refraction are assumed to be unity (in most cases) [34].

Solving Equations 2.3 and 2.4 simultaneously leads to solutions for the unknown angles, δ_t and δ_r. The ray bending angle, α, is then equal to the sum of these angles.

$$\alpha = \delta_t + \delta_r \tag{2.5}$$

The dispersive nature of the ionosphere causes the bending angle profile to be frequency dependent. The phase difference due to the ionosphere must be removed; therefore, dual-frequency measurements are necessary. The linear combination of signals from two different frequencies allows for the removal of ionospheric errors as a first-order approximation [87].

This bending angle calculation method works well at high altitudes, but below 6 km, multiple ray paths often converge at the receiver due to the presence of atmospheric structures [26]. SNR data, in conjunction with the occultation phase data, are commonly used to mitigate this issue of multiple ray paths [29].

2.4   Transformation to Atmospheric Quantities

The Abel transform, shown in Equation 2.6, provides a way to calculate the refractivity profile in terms of the impact parameter, a [51, 37].

$$\log n(a) = \frac{1}{\pi} \int_a^\infty \frac{\alpha(\rho)}{\sqrt{\rho^2 - a^2}} d\rho \tag{2.6}$$

With the assumption of a spherically symmetric atmosphere, the Abel transform is derivable from the basic integral equation for the bending angle [57].

$$\alpha(a) = -2a \int_a^\infty \frac{d \log n}{d\rho} \frac{d\rho}{\sqrt{\rho^2 - a^2}} \tag{2.7}$$

Using the relationships in Equations 2.6 and 2.7, the refractive index can be recovered as a function of altitude. The refractive index, $N = (n-1) \times 10^6$, is directly related to electron density in the ionosphere and is a function of pressure, temperature, and water vapor in the neutral atmosphere, as shown in the following equation [26]:

$$N = (n-1) \times 10^6 = a_1 \frac{P}{T} + a_2 \frac{P_w}{T^2} - 40.3 \times 10^6 \frac{n_e}{f^2} + O\left(\frac{1}{f^3}\right) + a_w W_w + a_i W_i \tag{2.8}$$

where $a_1 = 77.6$ K/mbar, $a_2 = 3.73 \times 10^5$ m K^2/mbar, P is the total pressure, T is the temperature, P_w is the water vapor partial pressure, n_e is the electron density in m^3, f is the operating frequency in Hz, W_w and W_i are the liquid water and ice content in g/m^3, and a_w and a_i are 1.4 and 0.6 m^3/g [34].

The first two terms of Equation 2.8 result in the neutral atmosphere refractive index and are referred to as the dry and wet terms. Given N, solving for P, T, and P_w in Equation 2.8 requires the ideal gas law and hydrostatic equilibrium as constraints.

$$\frac{dP}{dh} = -g\rho \tag{2.9}$$

$$\rho = \rho_d + \rho_w = \frac{m_d P}{TR} + \frac{(m_w - m_d)P_w}{TR} \tag{2.10}$$

h is the height, g is the gravitational acceleration of the Earth, ρ, ρ_d and ρ_w are the total, dry air, and water vapor densities, m_d and m_w are the mean molecular mass of dry air (28.98 g/mole) and water vapor (18.0 g/mole), and R is the universal gas constant ($8.3144621 \frac{\text{J}}{\text{mol K}}$).

Further manipulation of Equations 2.9 and 2.10 described in Hajj et al. (2002) reveals the following relationship [34].

$$\frac{dP}{dH} = -\frac{g m_d}{a_1 R} N + \frac{a_2 g m_d}{a_1 R} \frac{P_w}{T^2} + \frac{g(m_d - m_w)}{R} \frac{P_w}{T} \tag{2.11}$$

Three unknowns (P, P_w, and T) and two independent equations now exist. Water vapor pressure is most significant in the lower troposphere; therefore, the temperature, T, and pressure, P, can be solved for in the upper troposphere and stratosphere given a boundary condition [51]. The following equations solve for the temperature and pressure in this "dry retrieval".

$$P(h) = P(h_{max}) + \frac{m_d}{a_1 R} \int_h^{h_{max}} dh' g(h') N(h') \qquad (2.12)$$

$$T(h) = a_1 \frac{P(h)}{N(h)} \qquad (2.13)$$

At lower altitudes, P_w is more significant; therefore, the temperature and water vapor cannot be solved for independently. An approach to this problem is to assume the temperature profile is known, and solve for P and P_w iteratively. Kursinski and Gebhardt (2014) gives a detailed description to derive water vapor given knowledge of temperature and refractivity as a function of height [49].

Chapter 3

GROUND-BASED OCCULTATION

This chapter provides a detailed study of signals collected from a ground-based RO experiment. A ground-based occultation collection allows for development and implementation of algorithms specific for handling occultation-like data. In a receiver designed for RO, the amplitude and excess frequency observations are used to determine the occultation bending angle and impact parameter, and subsequently, vertical refractivity profiles. The general description for the derivation of RO data products from the GNSS signals is given in Chapter 2. Traditional GNSS signal tracking techniques fail for RO signal collection as the variations in signal amplitude and phase cause the tracking loops to lose lock. For ground-based collections, modifications to these algorithms are necessary to accommodate for the subtle changes in geometry [94].

Signals from two setting GPS satellites were taken from the summit of Pikes Peak, Colorado on 21-Oct-2011. Legacy and modernized GPS civilian signals were acquired and tracked to negative elevation angles using a software defined radio (SDR). As no truth metrics were obtained for the particular location and date for comparison, the focus of this collection experiment was to obtain the carrier phase and signal amplitude measurements similar to how an occultation receiver would do in space, except that the geometry is changing much more slowly with time.

3.1 Background

Remote sensing of the Earth's atmosphere via RO is employed by multiple missions, including GPS/MET, CHAMP, GRACE, SAC-C, and COSMIC [4]. These space borne experiments provide

numerous occultation soundings daily. Unfortunately, raw radio frequency (RF) data from these satellites is largely unavailable for use in algorithm development and testing for a new generation of RO receivers. Airborne and mountain-based horizontal looking experiments are considered a hybrid between the space and ground viewing geometries as it provides local atmospheric data for the region surrounding the receiver [94]. A terrestrial experiment provides the vertical profiling capability of a space-based receiver as the geometry is similar to the GNSS-LEO occultation event from space. Ground-based receivers also provide ample collection opportunities with location and timing known a-priori. The duration of the ground-based and airborne RO experiments is much longer, however, because of the slower relative motion between the transmitter and receiver.

Successful mountaintop occultation campaigns were conducted on Mt. Fuji, Japan in 2001 and Mt. Wuling, China in 2005. Refractivity profiles obtained from applying Abel inversions to the bending angle between the GPS satellite and ground experiment were consistent with radiosonde observations for both experiments [5, 41]. To aid in signal tracking under chaotic conditions, the open-loop (OL) tracking techniques described in Section 2.2 are adopted. In the winter of 2004, a ground-based experiment was performed in Gothenburg, Sweden that utilized OL tracking [67]. Occultation results were inconclusive due to the inability to distinguish between atmospheric turbulence and receiver clock instability. A more successful trial in OL tracking was performed on an airborne occultation experiment in the southeastern United States in 2008, where OL results showed improvement over closed-loop tracking methods [53]. OL tracking was also shown to improve the analysis of measurements from the lower troposphere by SAC-C [4].

Ground-based radio occultation experiments have varied levels of success, largely dependent on the experimental hardware setup and location. Signal fluctuations due to atmospheric structures are more prominent in humid locales, thus experiments in more temperate climates are expected to show minimal spectral broadening [67]. For the experiment described here, significant turbulence to the signal propagation path was not expected because of the dry climate of the experiment location (Pikes Peak, Colorado). The primary objective of this experiment was to establish algorithms for model-aided open-loop and closed-loop tracking of GPS L1, L2C, and L5 signals. These algorithms

will serve as a test platform for the core signal processing architecture for a future RO receiver.

3.2 Experiment

3.2.1 Data Collected

Many mountain peaks exist within a close proximity of the University of Colorado that provide a high-altitude setting for terrestrial occultation collection. Limitation based upon the time of year, day, and summit accessibility reduced this search space to Pikes Peak, near Colorado Springs, Colorado. The collection was conducted on 21-Oct-2011 in an eastward direction from the summit to capitalize on an altitude increase of 2.4 km from the summit to the plains in the horizon.

As a preliminary study to the occultation receiver architecture, the focus of this ground-based experiment was to develop and test tracking algorithms. Therefore, the study was limited to GPS signals, where PRNs 1 and 17 were chosen as primary collection candidates due to their optimal, fast-setting occultation geometries, shown in Figure 3.1. The modernized GPS civilian signals, L2C and L5, are broadcast from these satellites ,which provide the necessary test cases for the development of tracking algorithms for the each of the signals. The modernized GPS satellites, Block IIR-M and beyond, broadcast two civil signals at L-band (f_{L1} = 1575.42 MHz, f_{L2} = 1227.6 MHz), both of which have binary phase-shift keying (BPSK) modulation [7]. The Block IIF satellites broadcast an additional wideband civil signal at f_{L5} = 1175.45 MHz, with quadrature phase-shift keying (QPSK) modulation [6].

The L1/L5 signals were first collected from PRN 1, while the second collection capitalized on the L1/L2C frequencies broadcast by PRN 17. A high sampling rate was required to capture the wideband L5 signal for the first occultation, but was reduced for the second occultation. The collection logistics for both satellites are summarized in Table 3.1.
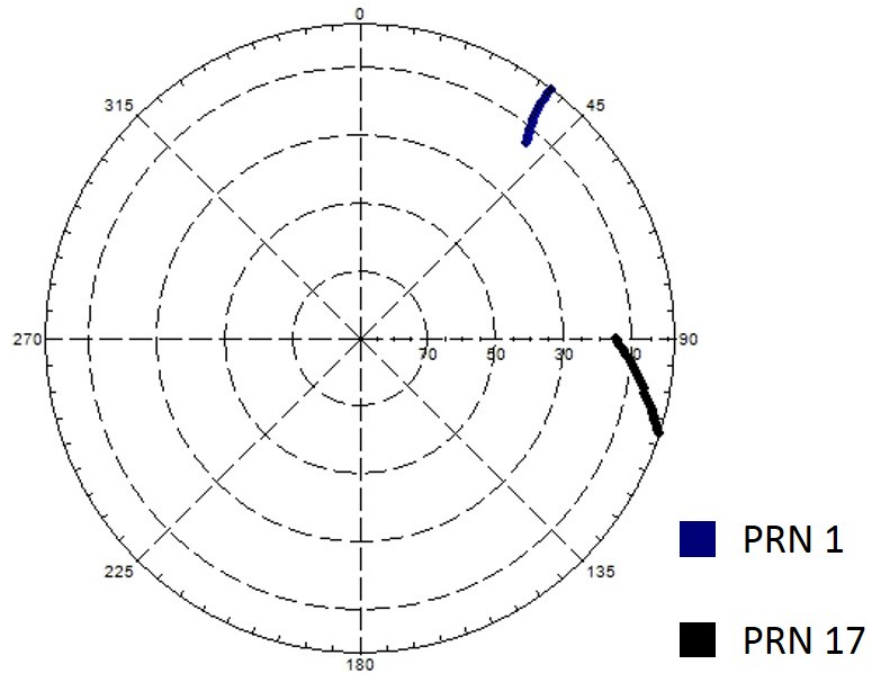
Figure 3.1: Azimuth/elevation plot for two ground-based occultation collection opportunities from the summit of Pikes Peak, Colorado on 21-Oct-2011. Both PRN 1 and PRN 17 provided fast-setting occultations east of the mountain.

Table 3.1: Summary of data characteristics from the two occultation events. Note the increased sampling frequency required to encompass the entire main lobe of the GPS L5 signal. The satellite vehicle numbers (SVN) are given for reference, and times are with respect to Coordinated Universal Time (UTC).

PRN/SVN	Freq	Start	Dur (min)	Az (°)	Freq (MHz)	IF (kHz)
1/63	L1/L5	17:30	42	38	4/20	420/450
17/53	L1/L2C	20:15	60	100	2/2	100/100

3.2.2 Hardware

A directional helix antenna, shown in Figure 3.2, was used to amplify the gain for collection of the occulting signal. As the helix antenna may not receive sufficient signal power from overhead satellites for a navigation solution, a multiband (L1/L2/L5) geodetic antenna was also used. Following the software radio paradigm, a recording system was used to capture a digital representation

of the signals output from the antennas. This allowed for post-processing of the data and utilization of a convenient computing environment for algorithm development. A commercial receiver, the Trimble NetR9, was connected to the multiband hemispherical antenna to confirm collection times. The system was synchronized with a common external rubidium frequency standard. A block diagram of the hardware setup for the L1/L5 collection is shown in Figure 3.3. The L5 filters were replaced by L2 filters for the L1/L2C collection.

Figure 3.2: L-band helix antenna used to collect the setting occultations from the summit of Pikes Peak. The external LNA is placed directly after the antenna in the RF chain.

Two configurations were used for the data collection: one for the Trimble antenna, the other for the high-gain helix antenna. The Trimble antenna has a built-in low-noise amplifier (LNA). In contrast, the helix required an external LNA, which was placed immediately after the
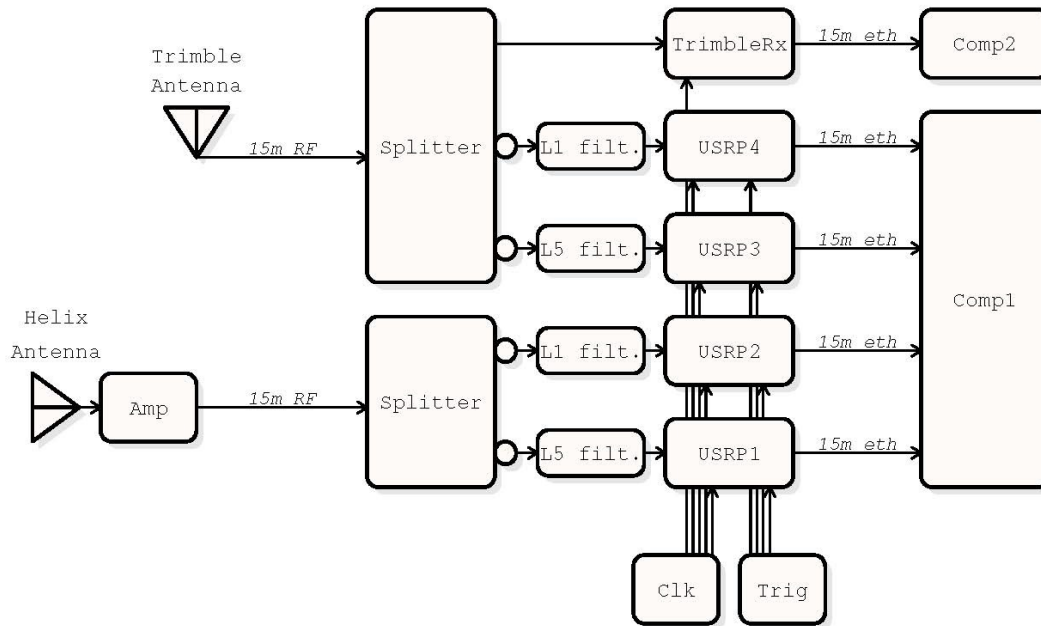
Figure 3.3: Block diagram describing the hardware setup for the Pikes Peak data collections. A hemispherical multiband antenna was used to collect overhead satellites for positioning and timing, while a directional helix antenna was pointed toward the horizon to collect signals from occulting GPS satellites.

antenna in the signal chain. To minimize radio frequency interference (RFI), fifteen meters of low loss RF cable was used to spatially separate the antenna from the recording equipment. Further shielding from self-generated RFI was provided with fifteen meters of Ethernet cables to allow for spatial separation from the recording equipment and the computers. Two RF splitters divided the wideband signals before they were fed into four Universal Software Radio Peripherals (USRPs), with direct current (DC) blocks (marked as circles in Figure 3.3) placed between the splitters and filters. The USRPs served to digitally sample the analog GPS signals. Appropriate cavity filters were used to isolate the frequency band of interest in the wideband signal. The Trimble NetR9 provided standard navigation messages, and the USRPs provided high-rate (between 8 and 80 MB/s) digital data output. The raw samples from the occultation events were filtered and down-converted to a nominal intermediate frequency (IF) by the USRP front end and saved to disk for future processing by the software receiver in the lab.

3.3 Occultation Signal Processing

3.3.1 Signal Acquisition

Acquisition of the signal was accomplished through correlation between a specific reference signal and the received signal from space. The acquisition process for each signal differed, as the modulation scheme and bit rates are unique to each signal, as described below.

For the GPS L1 civil signal, the C/A PRN code is repeated each ms with an additional data bit modulation at a 50 Hz rate [27]. A 10 ms coherent alternating block acquisition scheme was implemented to avoid the unknown navigation bit placement. Additional signal power was obtained with non-coherent summation of 10 consecutive coherent blocks.

The L2C signal broadcasts two PRN ranging codes: the civil-moderate (CM) and the civil-long (CL). The L2 CM signal is 20 ms in length and interleaved chip by chip with the L2 CL signal, which is 1.5 seconds in total length. The navigation message is added to the L2 CM signal at a rate of 50 bps [7]. One full L2 CM message (20 ms) was used for acquisition. To circumvent solving the code phase for the 1.5 second long CL signal, the CL blocks were zeroed out in the replica signal, resulting in a 40 ms long acquisition signal.

The GPS L5 signal also broadcasts two signals: the in-phase code (I5) and the quadraphase code (Q5). Unlike the L2C signal, these signals are concurrently broadcast and are each 1 ms in length. The I5 channel is modulated with a 100 sps navigation data stream and 10-bit known Neuman-Hoffman code, clocked at 1 kHz. The Q5 carrier is dataless, but is encoded with a 20-bit Neuman-Hoffman code, also clocked at 1 kHz [6]. Utilization of the dataless Q5 signal was sufficient for the purposes of this study, where 20 ms of coherent integration (one full Neuman-Hoffman code) was utilized for signal acquisition. Trials with longer integration times were conducted, but noticeable shifts in the acquired code phase were found due to the Doppler shift manifesting in the code.

3.3.2 Closed-loop Tracking

For the initial analysis, a closed-loop tracking scheme will a PLL was used to track the L1 signal for each occultation event. The PLL adjusted the frequency of the replica signal based upon the residual value of the previous measurement to track the incoming occultation signal. Values of the carrier phase were recorded at a $1\,\text{kHz}$ rate, and estimates of the signal power were made every $400\,\text{ms}$ using the variance summation method (VSM) for calculating the carrier-to-noise density ratio (C/N_0) [76]. The C/N_0 was used as a metric to determine whether the closed-loop tracking was successful at a given elevation angle, with a lower likelihood of continuous tracking at lower to negative elevations angles because of the atmospheric interference.

The estimated C/N_0 using a PLL for the first and second occultations of PRNs 1 and 17 are shown in Figure 3.4 and Figure 3.5. For reference, a simple line-of-sight estimate of the elevation angle of the geometric horizon with respect to the receiver is plotted in green. The occultation involving the Block IIF satellite, PRN 1, shows sufficient signal strength to keep lock for a short period after the geometric horizon, indicating some bending of the signal has occurred. However, the signal strength from the Block IIR-M satellite, PRN 17, was inadequate for closed-loop tracking of RO measurements. In this case, loss of lock occurred before the geometric horizon. Closed-loop tracking appears to be a viable option for some occultations, but not others. Suspected explanations include the original signal strength from the transmitting satellite, occultation geometry, or atmospheric turbulence interfering with the propagation of the signal.

Although closed-loop methods prove to be reliable for scenarios involving low signal dynamics and adequate signal power levels, they tend to fall short for tracking signals in the lower troposphere. Loss of lock in the PLL can occur due to decay of the signal amplitude, increased variation from diffraction and atmospheric multipath, and strong attenuation from refractivity layers [4]. Closed-loop approaches are a poor solution for rising occultations, as the signal power is too low to retain lock as the satellite emerges from behind the Earth's limb.
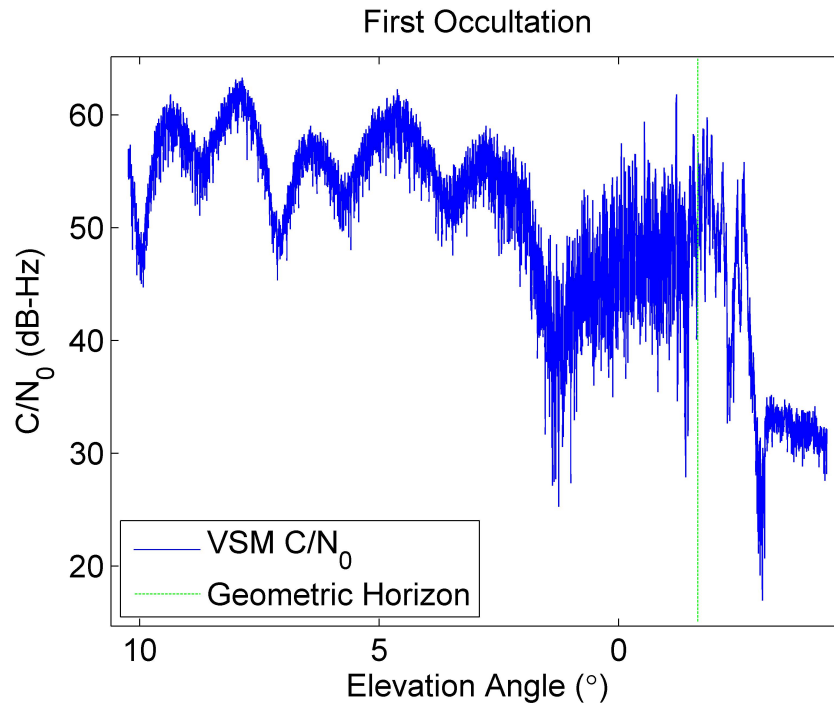
Figure 3.4: The C/N_0, as generated by the variance summation method, plotted as a function of elevation angle for setting occultation of PRN 1 [76]. Loss of lock using a feedback PLL technique appears to occur after the geometric horizon, shown as a vertical green line.
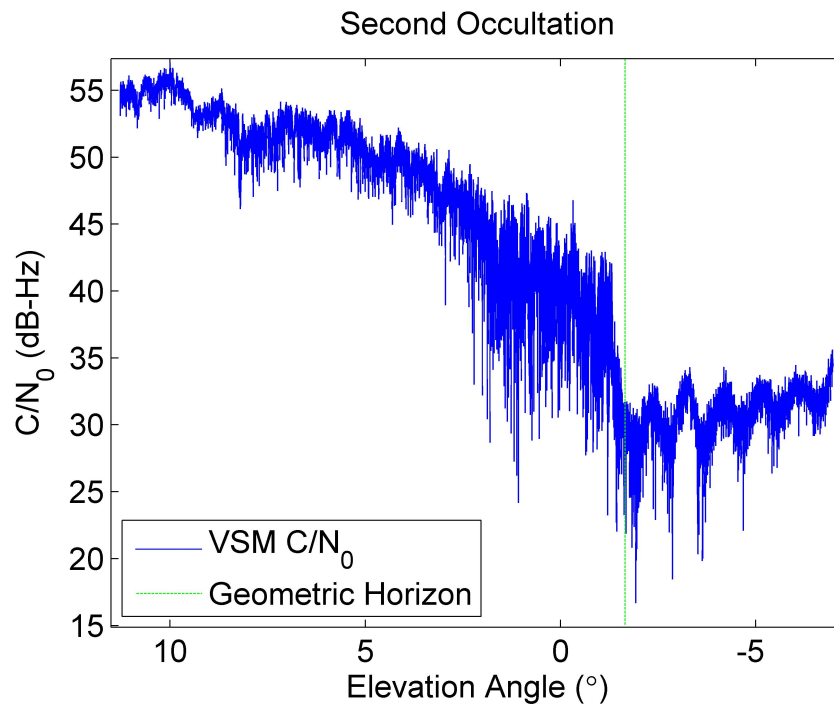
Figure 3.5: The C/N_0, as generated by the variance summation method, plotted as a function of elevation angle for setting occultation of PRN 17 [76]. Unlike PRN 1, lock of lock using a feedback PLL technique appears to occur before the geometric horizon, shown as a vertical green line.

3.3.3 Open-loop Tracking

OL tracking relies not on feedback loops to maintain lock on a signal, but on the accuracy of the estimated satellite orbits, receiver clock, and atmospheric Doppler shift and delay. The RO receiver for COSMIC utilizes two OL models that run in real time without feedback: 1) the phase (frequency) model used for frequency reduction and 2) the range model used for C/A code demodulation [78].

For the purposes of the ground-based occultation experiment, OL acquisition of the signals was aided by the use of precision Doppler models, traditional signal acquisition techniques, and additional sinc matching on the main lobe of the acquired signal. To develop an accurate Doppler prediction model, precise positions and velocities for both GPS satellite and occultation receiver are needed. The prediction model is necessary for even higher fidelity Doppler frequency estimates, as the search space within the receiver is greatly reduced. The line-of-sight Doppler frequency created by the relative motion between the satellite and receiver is given as

$$f_D = \frac{\hat{k}(\vec{v}_t - \vec{v}_r)}{\lambda} \tag{3.1}$$

where $\hat{k}$ is the unit vector from the RO receiver to GPS satellite, $\vec{v}_t$ and $\vec{v}_r$ are the velocities of the transmitter and receiver, respectively, and λ is the wavelength of the carrier wave.

The receiver location for the ground-based occultation experiment was known from decoding the navigation messages obtained from the upward looking Trimble antenna and performing a batch-filtered least squares estimate of the position for the duration of the occultation event. Precision orbits from the IGS Standard Product 3 (SP3) files were used to determine the GPS satellite positions at fifteen-minute intervals. Trigonometric interpolation provided satellite positions at 1-second intervals between the published fifteen-minute epochs [72]. The finalized GPS orbit products from the IGS are reported to provide GPS satellite positions to within 2.5 mm root mean square (RMS) accuracy, which is within the OL tracking noise level of other RO experiments [53]. The satellite velocities were approximated with a simple time-differencing method. Satellite clock corrections and relativity affect the satellite position at the centimeter-level, which is still within

an acceptable realm of accuracy for ground-based OL tracking. The Doppler model estimations were used as an initial estimate for a window of possible Doppler values.

The estimated Doppler for the setting occultation of PRN 1 using line-of-sight geometry is shown in Figure 3.6. The Doppler prediction was similar for PRN 17 and is not shown here for brevity. The estimated Doppler frequencies reduced the search space of the correlation operation within the OL tracking algorithm. To further reduce the computational complexity, the frequency search space was limited to the main lobe of the GPS spread signal sinc spectrum (also a function of coherent integration time). Table 3.2 describes the reduced frequency search space for each of the GPS signals and the step size used to maintain sufficient information about the location of the correlation peak. In general, sampling of five points above and below the center of main lobe provided a satisfactory estimate of the peak.
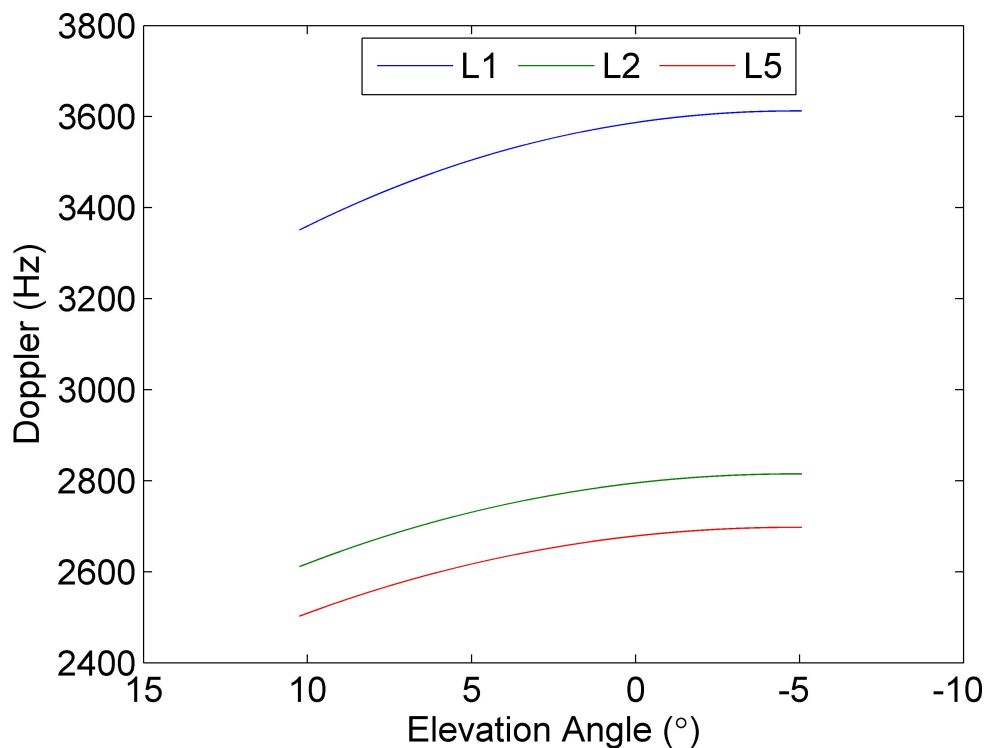
Figure 3.6: Doppler frequency estimations for the setting occultation of PRN 1 based upon line-of-sight geometry calculations. The Doppler values are scaled for GPS frequencies: f_{L1}, f_{L2}, and f_{L5}.

Table 3.2: Frequency search space and step size after application of Doppler prediction model and spectrum limitation to the main lobe of GPS signal.

Frequency	Main Lobe	Step Size
L1	± 50 Hz	10 Hz
L2	± 50 Hz	10 Hz
L5	± 100 Hz	20 Hz

Least squares sinc matching was applied as an additional measure to further refine the frequency estimate at each epoch. Replica codes were initialized to match the acquired code phase and were modulated by carrier waves at frequencies surrounding the estimated peak frequency. These test signals were correlated to the measured signal and best-fitted to a sinc function. A resulting shift in frequency was found that minimized the residuals between the theoretical sinc spectrum and the measured data. The least-squares sinc matching described here was optimized heuristically. Sampling the main lobe of the sinc spectrum at $1/10^{th}$ of the main lobe provided sufficient fidelity to best determine the signal frequency.

3.4   Results

Carrier phase data from both occultation events were processed using the OL tracking techniques described in Section 3.3.3. Measurements of precise carrier frequency were extracted and accumulated to create carrier phase measurements necessary for RO data retrievals. The difference between the measured data and the frequency model was integrated to obtain the accumulated phase difference, as described by the following relationship.

$$\phi_k = \phi_{k-1} + \int_{t_{k-1}}^{t_k} f_D(\tau)d\tau \tag{3.2}$$

where ϕ_k is the accumulated phase at epoch k and f_D is defined in Equation 3.1. In a typical occultation scenario, the accumulated phase measurements are expected to increase over the course of a setting occultation, as the atmosphere causes a delay to the propagation of the signal. The signal will have increased carrier phase cycles to accommodate for this delay.

The next subsections will describe the differences in modeled and measured frequency for the two setting occultation events collected and attempt to determine an accumulated phase measurement.

3.4.1   Occultation of PRN 1

The change in the measured frequency for the duration of the setting occultation event is shown in Figure 3.7. A change in frequency of approximately 250 Hz is seen between elevation angles of $10°$ and $-2°$. The peak metric shown is a value that describes the relative signal strength at that point in the collection and is calculated as the ratio of the energy found at peak correlation to the energy of the second highest peak [45]. Two vertical lines are plotted for reference: the blue line represents the local horizon, and the red line indicates the geometric intersection to the Earth horizon, relative to the receiver at the summit of the mountain peak. From Figure 3.7, the OL tracking successfully maintains lock on the signal of PRN 1 to negative elevation angles.

The Doppler difference between the OL tracking results and line-of-sight Doppler model on f_{L1} is shown in Figure 3.8. The difference is slightly negatively biased, indicating either overestimation of the Doppler effect or a possible timing offset between the two data sets. A distinct trend in the data appears at negative elevation angles that shows an elongation of the signal path. The measured carrier frequency becomes larger and more negative than the Doppler model, which describes a lengthened signal path, or similarly, a delayed phase observation.

Similar figures were produced for the f_{L5} signal from PRN 1. Figure 3.9 shows successful OL tracking down to negative elevation angles. The peak metric value of the f_{L5} frequency is generally higher than the f_{L1} frequency from the same satellite which was expected because of the minimum received RF signal strength reported by the respective Interface Control Documents (ICDs) [27, 6]. Although not as clear as on the L1 frequency, a phase delay is shown in Figure 3.10 for negative elevations.

From Equation 3.2, the accumulated phase delay can be calculated from the difference between the measured frequency and the Doppler model for the L1 and L5 signals, and is shown in

Figure 3.7: Change in the f_{L1} frequency of PRN 1 plotted as a function of elevation angle. The strength of the signal is measured from the peak metric of the open-loop acquisition function. The vertical blue line represents local horizontal, while the geometric horizon is given by the red vertical line.

Figure 3.8: Difference between frequencies reported by open-loop tracking and the line-of-sight Doppler model for PRN 1 on f_{L1}, as a function of elevation angle. The vertical green line represents local horizontal and the geometric horizon is given by the red vertical line.

Figure 3.9: Change in the f_{L5} frequency of PRN 1 plotted as a function of elevation angle. The strength of the signal is measured from the peak metric of the open-loop acquisition function. The vertical blue line represents local horizontal, while the geometric horizon is given by the red vertical line.

Figure 3.10: Difference between frequencies reported by open-loop tracking and the line-of-sight Doppler model for PRN 1 on f_{L5}, as a function of elevation angle. The vertical green line represents local horizontal and the geometric horizon is given by the red vertical line.

Figure 3.11 as a function of elevation angle. Both frequencies show a phase delay of approximately 14 meters at loss of lock of the OL tracking system.

Figure 3.11: Comparison of the accumulated phase, as calculated from open-loop tracking with a line-of-sight Doppler model, on f_{L1} and f_{L5} for PRN 1. Both show an accumulated phase of approximately 14 meters over the course of the setting occultation.

3.4.2   Occultation of PRN 17

A similar analysis was performed for the setting occultation of the Block IIR-M satellite, PRN 17. The primary difference in the collection of PRN 1 is that L2C was used as the second frequency rather than L5. Figure 3.12 shows the change in measured frequency of the L1 signal as a function of elevation angle. Loss of lock in the OL tracking is shown for elevations angles less than 5°. It is unlikely that the tracking loop failed due to some artifact of the atmosphere as the peak metric value indicates no lock whatsoever. A reasonable hypothesis to the tracking error is that

some hardware issue, likely an unstable oscillator or bad connection with the USRP, attributed to the loss of the signal on f_{L1}.

OL tracking for the signal on f_{L2} showed slightly better performance, as seen in Figure 3.13. Although a relatively low peak metric is shown at $5°$ elevation, the OL tracking mechanism maintains locks on the L2C signal. This supports the hypothesis that hardware, rather than atmospheric influences, caused the tracking glitch for the PRN 17 L1 signal. Another signal with equivalently high peak metric values manifested at a frequency difference of 40 Hz from the original signal. The additional signal might be an indication of an atmospheric inversion or possible multipath. It could also be a results of hardware or clock issues.

The Doppler difference between the strongest signal shown in Figure 3.13 and line-of-sight Doppler model on f_{L2} is shown in Figure 3.14. Again, the difference is negatively biased, indicating either overestimation of the Doppler effect or a possible timing offset between the two data sets. The difference becomes larger in magnitude at negative elevation angles, although not as distinctively as for the PRN 1 data set.

The accumulated phase was calculated for portions of the occultation results that were in agreement with the Doppler model. Although no conclusions were drawn from the f_{L1} Doppler difference (as loss of lock occurred too early in the occultation event), integration of the f_{L2} results showed a phase accumulation of approximately 6.5 meters, which is shown in Figure 3.15.

3.5   Significance

These preliminary findings suggest that a mountain-based collection with OL tracking is a feasible technique, provided an active atmosphere and proper hardware setup. Further utilization of the CL and I5 codes on the L2C and L5 signals will increase the signal power. Using these codes, however, will also require the removal of the navigation data bits, as they are indistinguishable from atmospheric modulation on the GPS signal [78]. This is the first ground-based RO experiment utilizing the GPS L5 signals.

Additional effort is needed to produce atmospheric profiles from the receiver observables,
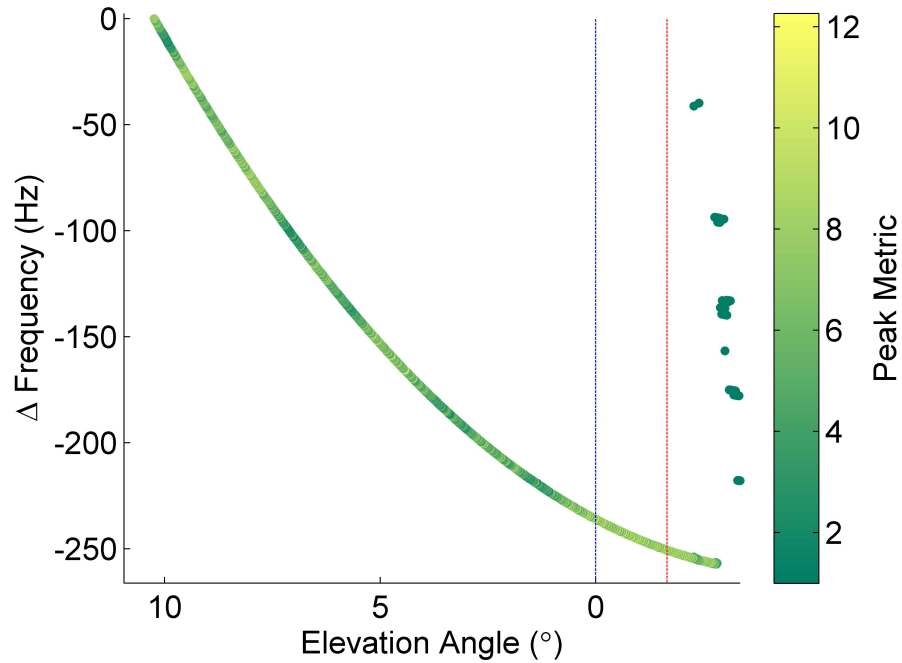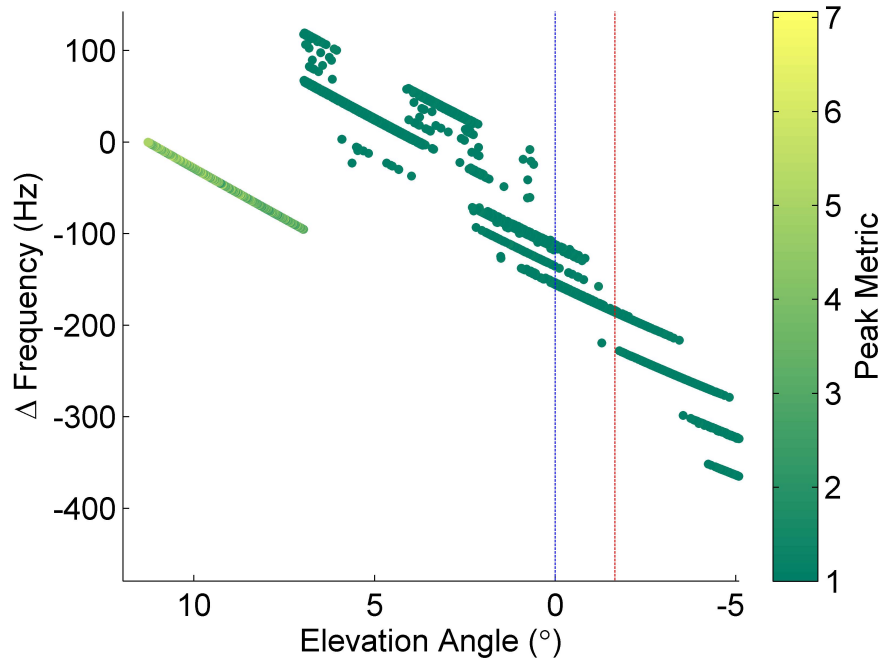
Figure 3.12: Change in the f_{L1} frequency of PRN 17 plotted as a function of elevation angle. The strength of the signal is measured from the peak metric of the open-loop acquisition function. The vertical blue line represents local horizontal, while the geometric horizon is given by the red vertical line.
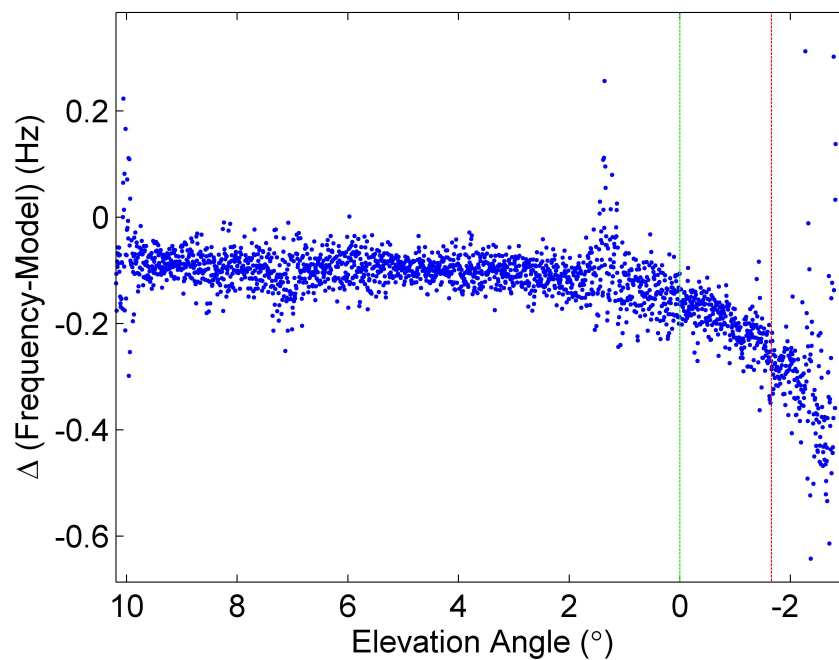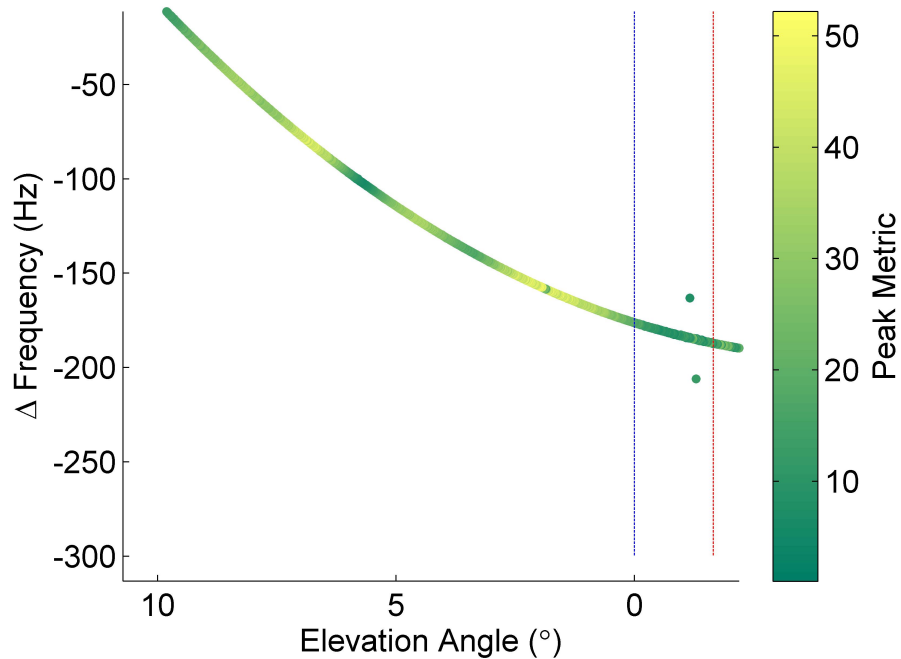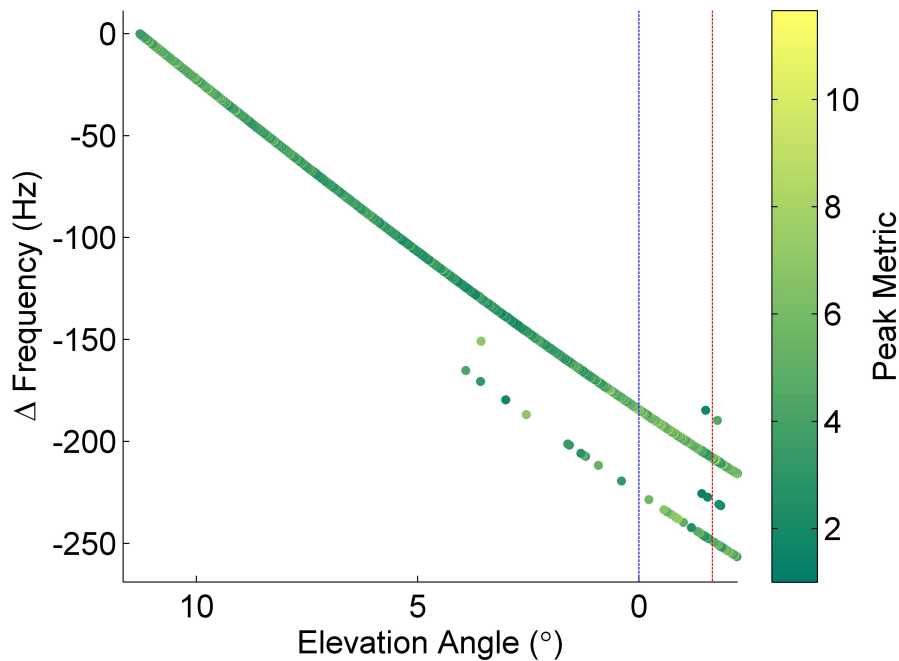

Figure 3.13: Change in the f_{L2} frequency of PRN 17 plotted as a function of elevation angle. The strength of the signal is measured from the peak metric of the open-loop acquisition function. The vertical blue line represents local horizontal, while the geometric horizon is given by the red vertical line.
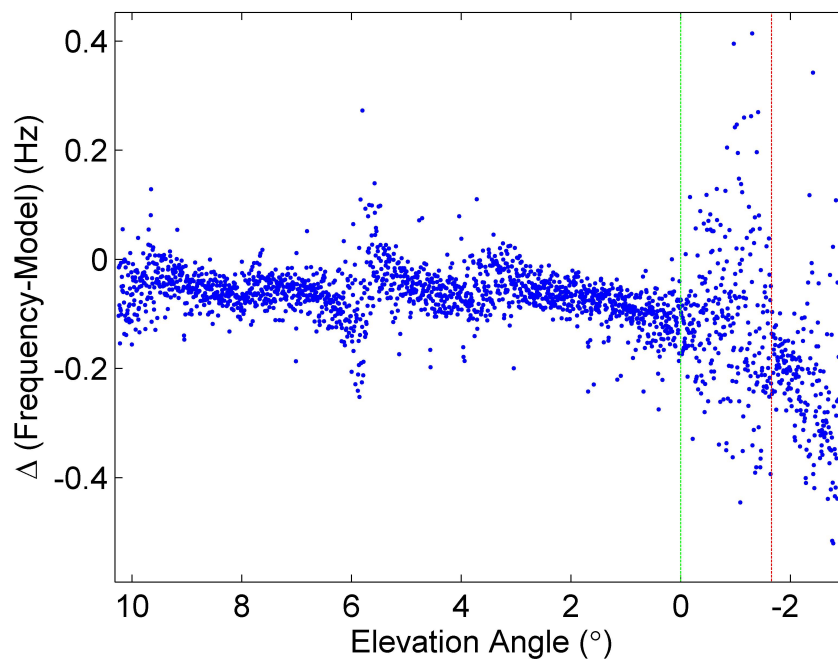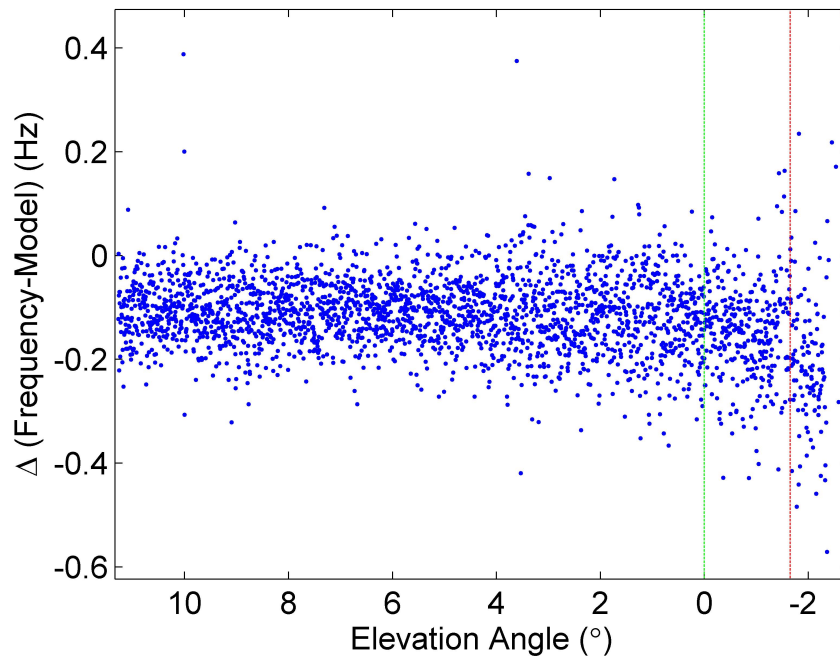
Figure 3.14: Difference between frequencies reported by open-loop tracking and the line-of-sight Doppler model for PRN 17 on f_{L2}, as a function of elevation angle. The vertical green line represents local horizontal and the geometric horizon is given by the red vertical line.
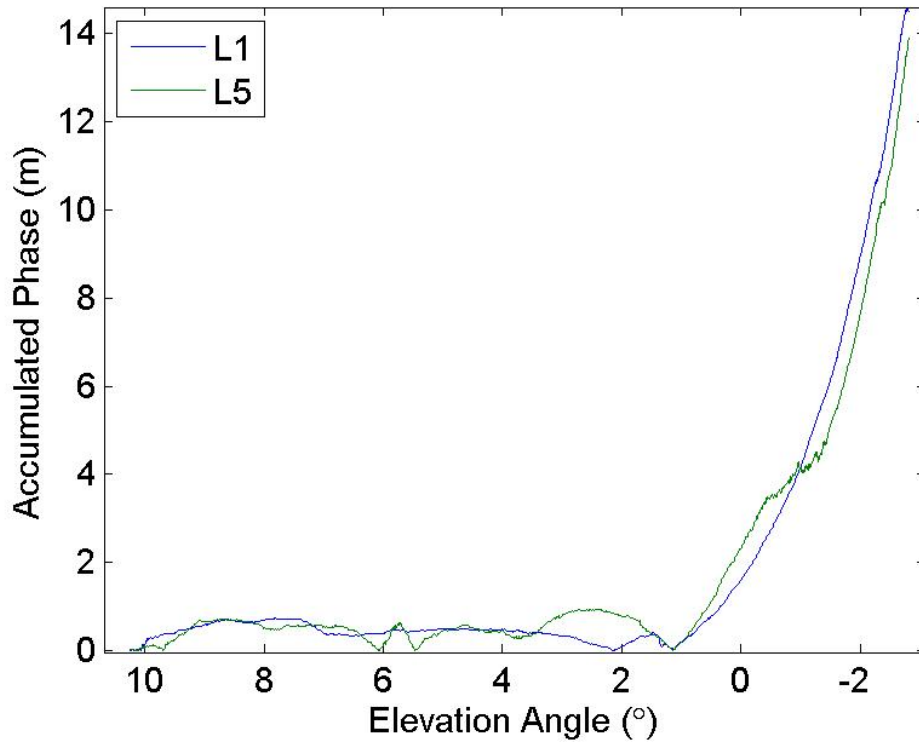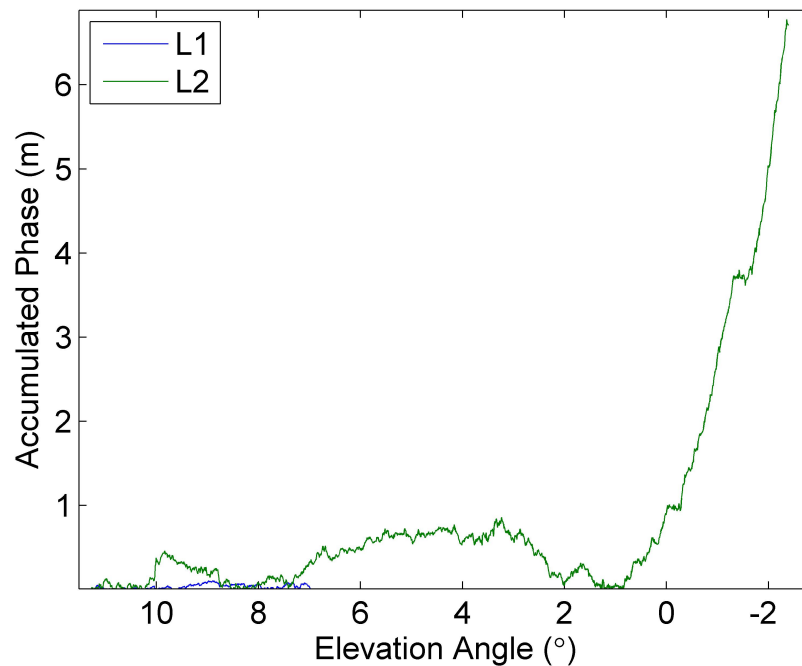

Figure 3.15: Comparison of the accumulated phase, as calculated from open-loop tracking with a line-of-sight Doppler model, on f_{L1} and f_{L2} for PRN 17. Loss of lock on the L1 signal is apparent at an elevation angle of 7°. An accumulated phase of approximately 6.5 meters is seen on the L2C signal over the course of the setting occultation.

as described in Sections 2.3 and 2.4 and Zuffada et al. (1999) [94]. The focus of this experiment, however, was to provide insight into the core receiver implementation for a RO specific GPS receiver. The development of the algorithms and software to process the GPS L1, L2C, and L5 signals provided an understanding to their respective signal structures, power levels, and implementation quirks. Results from this experiment provide useful insight into the optimal signal/modulation choice for a future RO receiver. OL tracking successfully provided carrier frequency measurements from both of the new modulations (L2C and L5). The increased signal strength allowed for collection beyond the optical horizon, but at the cost of increased signal processing complexity [7, 6].

Chapter 4

RADIO OCCULTATION CONSTELLATION STUDIES

The previous chapter's investigation into the implementation of a receiver capable of collection of the modernized GPS signals leads to the question of what are the potential quantitative benefits of full GNSS constellation utilization for RO. As of March 2013, the entire COSMIC constellation provides 1,500 RO soundings per day from GPS occultations [3]. Future constellations of RO satellites should achieve and surpass this number. Optimization of occultation events can be achieved with the utilization of the growing GNSS constellations and different orbit arrangements. Studies of future RO constellation configurations were conducted to predict the quantity and distribution of potential occultation events. Maximization of occultation events is key to producing sufficient measurements for NWP applications.

4.1 Constellation Simulations

The RO constellation simulations, implemented in STK/MATLAB, focused on the total occultation count and dissemination of these events as a function of number of occultation satellites, altitude, inclination, and total analysis time. The simulations share the same premise that the occultations occur between constellations of LEO satellites and the GNSS satellites, specifically signals from GPS, GLONASS, Galileo, and BeiDou. The simulations were at a future date to account for the time necessary to build and deploy the envisioned constellations. The GNSS constellations were updated to reflect documented estimates of satellite numbers and orbit parameters at each date. A description of the process to simulate and obtain these occultation opportunities is

presented in the next section, followed by the results of three different occultation simulations.

4.1.1 Simulation Description

To initialize the simulations, the GNSS constellations were loaded from the STK satellite database, which acquired their ephemeris and metadata from Celestrak and other sources. The GPS satellites were propagated by STK using the algorithms described by the GPS Directorate, while the propagation of the other GNSS constellations relied on SGP4 orbit determination [27, 86]. The Galileo and BeiDou systems were not fully populated as of 2015, and therefore only existing satellites were found in the STK database. These constellations were completed by simulating the planned satellites using the orbital characteristics of existing satellites and the constellation design parameters given in the ICDs [24, 14].

A field of view boundary of 55° was imposed from bore sight of the fore and aft antennas on the RO satellites. The line-of-sight (LOS) access between the RO satellites and the GNSS satellites was calculated to be within 1 cm of the Earth's surface. The occultation times and locations were only reported for the exact moment of intersection between the LOS vector and the Earth's surface. The latitude and longitude of the line-plane intersection point was imported to MATLAB and plotted against a two-dimensional projection map of the Earth.

Given a seed RO satellite of a given altitude, inclination, and eccentricity, identical satellites were then simulated as a Walker constellation [88]. The identical satellites were evenly spaced about the desired number of orbit planes, and the planes were equally spaced about the longitude of the ascending node. The RO satellites were propagated using STK's $J4$ method, which takes into account the point-mass accelerations of two-body dynamics and the dominant effects of Earth oblateness (represented by the gravity field model terms $J2$ and $J4$). The simulations described in the following sections study the effects of varying the orbital parameters of the initial seed satellite, the total number of occultation satellites, and the duration of the occultation simulation on the total occultation events and their distribution.

4.1.2   Number of Occultation Satellites

The first simulation described here studied the effect of additional RO satellites on Earth coverage. The quantity and distribution of occultation events were found from 1, 2, 3, 4, 5, and 6 RO satellites in sun synchronous circular orbits. The satellites were placed at 800 km altitude at an inclination of 98.696°. Each satellite occupied its own plane, which were spaced equally about the Earth. The projected GNSS constellations as of 2017 are shown in Table 4.1.

Table 4.1: The GNSS constellation status as of 2017 [25, 19]. The GPS constellation executes an "Expandable 24" configuration, where 3 of the additional satellites have become part of the constellation baseline [82].

Constellation	# Satellites	Orbital Planes	S/C per Plane	Spares
GPS	32	6	4 (3)	5
GLONASS	24	3	8	0
Galileo	26	3	8	2
BeiDou	27	3	9	0

For brevity, the occultation event results are shown only for the one, three, and six satellite cases. The occultation event coverage of the Earth's surface with one RO satellite for the simulation period of one day is shown in Figure 4.1. Figure 4.2 shows histograms describing the latitude distribution of the occultations by constellation type. 2,675 possible occultations events were found from the single RO satellite in a sun-synchronous orbit over 24 hours.

The results shown in Figure 4.3 are for three occultation satellites, place 120° apart in longitude of ascending node. The latitude distributions for each constellation are shown in Figure 4.4, with 8,053 total occultations over the course of one day.

Finally, the distributions of occultation events are shown for six RO satellites in sun synchronous orbits in Figures 4.5 and 4.6. This configuration results in 16,098 occultations per day. If the 2,500 COSMIC occultations (at its peak performance) were scaled up to the future 2017 GNSS constellation, this would result in approximately 8,516 occultations per day. Although the COSMIC satellites employ a field of view bandwidth of about ±45° in comparison to the ±55°

used here, the simulation results indicate that the highly inclined orbits of a sun synchronous system could provide additional occultation opportunities in comparison to the existing COSMIC RO constellation at 72° inclination.

4.1.3   Occultation Analysis Period

In the second simulation, the effect of the period of analysis was assessed for a single RO constellation. The distribution of the occultation events over relatively short time intervals (several hours) is important to weather prediction applications. The simulated constellation was similar to the COSMIC constellation with an altitude choice of 800 km and inclination of 72°. However, twelve satellites were split into six orbital planes, where two antipodal spacecraft occupied each plane. The time periods of interest for the simulation were 100 minutes (or approximately the length of one orbital period of the RO satellite), 3 hours (provides needed data for the numerical weather prediction 3-hour forecast), 12 hours (approximate period of one orbit of the GNSS satellites), and one day. Because of the increased number of RO spacecraft, the simulation timeframe was set to 2020 as the additional spacecraft take more time to build and launch. The projected GNSS constellations as of 2020 are shown in Table 4.2.

Table 4.2: The GNSS constellation status as of 2020 (full population of constellations) [25, 23].

Constellation	Num Satellites	Orbital Planes	S/C per Plane	Spares
GPS	32	6	4 (3)	5
GLONASS	24	3	8	0
Galileo	30	3	10	0
BeiDou	27	3	9	0

Figures 4.7 and 4.8 provide the simulated results of a twelve satellite RO constellation for just one orbital period of the LEO satellites. In total, this constellation provided 2,027 occultation opportunities over 100 minutes from the full GNSS constellations.

Over three hours, a length of time important to numerical weather prediction, the coverage of occultation constellation is shown in Figure 4.9 and distribution by constellation in Figure 4.10.
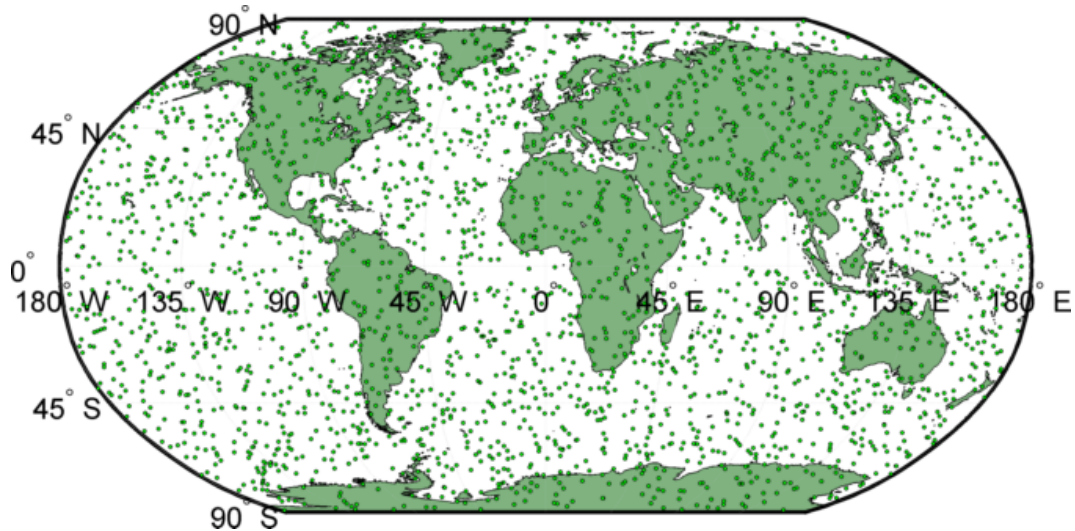
Figure 4.1: Occultation event locations over one day from one sun-synchronous RO satellite at an 800 km altitude circular orbit using the four GNSS constellations (GPS, GLONASS, Galileo, and BeiDou) in 2017.
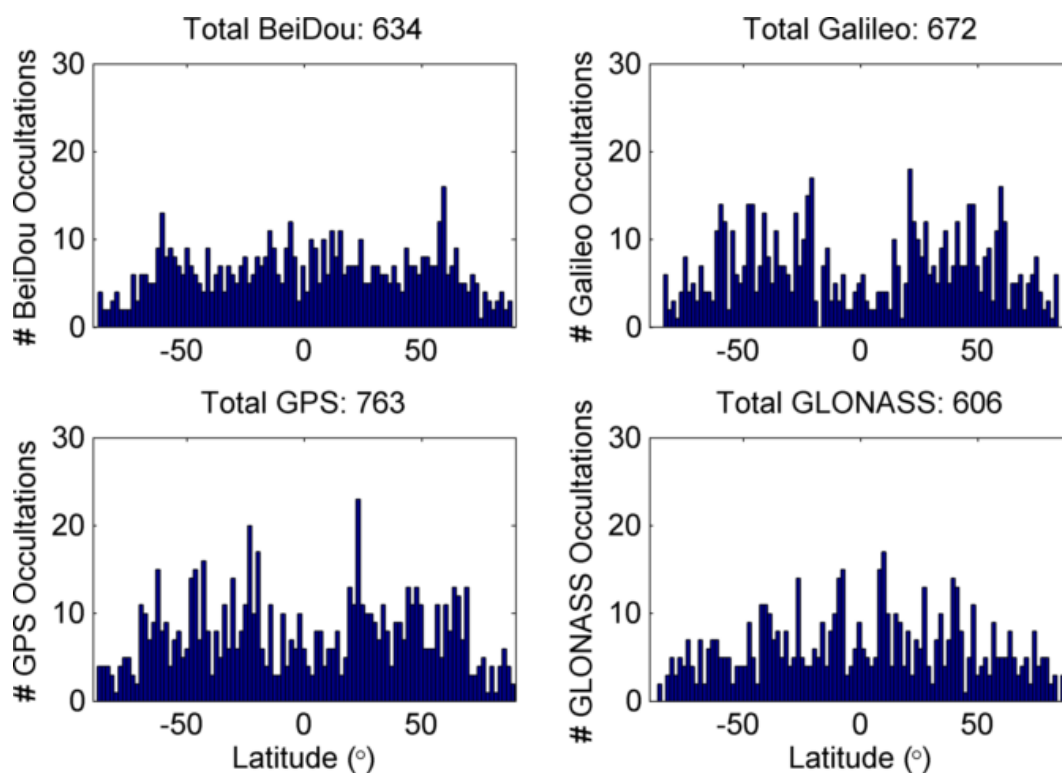
Figure 4.2: Histograms of the occultation events over one day as a function of the surface tangent point latitude, broken down by source GNSS signal. The total occultations by constellation are given in the title.
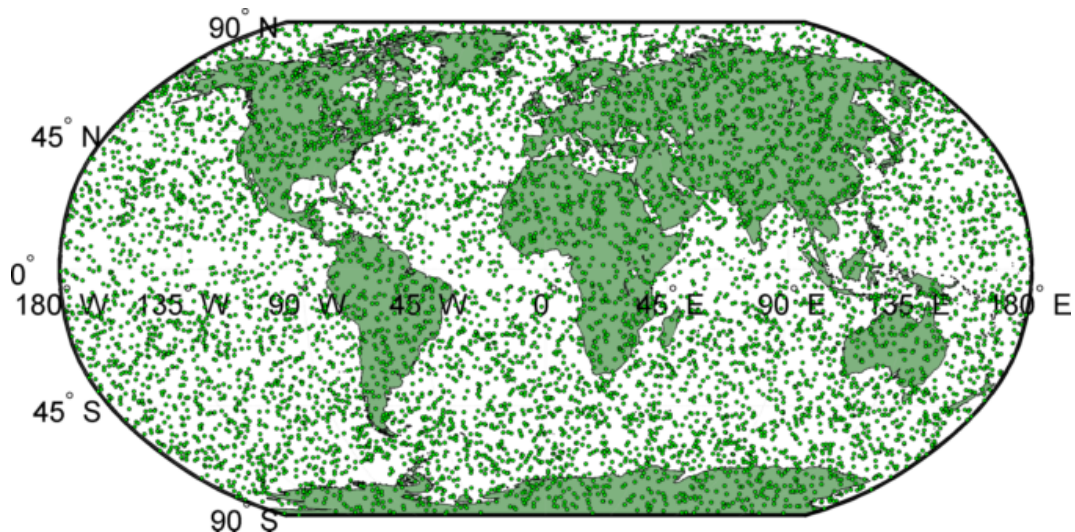
Figure 4.3: Occultation event locations over one day from three sun-synchronous RO satellites at an 800 km altitude circular orbit using the four GNSS constellations (GPS, GLONASS, Galileo, and BeiDou) in 2017.
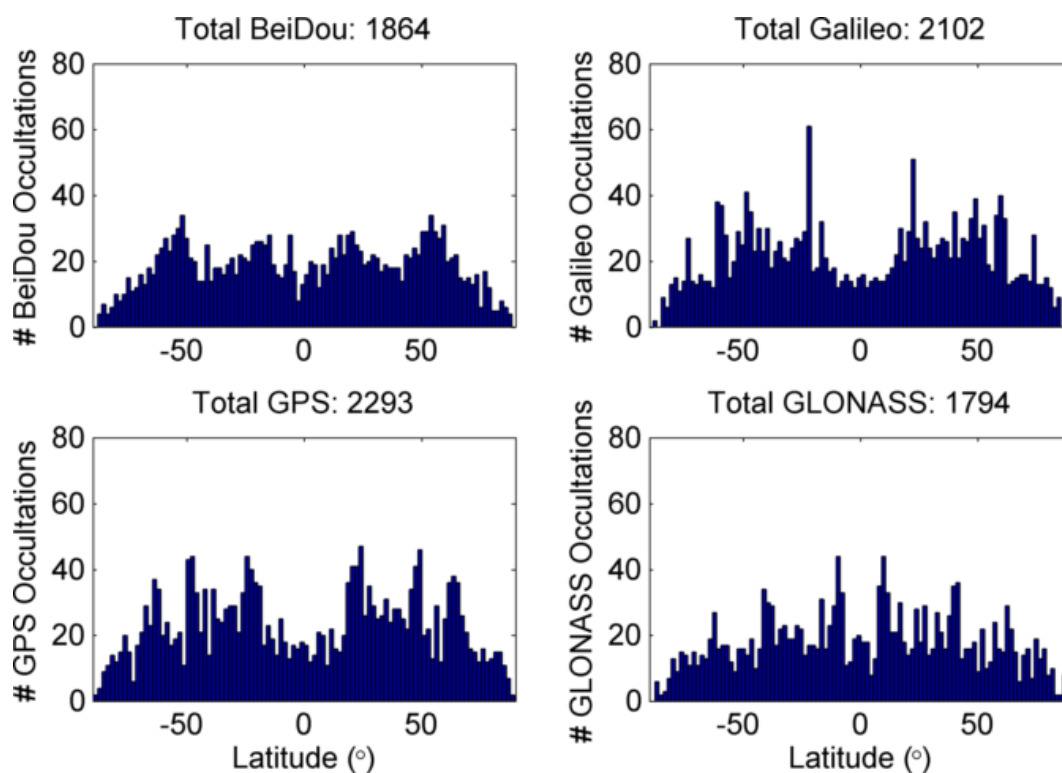
Figure 4.4: Histograms of the occultation events over one day as a function of the surface tangent point latitude, broken down by source GNSS signal. The total occultations by constellation are given in the title.
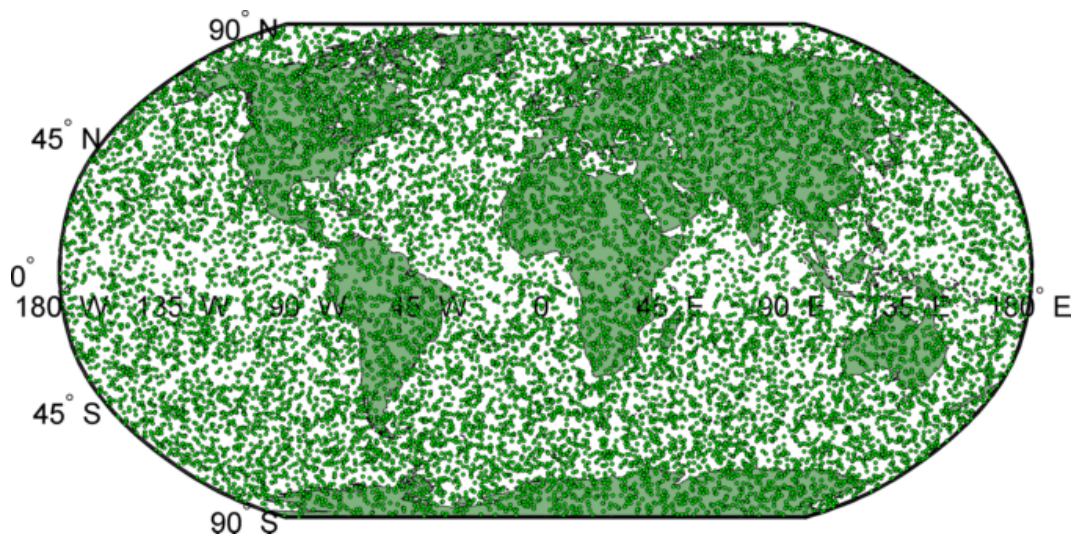
Figure 4.5: Occultation event locations over one day from six sun-synchronous RO satellites at an 800 km altitude circular orbit using the four GNSS constellations (GPS, GLONASS, Galileo, and BeiDou) in 2017.
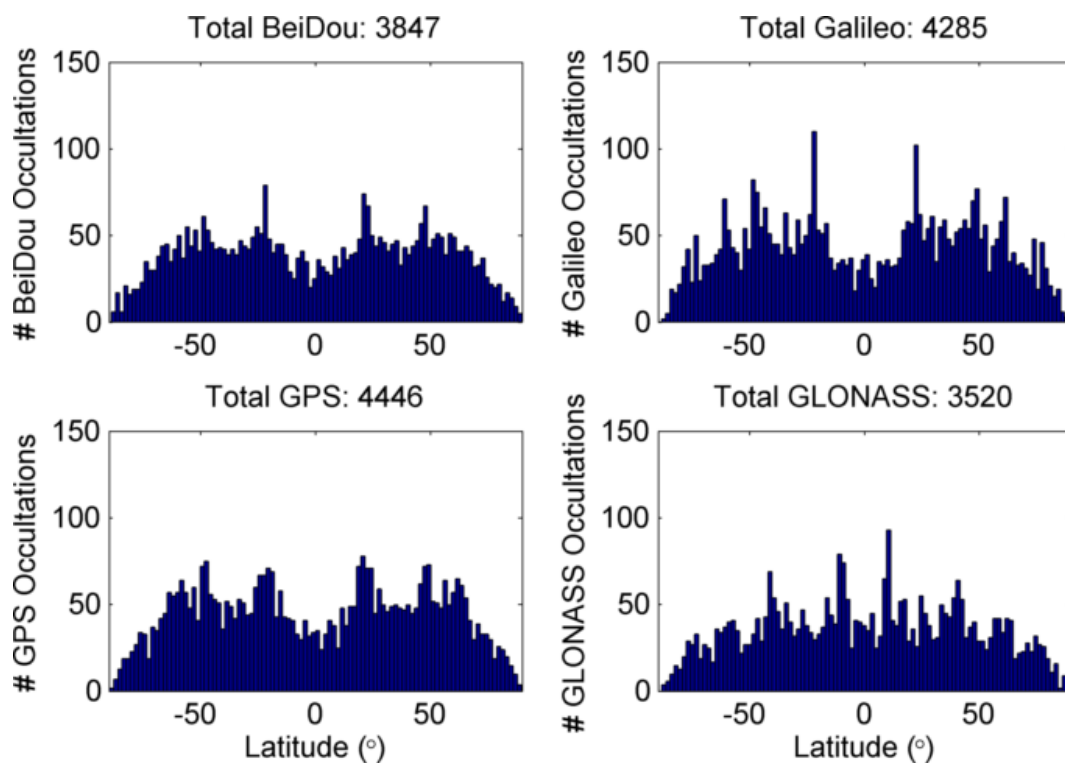
Figure 4.6: Histograms of the occultation events over one day as a function of the surface tangent point latitude, broken down by source GNSS signal. The total occultations by constellation are given in the title.

3,647 total occultation events were found.

Figures 4.11 and 4.12 show the results from one approximate orbital period of the GNSS constellation satellites, where 14,523 occultation opportunities were found.

Finally, the one day results for coverage and latitude/constellation distribution are shown in Figures 4.13 and 4.14. 29,001 total occultation opportunities were recorded over the course of one day. If the current COSMIC constellation was scaled from the five functional satellites to twelve, and the full GNSS constellation of 2020 is used, the predicted daily total amount of occultations would be approximately 12,713. This is significantly less than the simulated value found here. One possible reason for the difference is that the COSMIC constellation may have a reduced field of view in comparison to the simulation described here. The COSMIC constellation may not be processing or reporting all possible geometric occultation opportunties, as shown in the simulations here.

4.1.4   High Density RO Network

The final simulation examined the concept of combining high density communication satellite networks with remote sensing. Some missions, such as the O3B and Inmarsat networks, are built to purposefully cover the globe at sufficient signal strength for communications applications [56]. Satellite networks such as these could also be equipped with an occultation receiver and be used for remote sensing using the GNSS constellations.

This simulation analyzed the coverage and occultation opportunities of a very large RO constellation consisting of 400 satellites. These satellites were split into 20 orbital planes with 20 occultation satellites per plane. The satellites move in circular orbits of $1,300$ km altitude and $66°$ inclination. Using the predicted GNSS constellations of 2020 shown in Table 4.2, a three-hour simulation was performed. Figure 4.15 shows the occultation coverage from this large constellation projected on a two-dimensional map. Over three hours, near complete coverage of the Earth's surface was shown with 94,807 occultation opportunities, including denser coverage in the mid-latitude regions.

Of particular interest was the number of occultations over regions known to spawn tropical
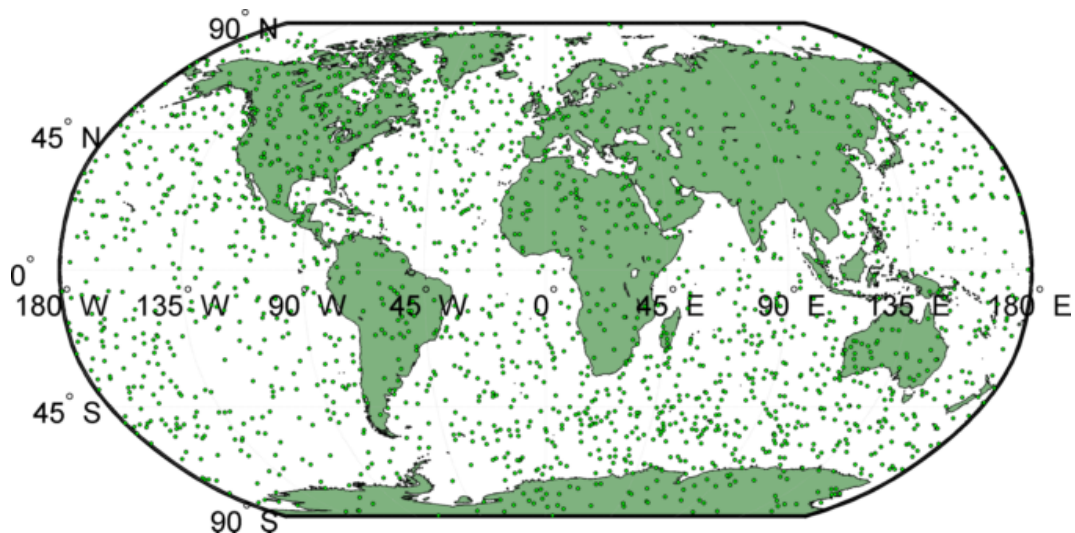
Figure 4.7: 100 minute-long simulation of the occultation events produced by 12 occultation satellites at 800 km circular orbits at 72° inclination.
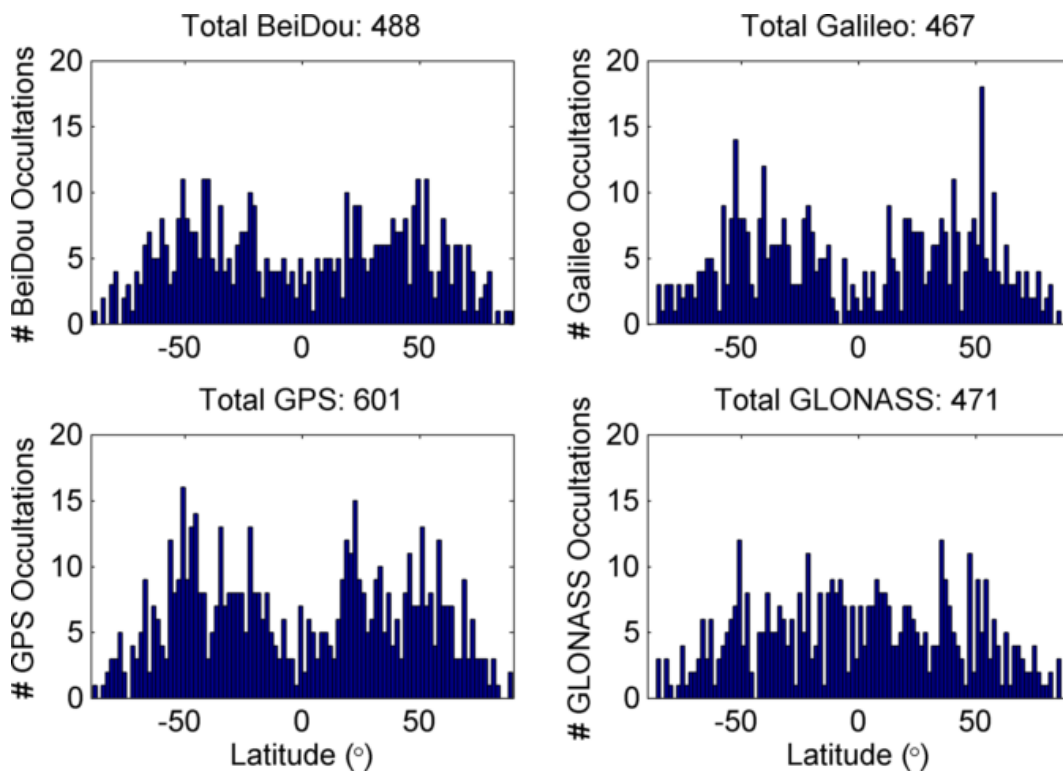
Figure 4.8: Histograms of the occultation events for the 12-satellite configuration over 100 minutes as a function of the surface tangent point latitude, broken down by source GNSS signal. The total occultations by constellation are given in the title.
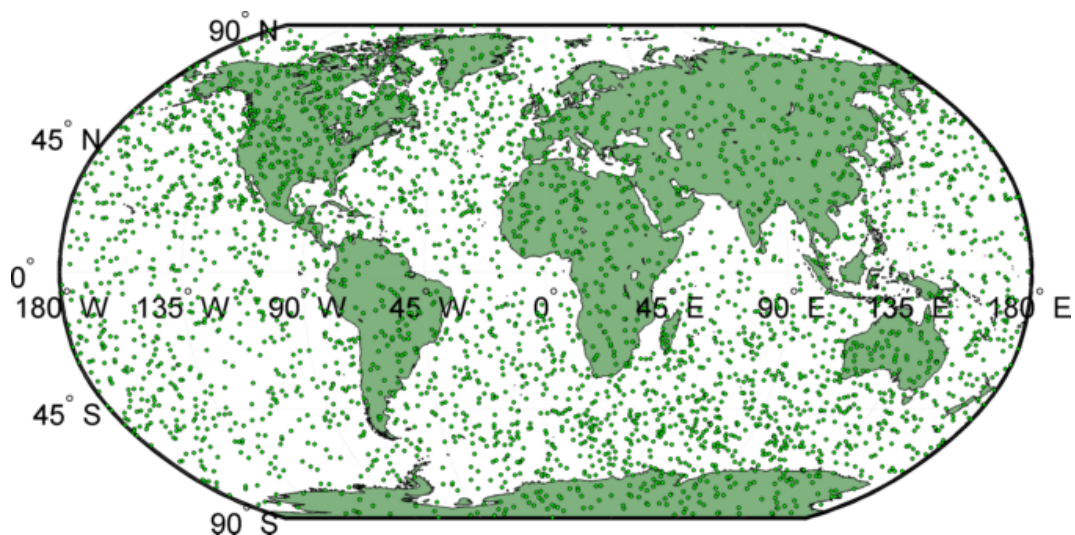
Figure 4.9: Three hour-long simulation of the occultation events produced by 12 occultation satellites at 800 km circular orbits at 72° inclination.
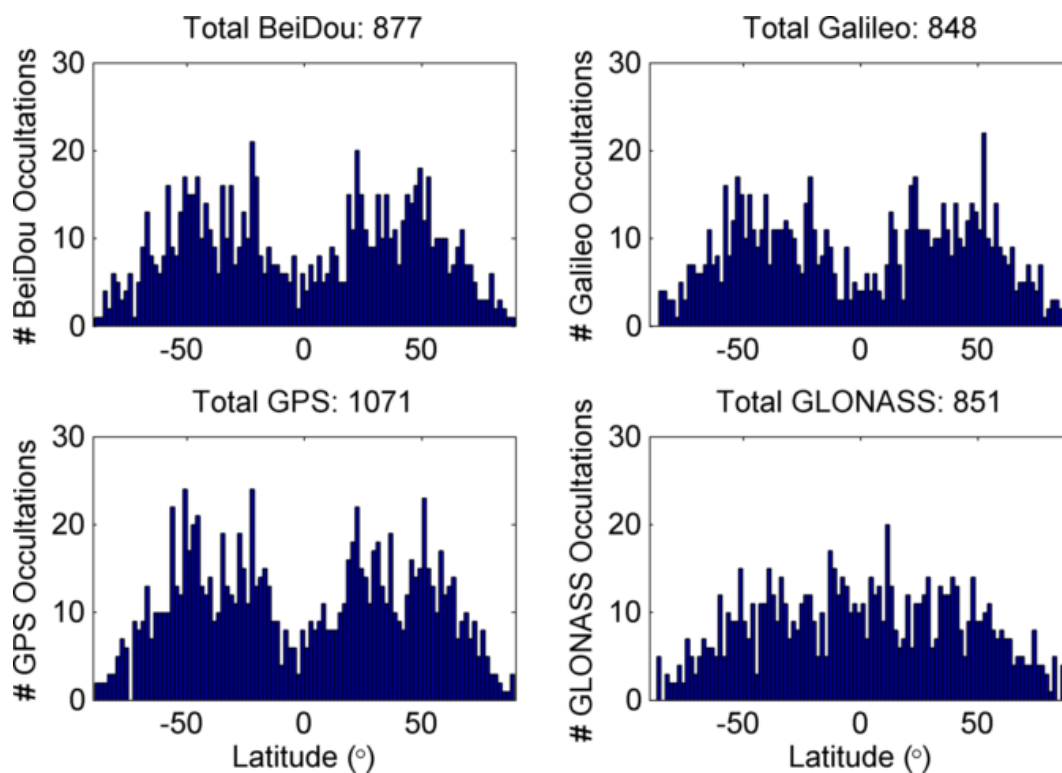
Figure 4.10: Histograms of the occultation events for the 12-satellite configuration over 3 hours as a function of the surface tangent point latitude, broken down by source GNSS signal. The total occultations by constellation are given in the title.
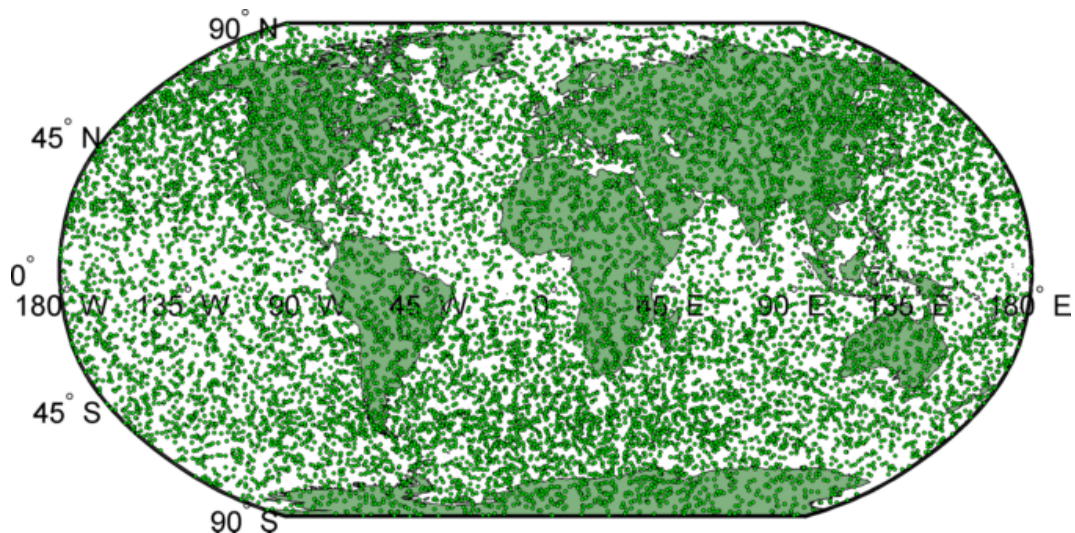
Figure 4.11: Twelve hour-long simulation of the occultation events produced by 12 occultation satellites at 800 km circular orbits at 72° inclination.
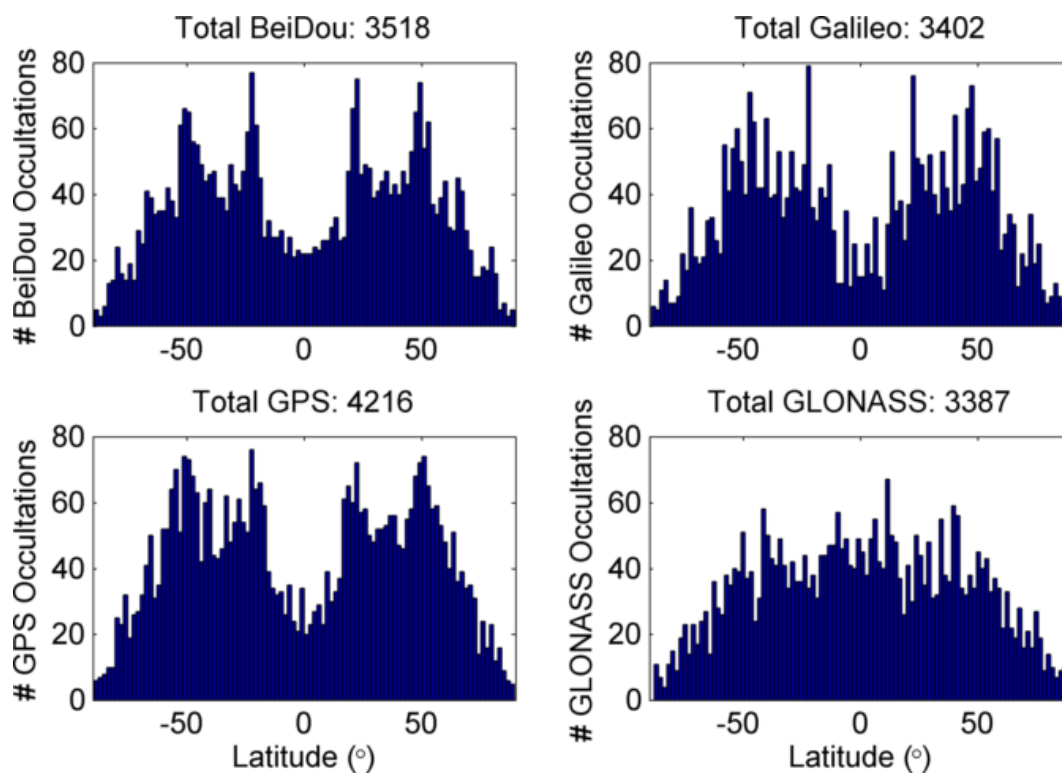
Figure 4.12: Histograms of the occultation events for the 12-satellite configuration over 12 hours as a function of the surface tangent point latitude, broken down by source GNSS signal. The total occultations by constellation are given in the title.
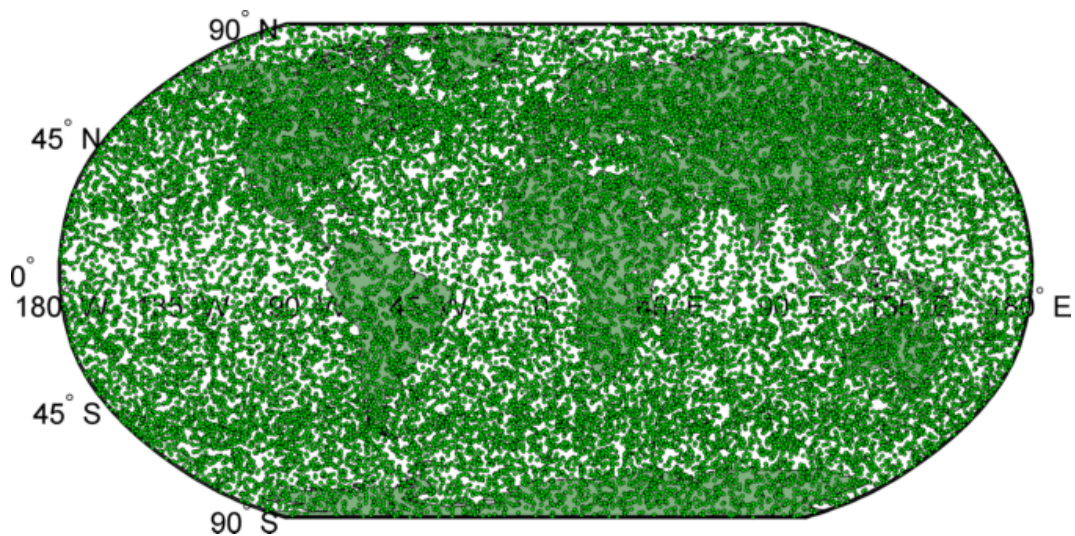
Figure 4.13: One day-long simulation of the occultation events produced by 12 occultation satellites at 800 km circular orbits at 72° inclination.
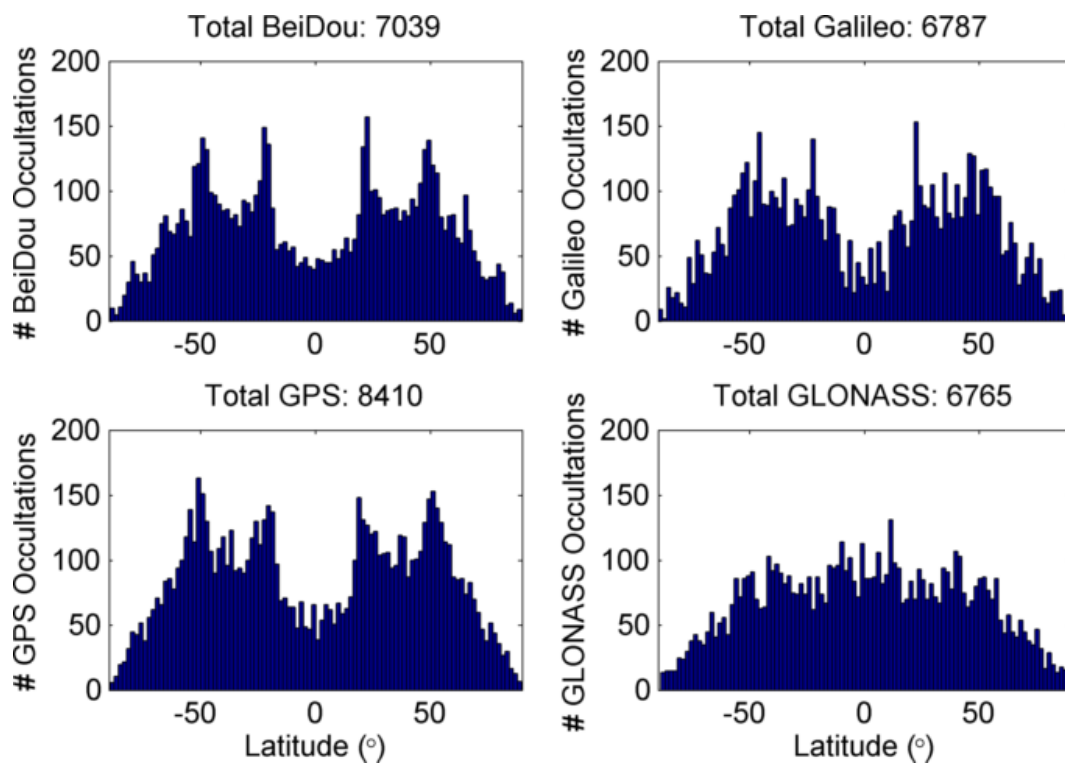
Figure 4.14: Histograms of the occultation events for the 12-satellite configuration over 1 day as a function of the surface tangent point latitude, broken down by source GNSS signal. The total occultations by constellation are given in the title.
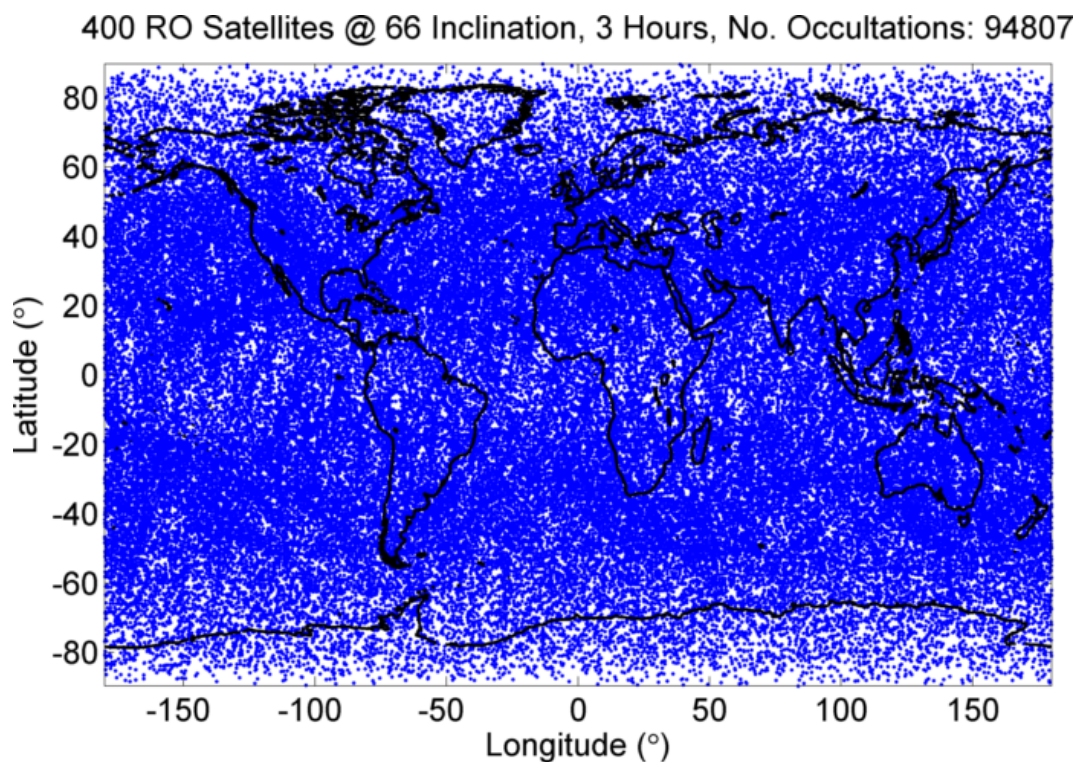
Figure 4.15: Three hour-long RO coverage map with 400 occultation satellites. The occultation satellites are distributed as 20 satellites per 20 orbital planes, equally spaced in longitude of the ascending node and at 66° inclination. The predicted GNSS constellations (GPS, GLONASS, Galileo, and BeiDou) as of 2020 are used for signal sources.

storms and cyclones. Figure 4.16, obtained from the National Weather Service, shows the seven regions of the Earth where cyclones tend to form. The coverage shown in Figure 4.15 was reduced to these seven regions in Figure 4.17 for three hours. The dense coverage from occultation opportunities of the large RO network will provide the real-time data necessary for the NWP analysis. The addition of RO collection capabilities to planned, large LEO constellations could be highly beneficial to NWP services, as real-time dense coverage of the Earth's surface is found in a fraction of the time of the current RO missions.
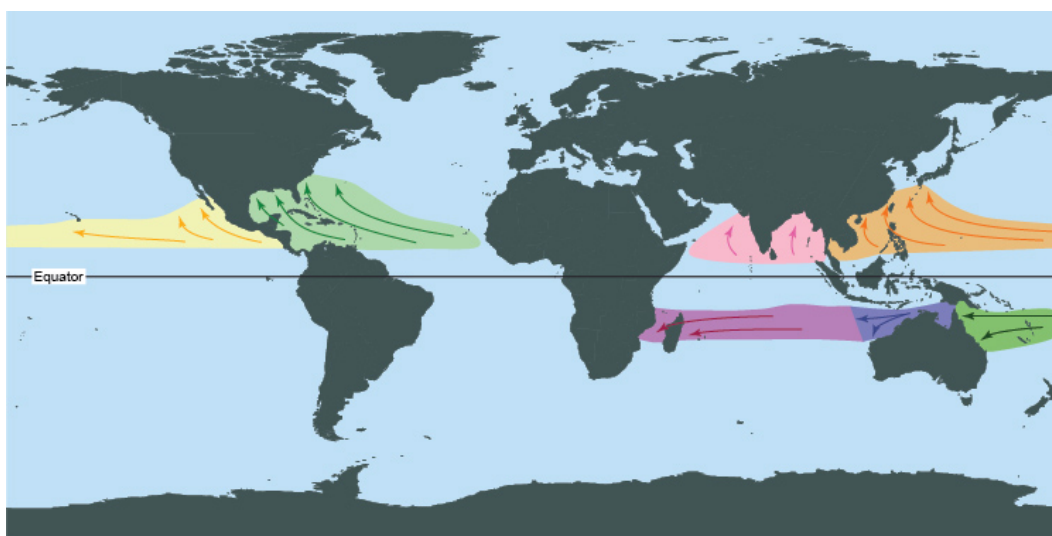
Figure 4.16: The seven regions on the Earth where tropical cyclones regularly form. Image courtesy of the National Oceanic and Atmospheric Administration (NOAA) [65].
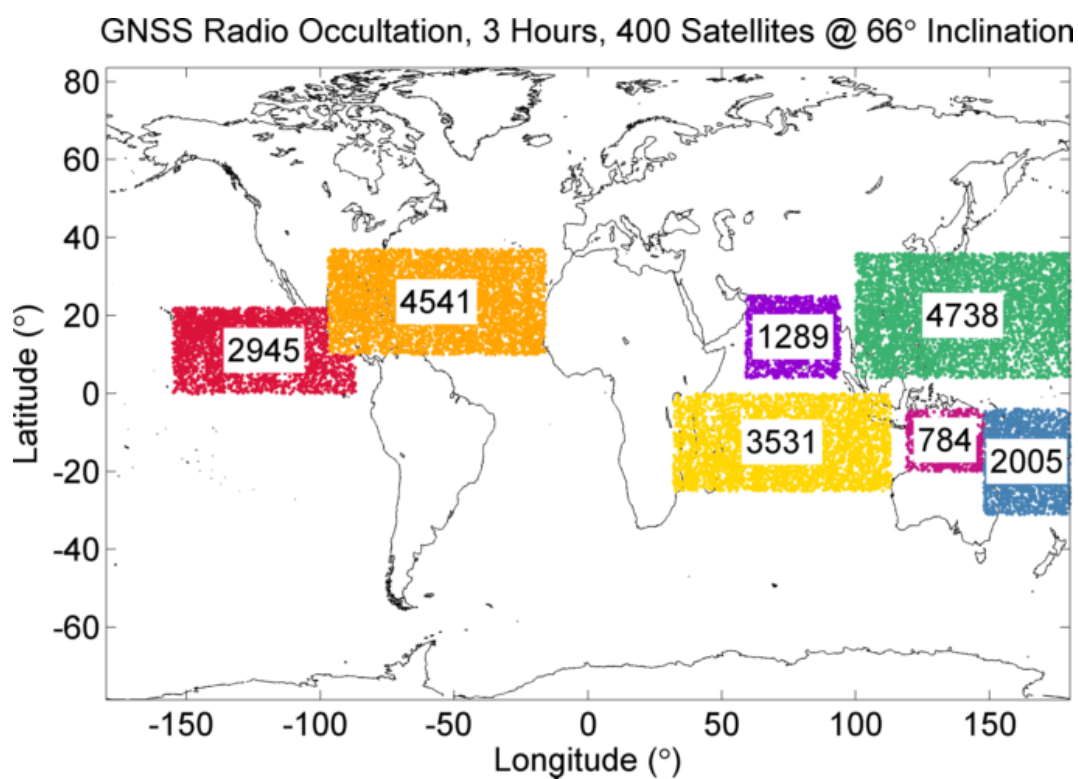
Figure 4.17: Three-hour coverage of cyclone regions using the simulated 400 RO satellite constellation.

4.2   Simulation Outcomes

The simulations shown here provide some insight to the planning and design of a future RO system. Applications that require very timely data, such a severe weather prediction, can note the coverage maps and distributions from the 100-minute and three-hour simulations for their planning purposes. Higher inclinations, such as sun synchronous orbits, may provide more geometric occultation viewing opportunities in comparison to previous RO missions. The most significant conclusion from these studies is that complete and timely coverage of the Earth's surface is most easily obtained with more occultation satellites. Using existing or planned missions, such as space-based communications applications, from which the satellites can operate the occultation mission can greatly increase the amount of real-time data acquired for weather prediction and climate change studies, especially in geographical areas known for cyclone formation.

Chapter 5

ORBIT DETERMINATION AND SCHEDULING

Utilization of all signal sources is advantageous for future occultation missions, as shown in the constellation simulations of Chapter 4. Knowledge of the position and motion of the LEO occultation satellite, as well as estimation of the locations of the GNSS satellites, is required for prediction of future occultation events. All GNSS satellites produce navigation messages in a broadcast ephemeris that updated once per day. The location and velocity of the LEO satellite, however, are a larger challenge to estimate and are typically determined through a combination of precise modeling and real-time observations. Prediction of upcoming occultation collection opportunities between the RO and GNSS satellites relies heavily on the accuracy of the orbit estimations. This chapter addresses the orbit determination (OD) of a LEO occultation satellite, propagation of the various GNSS constellations, and prediction of possible occultation events between the LEO and GNSS satellites.

5.1   Real-time Orbit Determination

For space-based GNSS collections, the relative motion between the transmitter and receiver results in large Doppler shifts. For example, an RO satellite at an 800 km circular orbit could experience a maximum Doppler shift to the GNSS signal of approximately 60 kHz. Ground-based GNSS receivers are typically subject to Doppler shifts of ± 5 kHz for stationary data collections and up to ± 10 kHz for high-velocity scenarios [10, 26]. Because large Doppler shifts are common to space-based receivers, ordinary ground-based GNSS receivers are inadequate for tracking signals

in space. A class of specialized receivers have been developed to account for the large velocities of space-based navigation. The dual-frequency BlackJack, IGOR, and GRAS receivers are used on a variety of LEO missions for signal collection and navigation. These receivers offer accuracies of $10 - 30$ cm in pseudorange and $0.5 - 2$ mm for carrier phase measurements [61].

RO requires very precise OD solutions for both LEO and GNSS satellites for the retrieval of the science data. This is done on the ground in post-processing and requires the position and velocity estimates of the LEO satellite to be accurate to $10 - 20$ cm and $0.1 - 0.2$ mm/s (3D RMS), respectively [74, 59, 60]. Orbital velocity errors of less than 0.05 mm/s 3D RMS are small and should not limit retrieval accuracy at any altitude [51]. Orbital velocity error affects the RO data retrieval process primarily through the component of the velocity error projected along the ray path, which translates to error in the Doppler frequency.

The navigation accuracy requirements are more relaxed for an onboard occultation scheduler and necessitate real-time position and velocity solutions with sufficient accuracy for open-loop tracking. The narrow-band digital recording (NBDR) technique, developed for the BlackJack and IGOR receivers, allows for a modest data volume of data downlink during open-loop tracking at a 50 Hz bandwidth [4]. For scheduling purposes, the NBDR method requires pseudorange modeling accuracy to within one C/A chip, or 300 meters. Satisfactory phase reconstruction using open-loop tracking is possible if the mean pseudorange error is within 100 meters and Doppler mismodeling is less than approximately 10 Hz [77], which translates to a line-of-sight velocity error of approximately 1.9 m/s (combined for both satellites). As the NBDR tracking method incorporates both the first-order atmospheric model and OD navigation estimates, the orbit mismodeling should only contribute to a fraction of the total error.

Real-time OD for satellites in LEO using GPS measurements and ephemerides are fairly common in literature. The most accurate results are shown from navigation filters using dual-frequency code carrier phase observations and gravity model. One of which, described by Montenbruck and Ramos-Bosch (2007), shows 0.5 m and ≤ 1 mm/s 3D RMS orbit accuracy for data obtained from LEO missions varying from 400-800 km altitude [61]. In their study, measurements from the

BlackJack, IGOR, and GRAS receivers on CHAMP, GRACE-A, TerraSAR-X, ICEsat, SAC-C, and MetOp-A were used to test an extended Kalman filter (EKF) in a real-time orbital data processing scenario as would a space-based OD receiver. Another study shows orbital accuracies of 0.5 m position and 0.5 mm/s velocity 3D RMS produced by the GRAS receiver on MetOp-A [60]. Fairly accurate OD has even been demonstrated by the low-cost GPS receiver, Phoenix-XNS, where ionosphere-free code and carrier measurement combinations were shown to produce orbits with position accuracy of 1.1 m 3D RMS on the PROBA-2 satellite [62]. The GRoup And Phase Ionospheric Correction (GRAPHIC) combination described by Yunck (1996) allows for a simple, single-frequency approach, and has been shown to produce orbit accuracies of 0.6-1 m 3D RMS [93, 61]. Single-frequency approaches are best suited for LEO satellites at higher orbital altitudes and under minimal solar activity [8].

Position and velocity estimates from current OD engines provide navigation accuracy to well within the orbit/atmospheric modeling requirements of the NBDR technique used by the receivers on COSMIC. The EKF using dual-frequency carrier phase observations provides sub-meter 3D RMS position accuracy and $0.5 - 1\,\mathrm{mm/s}$ 3D RMS velocity accuracy. Orbits with accuracy approaching the required values for the stringent RO post-processing requirements can be obtained with near-real time orbit and clock products from the GRAS Support Network (GSN) and RETICLE system [60], but these have a latency associated with them and cannot be used for prediction algorithms, such as an occultation scheduler. Future work in OD engines could provide sufficient accuracy for processing of RO retrievals on-orbit and in real-time.

5.2   Occultation Scheduler

Under the assumption that a navigation engine with sufficient accuracy could be constructed or obtained, an autonomous occultation prediction and scheduling routine was developed. The algorithms shown here allow for the collection and scheduling of all GNSS constellations solely from their broadcast ephemeris messages. Two methodologies support the detection of occultation events: 1) by an elaborate link budget model calculation or 2) by LOS geometry. As the link budget

calculation requires advanced knowledge of the antenna gain pattern and orbit characteristics, a more simplistic geometric model is described here.

5.2.1   Geometric Interpretation

For a geometric LOS occultation calculation, the minimum distance was found between the line segment formed between the GNSS satellite and the LEO satellite and the center of the Earth. Figure 5.1 shows the geometry of the minimum distance, d, between the point x_0 and the line segment formed by points, x_1 and x_2. The formula for d is as follows.

$$d = \frac{|(\mathbf{x_2} - \mathbf{x_1}) \times (\mathbf{x_1} - \mathbf{x_0})|}{|\mathbf{x_2} - \mathbf{x_1}|} \tag{5.1}$$

The minimum distance is limited to the occultation region of interest, namely a vertical distance above and below the Earth's surface. For the purposes of this simulation, the vertical bounds for the occultation were set to $R_{Earth} - 200 \, \text{km} \leq d \leq R_{Earth} + 150 \, \text{km}$.
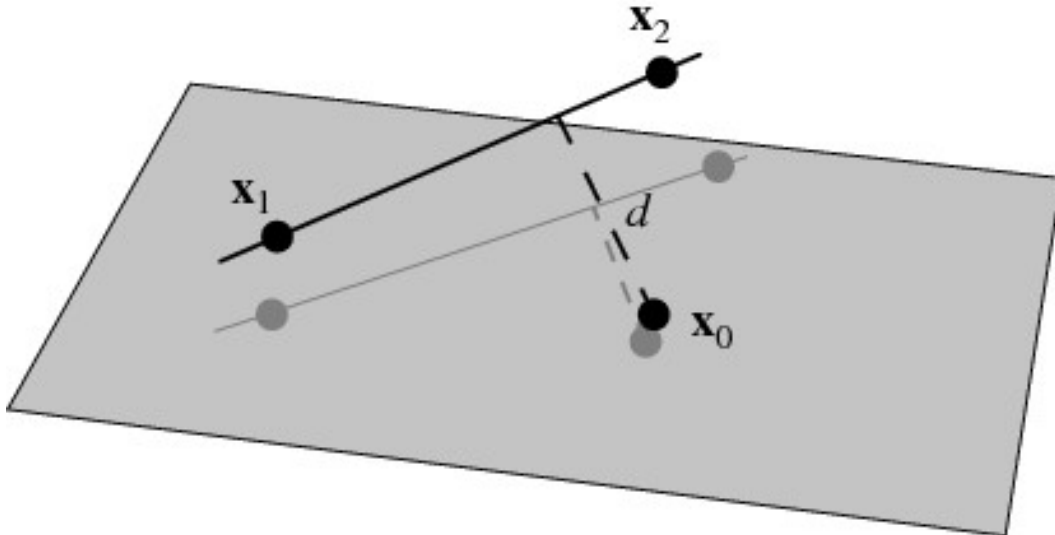
Figure 5.1: Minimum distance, d, between a point and line segment in three-dimensional space. For the purposes of the occultation scheduler, x_0 is the center of the Earth, and x_1 and x_2 are the RO and GNSS satellites, respectively. Image courtesy of Wolfram Mathworld [90].

To ensure that the point of minimum distance exists on the line segment created by the points x_1 and x_2 and not just on the infinite line defined by these points, the parameter, t, must

be positive in the following equation.

$$t = -\frac{(\mathbf{x_0} - \mathbf{x_1}) \cdot (\mathbf{x_2} - \mathbf{x_1})}{|\mathbf{x_2} - \mathbf{x_1}|^2} \tag{5.2}$$

If a LOS vector exists between the two satellites and it is shown to pierce the Earth's atmosphere, the azimuth angle of the vector must be validated to be within the field of view of the fore or aft antenna of the occultation satellite. First, the LOS vector is rotated from the Earth-Centered, Inertial (ECI) frame to the Radial-In track-Cross track (RIC) with the following matrix [9].

$$\vec{R} = \frac{\vec{r}}{|\vec{r}|} = \frac{X}{r}\hat{i} + \frac{Y}{r}\hat{j} + \frac{Z}{r}\hat{k}, \tag{5.3}$$

$$\vec{C} = \frac{\vec{h}}{|\vec{h}|} = \frac{\vec{r} \times^{ECI} \dot{\vec{r}}}{|\vec{r} \times^{ECI} \dot{\vec{r}}|}, \tag{5.4}$$

$$\vec{I} = \vec{C} \times \vec{R} \tag{5.5}$$

$$\beta_{RIC}^{ECI} = \begin{bmatrix} R_x & R_y & R_z \\ I_x & I_y & I_z \\ C_x & C_y & C_z \end{bmatrix} \tag{5.6}$$

Using this direction cosine matrix, the position vector is rotated from ECI to RIC as

$$\begin{bmatrix} R \\ I \\ C \end{bmatrix} = \beta_{RIC}^{ECI} \begin{bmatrix} X \\ Y \\ Z \end{bmatrix} \tag{5.7}$$

Once rotated to the RIC frame, the arctangent of the radial and in track components is taken to find the azimuth angle. It is then evaluated against the field of view bounds (typically set to $\pm 55°$ of bore sight). If the evaluation of these tests are proven to be true, an occultation event is noted and the time and GNSS satellite are recorded.

5.2.2   Scheduler Simulation

A test case was developed for the scheduler to validate the orbit propagation, timing and coordinate system transformations, and the scheduling algorithm abilities. The scheduler is designed

to be autonomous, meaning it has the capability to propagate and find geometric occultation events given only the initial conditions provided in the GNSS ephemeris messages and the time of propagation. As a result, the start times and durations of the predicted occultation events are given. In addition, occultation statistics and metrics are provided to assist in the data handling capabilities of a future RO system.

The orbit simulation was initialized to 1-Jan-2015, 00:00:00.000 UTC, using the GNSS orbit information from the broadcast navigation messages [43]. The ephemeris and almanac information obtained from the IGS broadcast file was translated to a format as produced by the software defined radio (SDR) developed by CU. The ephemeris contains only three BeiDou mid-Earth orbit (MEO) and three Galileo satellites, as that mirrors the true GNSS status as of 1-Jan-2015. The GNSS orbits were propagated from their initial states using the algorithms described in their respective ICDs [27, 71, 24, 14]. Common coordinate (ECI) and timing (UTC) systems were realized through the required transformations.

A fictitious occultation satellite was created for the purposes of this simulation. The satellite was placed in an 800 km altitude circular orbit about the Earth at $72°$ inclination (similar to a COSMIC satellite). The software package STK was used to initialize and propagate the new RO satellite using two body dynamics and the $J2$ and $J4$ perturbation coefficients. STK reported position and velocity values for the RO satellite at a $1\,\mathrm{Hz}$ rate in the ECI coordinate and UTC timing systems. On orbit OD accuracies for this satellite were assumed to be consistent with what is shown in literature, as described in Section 5.1.

The GNSS constellations and RO satellite were propagated for a single orbit period of the occultation satellite, or approximately 6073 seconds. Using the algorithms given in Section 5.2.1, a $\pm 55°$ field of view azimuthal bound on the fore and aft antennas, and a vertical bound of $-200\ \mathrm{km} \leq d \leq 150\ \mathrm{km}$ from the Earth's surface, a list of possible occultation events and their times were calculated. Recorded were the initial start times, dates, and other useful metrics for RO receiver development. The satellite identifications (ID) and constellation are documented, as these parameters affect the data collection rates, frequencies, modulations, and eventual storage

size for the raw signal capture. The duration of the occultation, whether it is rising or setting, and the latitude and longitudinal drift parameters were also catalogued.

The scheduling results from a single orbit simulation of a potential occultation satellite are shown here. Possible occultation signal sources include the 32 GPS satellites, 24 GLONASS satellites, 3 operational Galileo satellites, and 3 BeiDou MEO satellites. Figures 5.2 - 5.5 show the scheduling results as a timeline for the individual constellations. A combined timeline of all constellations and tabular occultation results for a partial orbit of the LEO occultation satellite can be found in Appendix A, and not shown here.

The occultation opportunities between the LEO RO satellite and the GPS constellation are visually shown in Figure 5.6. The LEO and GPS satellites are plotted in green and red, respectively, over the course of a single orbit of the LEO satellite. If LOS access exists between the satellites after consideration of the antenna field of view and vertical tangent point bounds, the LOS vectors between the RO and GPS satellites are plotted in blue at each time step, while the pierce points are plotted in pink as single points on the Earth's surface.

5.2.3   Occultation Metrics

From this single orbit simulation, statistics were gathered to characterize the typical occultation duration, type, and source constellation. These parameters are important for the design of an RO system, as the data rates and storage needs are based upon these parameters. For example, modulation differences exist between the GPS Block IIA/IIR and all later blocks. The IIA and IIR satellites broadcast only military signals on the L2 frequency, while the IIR-M and IIF satellites provide the civil signal L2C on the same frequency. Therefore, the GPS Block IIA and IIR satellites will only require a fraction of the hardware space during data collection that their later counterparts will require. Dual-frequency measurements, however, will not be possible with these same satellites.

A breakdown of the total occultation time by constellation and satellite block type is given in Figure 5.7. Because the simulation was performed with the current constellations as of 1-Jan-2015,
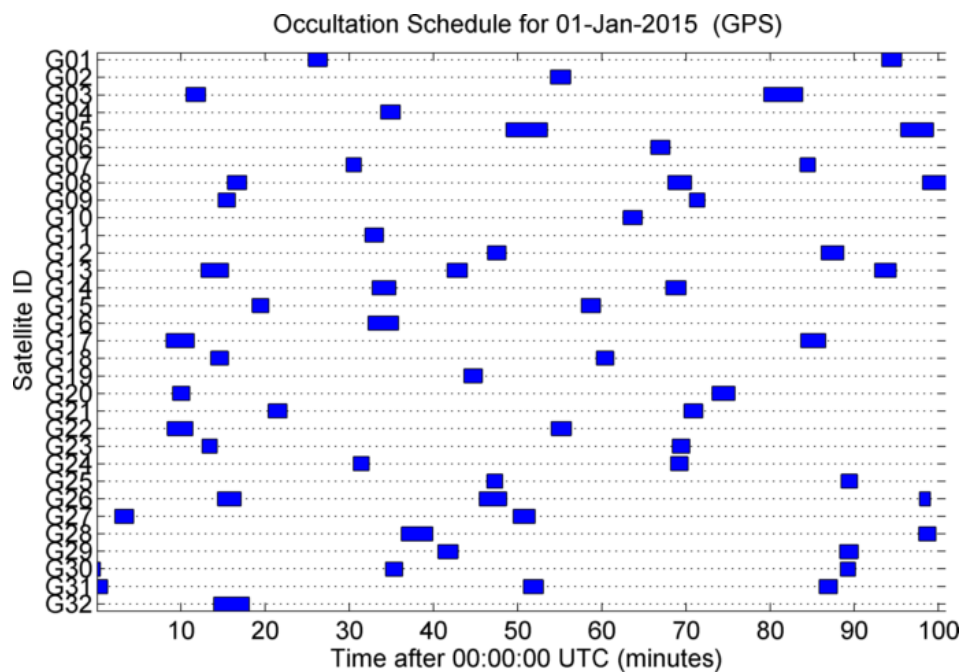
Figure 5.2: Timeline of geometric occultation events between a potential RO satellite and the GPS constellation on 1-Jan-2015 for the period of one LEO orbit.
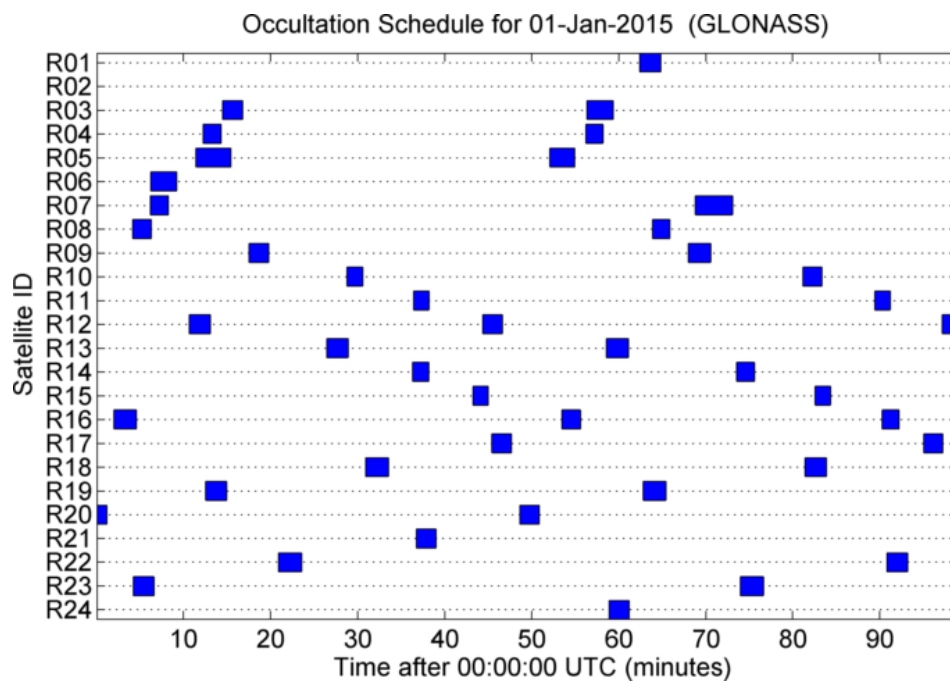
Figure 5.3: Timeline of geometric occultation events between a potential RO satellite and the GLONASS constellation on 1-Jan-2015 for the period of one LEO orbit.
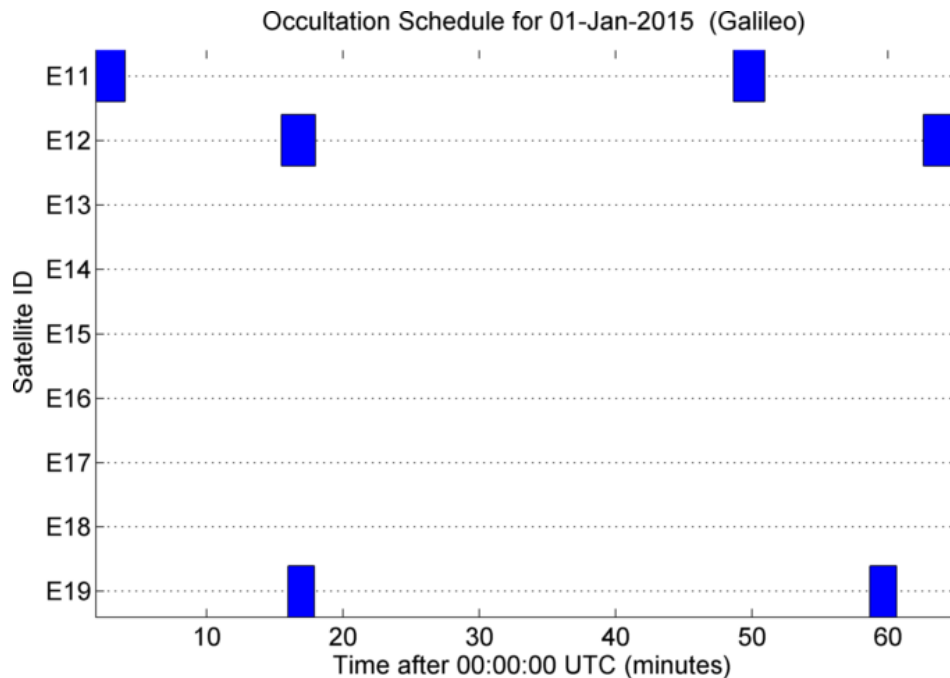
Figure 5.4: Timeline of geometric occultation events between a potential RO satellite and the Galileo constellation on 1-Jan-2015 for the period of one LEO orbit.
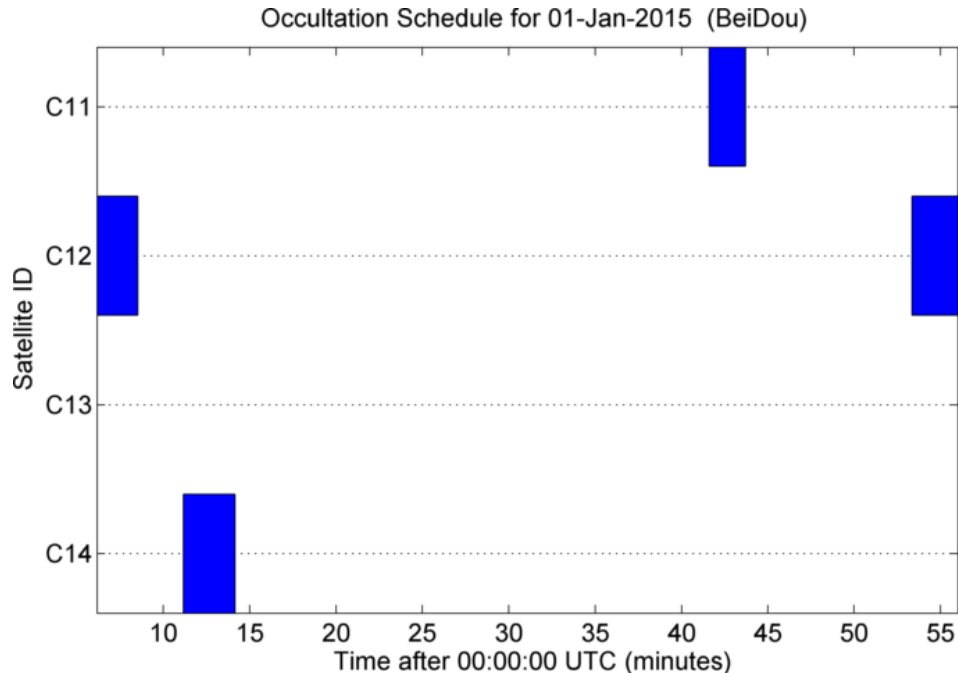
Figure 5.5: Timeline of geometric occultation events between a potential RO satellite and the BeiDou MEOs on 1-Jan-2015 for the period of one LEO orbit.
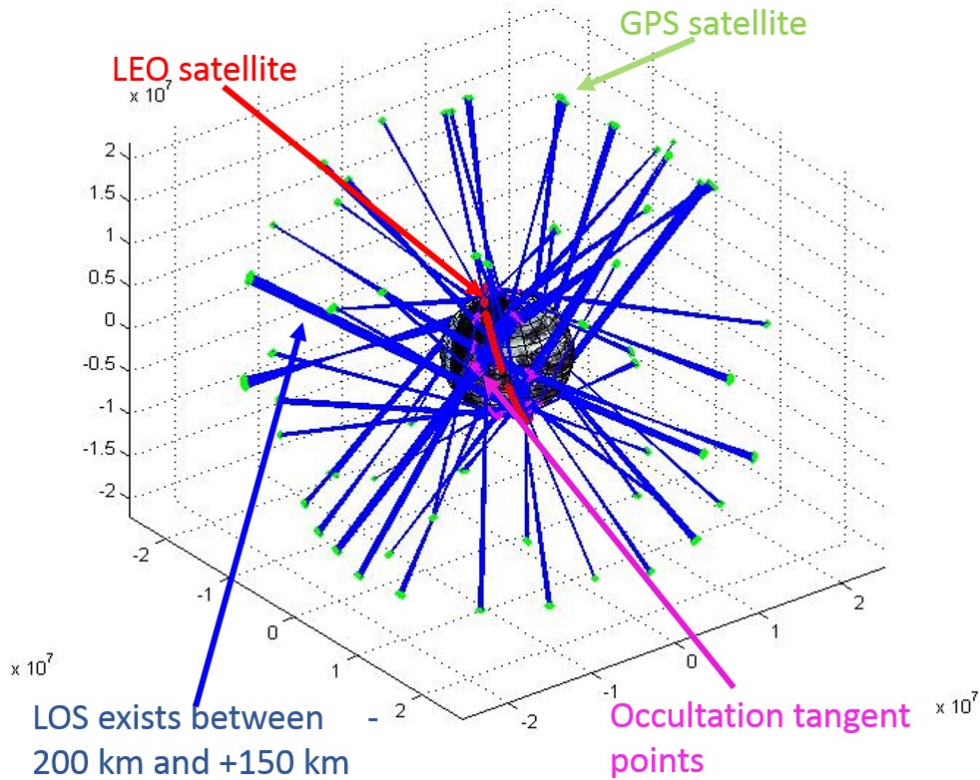
Figure 5.6: Simulation results from a single orbit of a possible occultation satellite at 800 km altitude. The LOS occultation events are shown in blue between the LEO satellite, plotted in red, to the GPS satellites, plotted in green. The occultation pierce points are shown in pink, and exist between +200 km and -150 km from the Earth's surface.

the majority of the geometric occultation opportunities are provided by the GPS constellation. The GLONASS satellites provide a large portion of the total occultation time, while the BeiDou and Galileo make up approximately $1/10^{th}$ of the total occultation time. The Galileo/BeiDou fraction will grow with the expected growth and launch schedule of both constellations. By 2020, Galileo and BeiDou collections will make up approximately 26% and 27% of the total occultation time, respectively. Another pie chart is shown in Figure 5.8 that describes the break down, in total time, of the rising and setting occultation opportunities. As expected, these are approximately equal.

The total occultation time for one orbit of the RO satellite can be broken down to time and fraction of the orbit spent in occultation, and is shown in Table 5.1. As apparent by these times
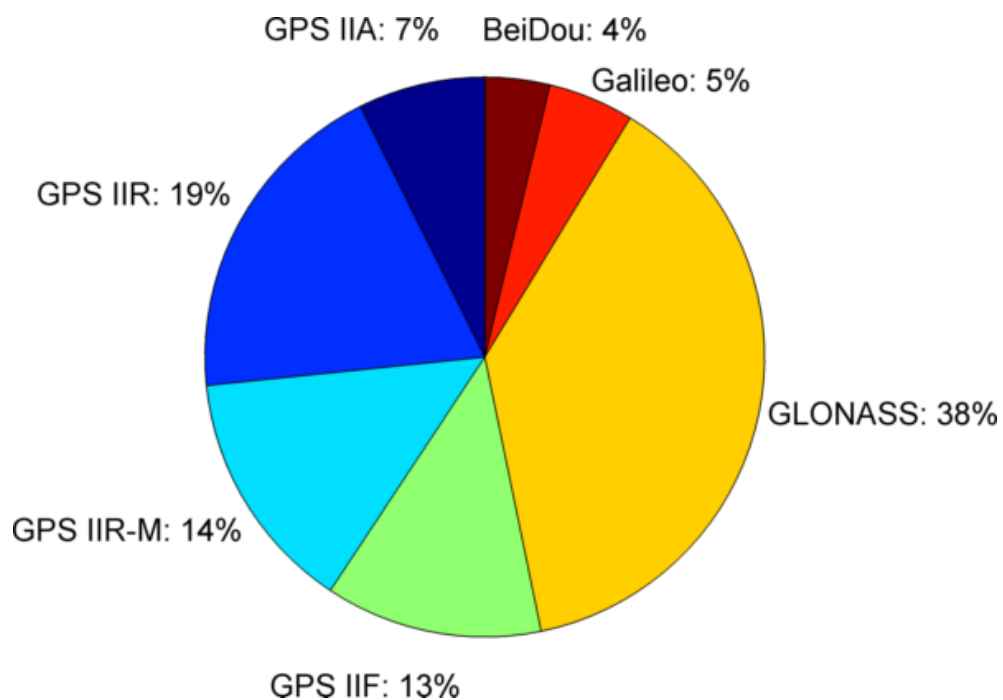
Figure 5.7: Pie chart describing the occultation source break down from the GNSS constellations as of 1-Jan-2015. The GPS constellation makes up 54% of the total occultation time.
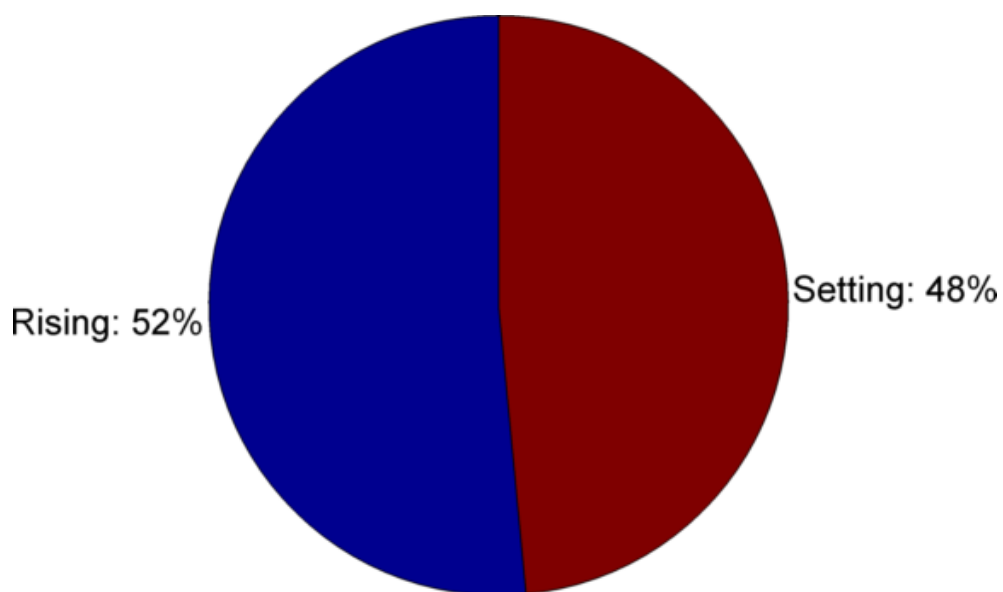
Figure 5.8: Pie chart describing the break down between total rising and setting occultation times.

and by the timelines, there is overlap between the occultation events. Some of the coinciding occultations can be collected simultaneously, however, some constellations must be collected separately due to frequency differences. Therefore, a collection priority list, based upon signal stability results described in the upcoming Chapter 7, is given in Table 5.2.

Table 5.1: Total time spent in occultation for the simulation of one orbit of the RO satellite. Time is shown in both seconds and fraction of the orbit for each of the GPS blocks and other GNSS constellations.

	Block IIA	Block IIR	Block IIR-M	Block IIF	GLONASS	Galileo	BeiDou
Occ. Time (s)	1067	2250	1834	1954	4114	686	605
Occ. Frac	0.1763	0.3717	0.3030	0.3228	0.6797	0.1133	0.1000

Table 5.2: Occultation collection priority list based upon the short-term stability of the occultation source signal.

Priority	Const/Block	Clock
1	Galileo	PHM
2	GPS Block IIF	RFS
	Galileo	RFS
	BeiDou	RFS
3	GPS Block IIA	RFS
	GPS Block IIA	CFS
	GPS Block IIR	RFS
	GPS Block IIR-M	RFS
4	GPS Block IIF	CFS
5	GLONASS	CFS

A histogram portraying the distribution of the simulation occultation duration is shown in Figure 5.9. The majority of occultation durations fell between 100 and 175 seconds, restricted by the field of view constraint, primarily. The outliers at the lower end of distribution are associated with occultation events that were cut short due to limited simulation time. A few larger outliers existed that were longer than the typical occultation event, and were likely due to the GNSS satellite being at a low elevation angle at the widest field of view. A tighter restriction of the field

of view removes the large outliers, as shown in Table 5.3, where the smaller field of view reduces the maximum occultation duration and standard deviation of the distribution.
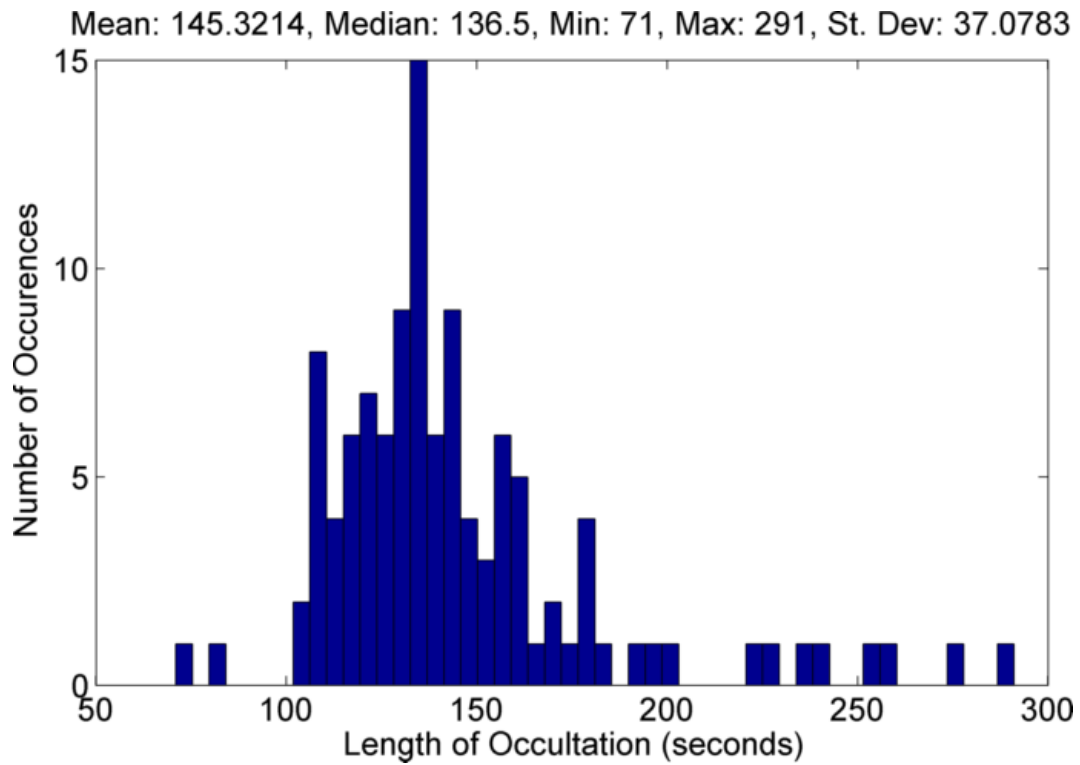
Figure 5.9: Histogram of occultation event duration times for a single orbit simulation. Duration statistics are shown in the title for this distribution (in units of seconds).

Table 5.3: Statistics of a typical occultation event duration for a given field of view angle bound. Note the field of view bound shown is the angle from bore sight (the total field of view angle is twice this amount).

Statistic	Field of view from bore sight		
	45°	50°	55°
Mean (sec)	135.4	141.2	145.3
Median (sec)	135	135.5	136.5
Minimum (sec)	71	71	71
Maximum (sec)	229	276	291
Std. Dev (sec)	22.8	32.2	37

5.3   Scheduler Summary

The occultation scheduling algorithm developed here predicts the upcoming occultation collection opportunities by LOS calculations between the LEO and GNSS satellites. Accurate orbital estimates of the position and velocity of the LEO occultation satellite are an integral piece to the validity of the predicted occultation event times and durations, and an OD engine with sufficient accuracy for Doppler estimation within 10 Hz must be implemented. The propagation of the GNSS satellites is autonomously calculated from the ephemerides of the broadcast navigation messages. For mission planning and data collection planning purpose, duration statistics were produced for one orbit of an example RO satellite in LEO. These statistics are automatically generated for the simulation and should be useful in the determination of data storage space and processing needs for future occultation mission planning.

Chapter 6

GNSS SATELLITE CLOCK CHARACTERIZATION

The GNSS signals are well suited for precision carrier phase applications, like RO, as each satellite is equipped with a highly stable atomic frequency standard (AFS), necessary for all navigation functionality. The frequency stability of the signals emitted by the GNSS satellites is tied to the stability of the AFS they carry onboard, and is thus critical to the quality of the carrier phase measurements. Because the atomic clocks onboard the GNSS satellites are generally optimized for stability performance at longer time scales (hours/days), there exists a range of clock stabilities at timescales relevant to a space-based RO event (< 100 seconds). The short-term stability hinges upon both the performance of the crystal oscillator in the control loop and the stability of the AFS itself.

Satellite clock instabilities cause variations in the carrier phase that will degrade the atmospheric profiling via RO if not properly characterized. A clock sampling interval of 1 second or less is required for single and undifferenced processing to achieve the highest quality excess atmospheric phase data for RO applications [73]. Because a typical space-based RO event lasts approximately 100 seconds, knowledge of clock stability over time intervals of 0.1-100 seconds is significant [57]. It is important to understand the behavior of GNSS satellite clocks as it influences future RO receiver and satellite designs, as well as required ground infrastructure and post-processing methodologies.

The terminology and methodology used to conduct an analysis of the GNSS satellite clock performance at timescales relevant to RO collections is presented in this chapter. The satellite clock contribution to the carrier phase of the signal is isolated through minimization and elimination of

other error sources. The Allan deviation (AD), which is a statistic used to characterize clock stability, is discussed, along with variations to the AD method that better assess the oscillators at time intervals pertinent to RO. Two independent methodologies are developed here to account for the errors introduced by the receiver clock to the carrier phase observations from which the clock performance is derived. Finally, possible methods to compensate for the thermal noise contribution to the variation of the carrier phase are addressed in heuristic and analytic approaches.

6.1   Carrier Phase Development

The satellite clock variation is measured through precise measurement and modeling of the carrier phase of the GNSS signal. The model for GNSS carrier phase measurements from a particular satellite, A, is the following.

$$\phi_A \lambda_A = \rho_r^A - c\delta t^A + c\delta t_r + \rho_{trop}^A - \rho_{iono}^A + \rho_{mult}^A + N_A \lambda_A + \epsilon_\phi^A \tag{6.1}$$

where the definitions in Table 6.1 hold.

Table 6.1: Definitions of terms within the GNSS carrier phase model.

ϕ_A	Carrier phase measurement
λ_A	Wavelength associated with carrier frequency
ρ_r^A	Geometric distance between receiver and satellite
c	Speed of light
δt_r	Receiver clock error
δt^A	Satellite clock error
ρ_{trop}^A	Range error attributed to the troposphere
ρ_{iono}^A	Frequency-dependent error due to the ionosphere
ρ_{mult}^A	Frequency-dependent range error due to multipath
N_A	Carrier phase ambiguity integer
ϵ_ϕ^A	Thermal noise error term

To isolate the satellite clock value, δt^A, from Equation 6.1, the other terms must be sufficiently modeled and/or minimized with appropriate assumptions and data collection techniques. Typically, the largest error source in the carrier phase equation is the receiver clock term, δt_r. In positioning applications, the receiver clock bias and drift are solved for in the least squares solution, allowing

for inexpensive clocks to be used in ordinary GNSS receivers. Here, the variations in the carrier phase due to the satellite clock are the measurement of interest, and therefore the receiver clock cannot be solved for or eliminated by a batch solution.

Two common techniques have evolved to compensate for the receiver clock error: 1) single differencing the carrier phase data from two satellites collected by a common receiver, or 2) using a very precise receiver reference. Single differencing allows for the noise contribution from the imprecise receiver clock to be removed by subtraction between two signals, as it is common to both satellites. What remains is a combination of carrier phases from both satellites, which may or may not be desired. The use of precision atomic clocks, on the other hand, is conceptually easier because the effect of the receiver clock is minimized and bounded. In the following studies, active hydrogen masers (AHM) are often used as the receiver oscillator. Although the receiver clock error term is not removed from Equation 6.1, it is typically an order of magnitude or greater lower than the remaining error terms. Further discussion of the receiver clock mitigation techniques is discussed in Section 6.3.

The geometric distance term, ρ_r^A, in Equation 6.1 is modeled and removed using precision orbit files produced by the IGS and the receiver position, which was found using a geodetic GNSS receiver (in the experiments that follow, a Trimble NetR9 receiver). Orbit positions are reported at fifteen-minute intervals for the GPS, GLONASS, and Galileo constellations by the IGS. Precision orbits are not yet available for BeiDou; therefore, the lower quality broadcast ephemeris is used instead. Interpolation between data points of the IGS orbit values is necessary to report positions at the rate of the raw carrier phase data. A 9th-order trigonometric interpolation algorithm as given by Schenewerk (2003) provides satellite positions at the necessary rate. This trigonometric interpolation scheme, shown in Equation 6.2, outperforms polynomial expansions, as it better represents the physical characteristics of the orbit over short time spans [72].

$$C = A_0 + A_1 \sin(\omega t) + A_2 \cos(\omega t) + A_3 \sin(2\omega t) + A_4 \cos(2\omega t) + ... + A_9 \cos(9\omega t/2) \qquad (6.2)$$

C represents the x, y, or z coordinate value, t is the time, and A_0 through A_9 are the coefficients

of the polynomial that are adjusted to fit the ephemeris data. The characteristic frequency is represented by ω, which is proportional to the ratio of the solar day to the satellite's orbital period. The characteristic frequencies are unique to the respective constellations; GPS satellites orbit the Earth twice per sidereal day, while the other constellations are slightly more or less than this value.

The unknowns that remain in Equation 6.1 are the satellite clock error, atmospheric influences to the signal, multipath, and the carrier phase ambiguity. Because the interest in this study is the incremental change in carrier phase, the integer ambiguity term cancels out as it is constant, unless a cycle slip occurs. During the data collections described in the next chapter, antenna choice and placement were important factors to manage and minimize the errors induced by multipath. Additionally, data arcs from overhead satellites were used to decrease the possibility of reflected signal paths. Under quiet atmospheric conditions, tropospheric errors are slow varying [36]. Therefore, over the short timescales of the carrier phase analysis, the troposphere was assumed to be constant and having no effect on the stability calculations.

Dual-frequency measurements were considered as a method to remove the ionospheric contribution in Equation 6.1, however Hauschild et al. (2013) shows a direct comparison of the one way carrier phase (1WCP) methodology for single- and dual-frequency measurements. In their results, the single frequency observations show better performance than the dual-frequency measurements for short time intervals as the two streams of data in dual-frequency results add a factor of $\sqrt{2}$ to the noise. For time scales of 200 seconds or longer the single frequency results are worse than the dual frequency results which is indicative of an ionospheric contribution to the single frequency results [36]. For the clock analysis performed in this thesis, the analysis period was sufficiently short (< 200 seconds) to assume the ionospheric delays to the signal were smaller than the clock contributions. As an additional tactic to minimize the impact of the ionosphere, carrier phase measurements were taken during local night time at which the ionospheric error contribution is minimal.

6.2   Statistic of Measuring Time Stability

6.2.1   Allan Deviation

The most common measure of the performance of frequency standards is the Allan variance. Also known as the two-sample variance, the Allan variance provides a statistical measure of clock behavior inherently dependent on the time period between samples, τ, and the distribution measured. The Allan deviation (AD) is defined as the square root of the Allan variance.

The average fractional frequency of the ith clock phase measurement, ϕ, over the interval τ is given by

$$\bar{y}_i^\tau = \frac{\phi(t_i + \tau) - \phi(t_i)}{\tau} \tag{6.3}$$

The Allan variance, in the time domain, is the infinite average of the difference between subsequent fractional frequency measurements, and is given by Allan et al. (1988) as

$$\sigma_y^2(\tau) = \frac{1}{2}\langle (\Delta \bar{y}^\tau)^2 \rangle = \frac{1}{2\tau^2}\langle (\phi(t_i + \tau) - 2\phi(t_i) + \phi(t_i - \tau))^2 \rangle \tag{6.4}$$

where $\Delta \bar{y}$ defines the difference between adjacent frequency measurements, and $\langle \rangle$ represents the expectation operation [2]. Using the overlapping estimate of the expected value, the Allan variance can be approximated for N time samples by

$$\sigma_y^2(\tau) \approx \frac{1}{2\tau^2(N-2)} \sum_{i=2}^{N-1} (\phi(t_i + \tau) - 2\phi(t_i) + \phi(t_i - \tau))^2 \tag{6.5}$$

The AD is a useful statistical tool for characterizing frequency stability and the limiting noise processes. For noise processes that dominate at very short time intervals (less than one second), the AD becomes ambiguous because it does not distinguish between white phase noise modulation and flicker phase noise modulation [1]. The modified Allan deviation (MAD) distinguishes between the signatures of these two noise processes by optimizing the detection bandwidth coinciding to the sample interval. The MAD modifies the reciprocal software bandwidth linearly with sample time, yielding a clear distinction between white and flicker phase noises. It is first defined in Allan and

Barnes (1981) as

$$\sigma_{y,\text{MOD}}^2(\tau) = \frac{1}{2\tau^2} \left\langle \left(\frac{1}{n} \sum_{i=1}^{n} (\phi(t_i + \tau) - 2\phi(t_i) + \phi(t_i - \tau)) \right)^2 \right\rangle \tag{6.6}$$

For finite data sets, the following approximation for the MAD is generally used [1].

$$\sigma_{y,\text{MOD}}^2(\tau) \approx \frac{1}{2\tau^2 n^2 (N - 3n + 1)} \sum_{j=1}^{N-3n+1} \left(\sum_{i=j}^{n+j-1} (\phi(t_i + \tau) - 2\phi(t_i) + \phi(t_i - \tau)) \right)^2 \tag{6.7}$$

The AD and MAD curves have a specific relationships with the power law noises that they represent and can be determined by the slope of the curve on a log-log sigma-tau plot. Table 6.2 gives the relationship between power law noise, power spectral density function, $S_y(f)$, and the AD and MAD characteristic slopes [69]. Figure 6.1 is courtesy of Riley (2008), and shows measures of the frequency stability (AD and MAD) versus time over which the frequency is averaged. The slopes seen in Figure 6.1 are identical to the values shown in the penultimate and last columns of Table 6.2.

Table 6.2: Relationship between the power law noises and their slopes on a sigma-tau plot, used frequently by AD and MAD analysis. Each noise type has a specific slope for the power spectral density function ($S_y(f)$), AD ($\sigma_y(\tau)$), and MAD ($\sigma_{y,\text{MOD}}(\tau)$).

Noise	$S_y(f)$	$\sigma_y(\tau)$	$\sigma_{y,\text{MOD}}(\tau)$
White phase modulation	f^2	τ^{-1}	$\tau^{-3/2}$
Flicker phase modulation	f^1	τ^{-1}	τ^{-1}
White frequency modulation	f^0	$\tau^{-1/2}$	$\tau^{-1/2}$
Flicker frequency modulation	f^{-1}	τ^0	τ^0
Random walk frequency modulation	f^{-2}	$\tau^{1/2}$	$\tau^{1/2}$

6.2.2 Pre-filtered Allan Deviation

Although fairly straight-forward to implement, the formulation shown in Equation 6.7 takes significantly longer computation time than the traditional AD for higher-sampled, multi-hour data arcs. A pre-filtered Allan deviation (PAD) was developed that averages consecutive phase samples prior to the calculation of the AD. In doing this, the software bandwidth is optimized according to sample time and is mathematically equivalent to Equation 6.7.
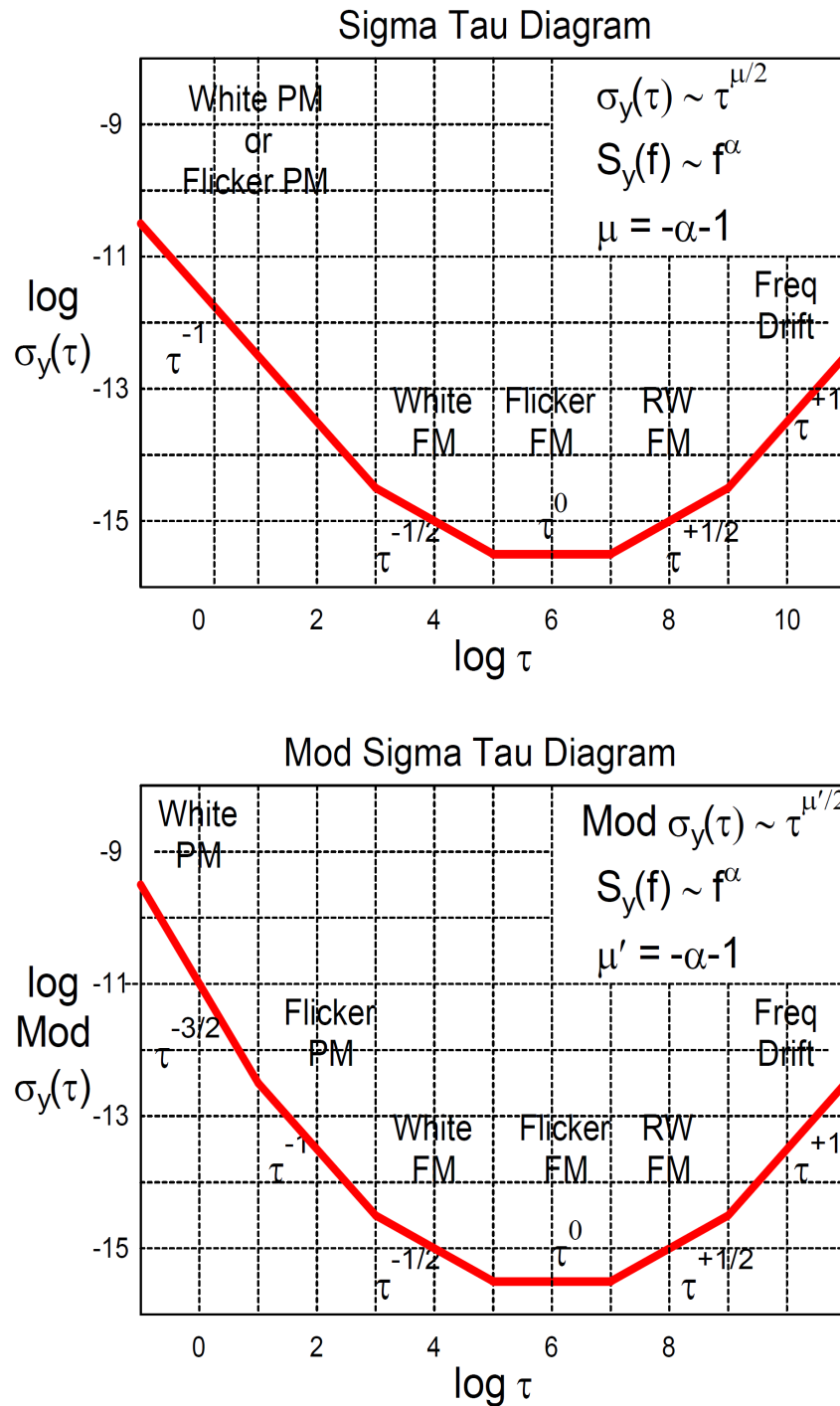
Figure 6.1: Sigma tau and modified sigma tau diagrams, showing the relationship between power law and slope of the AD or MAD. Images reproduced from Riley (2008) [69].

Equation 6.7 takes a considerable amount of time for long, high-rate data arcs due to the double summation operation. Returning to the original definition given in Allan and Barnes (1981), the MAD makes use of a software bandwidth, which is realized by averaging n adjacent phase measurements [1]. For the PAD, the MATLAB functionality to reshape and average adjacent samples is used until the minimum software bandwidth is reached, defined as $N = \tau \times bw$, where bw is the PLL bandwidth.

The PAD is an efficient coding implementation that provides the noise differentiating advantages of the MAD with the processing speed of a traditional AD. It reduces the short-term phase variations by essentially narrowing the filter bandwidth. Because the C/N_0 varies by a few dB-Hz between the GNSS satellites collected for this analysis, averaging serves to eliminate excess noise where C/N_0 is relevant. The optimum performance is achieved when the noise bandwidth is the inverse of the sampling interval. For example, using 20 Hz data, 40 clock phase points were averaged to calculate the $\tau = 2$ second PAD values.

The algorithm for the PAD is given here and shown visually as pseudocode in Figure 6.2. The carrier phase observations from the receiver are corrected with long-trend variation removal of the orbital contribution using precision orbits produced by the IGS. The remaining long-term variations due to ionosphere, troposphere, and unmodeled orbit errors are removed with polynomial detrending [36]. This leaves only the variation of the satellite clock with respect to some reference clock and the measurement error. The carrier phase observations are then sampled at a maximum rate to guarantee independent measurements, which is equal to the data rate over the bandwidth. N consecutive samples are then averaged, where N is the PLL bandwidth multiplied by the AD interval, τ. Because of the very large sample size, any remaining samples after the averaging operation are truncated. The AD, as described in Section 6.2.1, is then calculated with the averaged samples for all τ intervals.

The MATLAB implementation of the PAD developed as part of this work is available at MATLAB Central [31]. Since the PAD described here is equivalent to the MAD, the Allan analyses that follow are calculated as a PAD, but referred to as MAD for comparison to other similar studies.

For all τ

Initialize with detrended carrier phase measurements

Resample at $\frac{\text{time step}}{\text{bandwidth}}$

Average $N = \tau \cdot$ bandwidth and truncate

Calculate Allan deviation at τ with new points

$$\sigma_y^2(\tau) \approx \frac{1}{2\tau^2} \sum_{i=2}^{N-1} \big(\phi(t_i + \tau) - 2\phi(t_i) + \phi(t_i - \tau)\big)^2$$
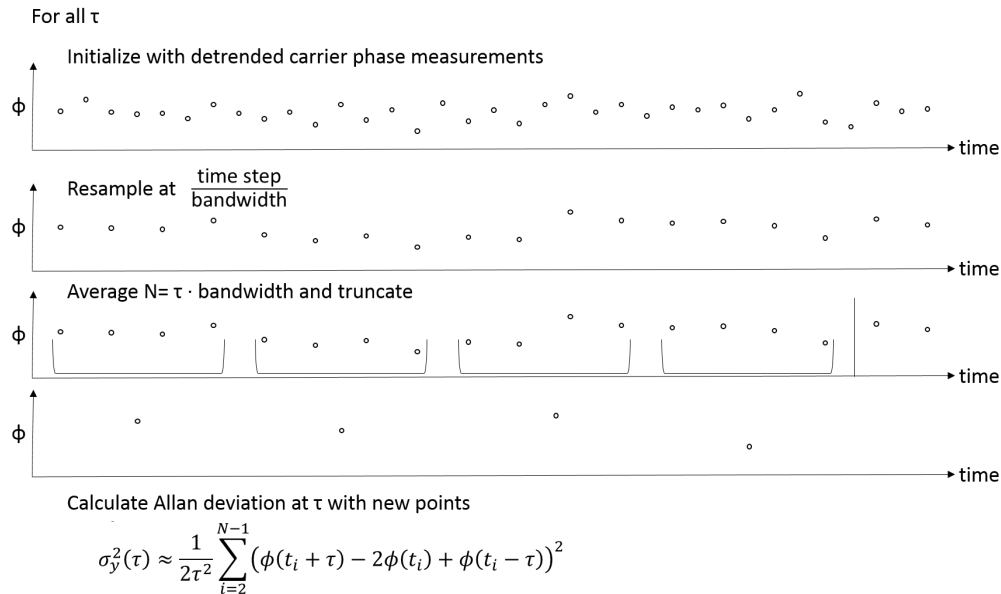
Figure 6.2: Generic algorithm describing the pre-filtering process for the carrier phase measurements prior to taking the AD. The phase measurements are first detrended, resampled, and then averaged prior to computing the AD.

6.3 Receiver Clock Error Compensation

Two methods were explored to remove the carrier phase errors introduced by the receiver clock. The first, referred to as the three cornered hat (3CH) method, uses single differenced carrier phase measurements from two satellites to remove the common receiver clock error. This approach requires a receiver reference with sufficient stability to maintain lock when tracking the signal. The second method, which is referenced as the one way carrier phase (1WCP), requires a reference at the receiver with better accuracy than the clock of interest from the GNSS satellites [28, 18, 36]. In this approach, the receiver clock error is minimized during the data collection.

6.3.1 Differencing Method

Single differencing carrier phase measurements from two satellites is a prevalent technique used to remove the errors induced by the receiver clock. The remainder is the clock phase between a pair of satellites with minimal noise contribution from the receiver clock. Although it may be

insightful to characterize the relative behavior between two satellite clocks, individual AFS behavior is desired for most applications. The variance of a single oscillator can be estimated by comparison with data from two or more other oscillators. The triangulation, or three-cornered hat, method requires independent oscillators and offers and unbiased result for the third oscillator because the expected value of the cross-correlation term approaches zero as the number of measurements increases [30]. Here, a version of the 3CH methodology is used that isolates individual satellite clocks and resolves the receiver clock noise by substituting single-differenced pairs of carrier phase measurements.

As described in Section 6.2.1, the difference of consecutive average fractional frequency measurements over the observation time τ for oscillator A at a given time, t_i is defined as

$$\epsilon_A(t_i) = \frac{\phi_A(t_i + \tau) - 2\phi_A(t_i) + \phi_A(t_i - \tau)}{\tau} \tag{6.8}$$

The application of the triangulation method using single difference pairs with clocks B and C is given by

$$\frac{1}{2(N-2)} \frac{1}{\tau^2} \sum_{i=2}^{N-2} (\epsilon_A(t_i) - \epsilon_B(t_i)) \cdot (\epsilon_A(t_i) - \epsilon_C(t_i)) = \tag{6.9}$$

$$\frac{1}{2(N-2)\tau^2} \left(\sum_{i=2}^{N-2} \epsilon_A^2(t_i) - \sum_{i=2}^{N-2} \epsilon_A(t_i)\epsilon_C(t_i) - \sum_{i=2}^{N-2} \epsilon_B(t_i)\epsilon_A(t_i) + \sum_{i=2}^{N-2} \epsilon_C(t_i)\epsilon_B(t_i) \right) \tag{6.10}$$

$$\approx \frac{1}{2(N-2)\tau^2} \sum_{i=2}^{N-2} \epsilon_A^2(t_i) = \sigma_{y,A}^2 \tag{6.11}$$

As the cross-correlation terms between the different satellite clocks approach zero with increasing number of observations, the squared error term from the satellite of interest remains. This is approximately equivalent to the Allan variance of the clock phase error from satellite A, to within the error of the accumulated cross-correlation terms.

The number of measurements, N, that is sufficient for the cross-multiplied terms to be significantly less than the squared term can be estimated as follows. The standard deviation of a single element in the cross-term summation of Equation 6.9 is

$$\langle (\epsilon_A \epsilon_B)^2 \rangle^{1/2} = \langle (\epsilon_A^2 \epsilon_B^2) \rangle^{1/2} = \langle \epsilon_A^2 \rangle^{1/2} \langle \epsilon_B^2 \rangle^{1/2} = \sigma_{y,A}\sigma_{y,B} \tag{6.12}$$

The second equality is valid because the values ϵ_A and ϵ_B from the clocks on two different satellites A and B are assumed independent and zero mean. The standard deviation of each of the three cross-term summations will approximately equal the product of the individual standard deviations divided by N. If the desired fractional uncertainty in the estimate of $\sigma_{y,A}^2$ is denoted as m, then

$$\frac{\sigma_{y,A}\sigma_{y,B} + \sigma_{y,A}\sigma_{y,C} + \sigma_{y,B}\sigma_{y,C}}{N} = m\sigma_{y,A}^2 \tag{6.13}$$

Solving for N yields

$$N = \frac{\sigma_{y,A}\sigma_{y,B} + \sigma_{y,A}\sigma_{y,C} + \sigma_{y,B}\sigma_{y,C}}{m\sigma_{y,A}^2} \tag{6.14}$$

If the three frequency standards have comparable stability, such that $\sigma_{y,A} \sim \sigma_{y,B} \sim \sigma_{y,C}$, then $N = 3/m$. If an uncertainty of 10% ($m = 0.1$) in the $\sigma_{y,A}^2$ estimate is desired, then $N = 30$; at least thirty measurements of the carrier phase from each satellite would be necessary to determine the variance of a single satellite clock. If one of the three frequency standards was a factor of 10 worse than the other two, such that $\sigma_{y,A} \sim \sigma_{y,B} \sim 0.1\sigma_{y,C}$, then $N = 21/m$. To achieve 10% uncertainty in the $\sigma_{y,A}^2$ estimate, 210 measurements would be required.

This 3CH methodology does not require an AFS for the receiver. In fact, the receiver clock needs only enough precision to maintain a tight phase lock on all signals, as single differencing removes the error introduced by the common receiver clock. Multiplying pairs of single differences allows for AD analysis of a single satellite clock, and in turn, its stability characteristics can be determined given comparable clock stabilities and enough measurements. The overall data arc length, data volume considerations, and the variation in orbit and atmospheric errors limit the applicability of this methodology to time intervals of approximately 1,000-1,500 seconds.

6.3.2   Active Hydrogen Masers

The 3CH method has its limitations, however, as a single satellite with clock stability that differs from the other two in the trio will limit the accuracy of the AD results without sufficiently long data arcs. Additional averaging of the data would be necessary if stabilities of the clocks in the trio of satellites were grossly different. For example, if one of the three frequency standards was

a factor of ten better than the other two, as with the Block IIF rubidium clocks compared to the older GPS blocks, then to achieve 10% uncertainty in the σ_y^2 estimate would require 1,200 averages. The estimate of the AD at a timescale of 100 seconds would require 120,000 seconds, or almost 1.5 days, of continuous data collection. A better option is to simultaneously acquire data from three GNSS satellites with clocks of comparable stability. To estimate the performance of a Block IIF satellite clock would require some combination of three Block IIF satellites and/or Galileo satellites in the sky at the same time.

An alternative approach is the use of a precise receiver reference that has significantly better stability at the time scales of interest than the GNSS frequency standards being characterized. This eliminates the need for the 3CH processing methodology and allows for characterization of the newer GNSS constellations, such as the Passive Hydrogen Masers (PHM) on the Galileo satellites, or the newly developed rubidium frequency standards (RFS) on the GPS Block IIF satellites. The 1WCP method, used in [36, 28, 18], allows for the extraction of the temporal behavior of the GNSS clock from the carrier phase of a single receiver, only under quiet atmospheric conditions and with a sufficiently good receiver clock.

A comparison of the MAD results as calculated by the 3CH and 1WCP with precise reference are shown in Figures 6.3 and 6.4, respectively. The 1WCP results in Figure 6.4 show lower MAD results for PRN 25 (SVN 62), a Block IIF satellite, for averaging intervals of $\tau \geq 5$ seconds. Because the relative stabilities between the GPS Block IIF RFS and the other satellite AFS differ by such a large margin, the 3CH method over estimates the MAD for PRN 25, as seen in Figure 6.3. The MAD curves of the other satellite AFS shown in Figures 6.3 and 6.4 are very similar, indicating good agreement between the techniques for oscillators with comparable stabilities. To accurately characterize the AFS from all GNSS constellations, either trios of clocks with similar stability characteristics would need to be found (which can be difficult given their orbital geometries and sky pass frequencies), or the 3CH methodology cannot be used.
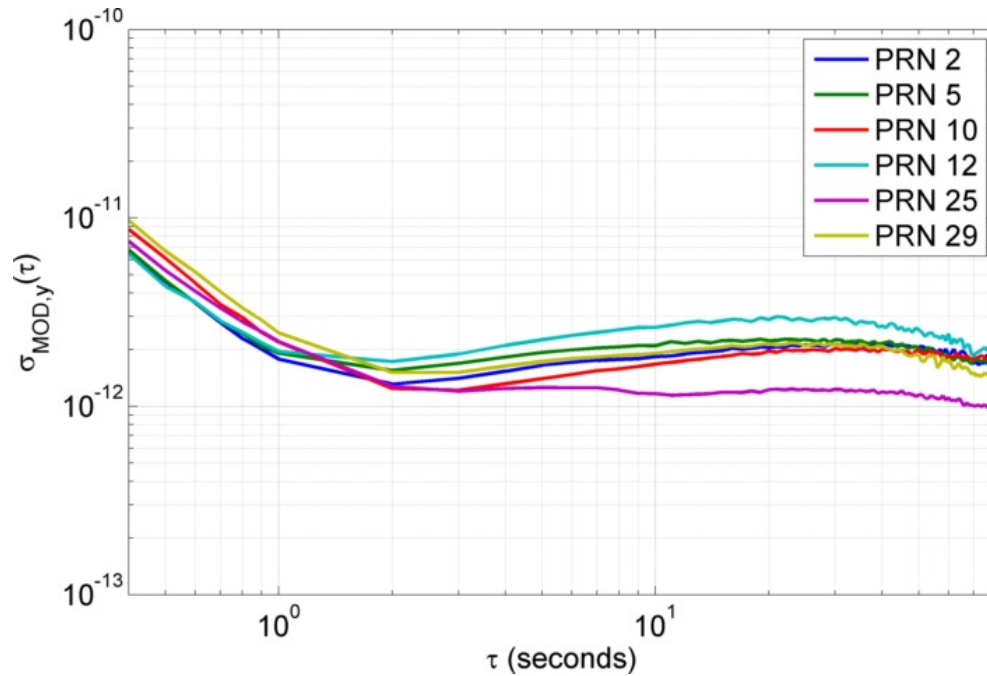
Figure 6.3: Individual GPS satellite MAD from $0.4 \leq \tau \leq 80$ seconds, as produced by the 3CH method with satellite clocks of varying stability.
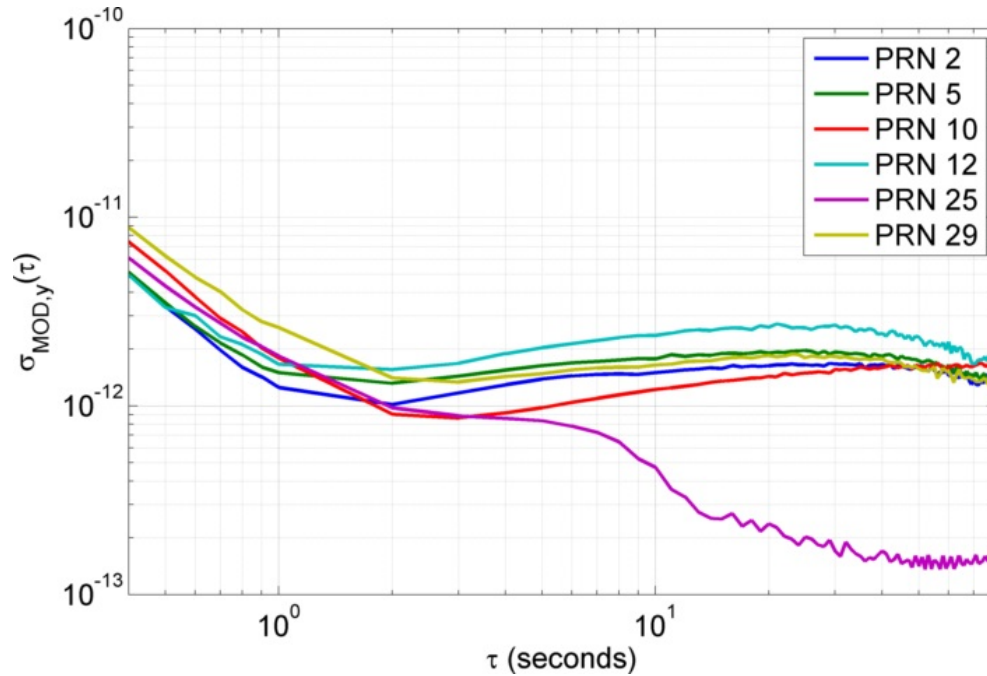
Figure 6.4: Individual GPS satellite MAD from $0.4 \leq \tau \leq 80$ seconds using the 1WCP methodology with AHM as the receiver clock.

6.4 Thermal Noise Compensation

The thermal noise of the receiver contributes to the variations in the measured clock phase and, in fact, dominates for sufficiently short time intervals. The thermal noise is distributed as zero-mean Gaussian in phase, and follows a white phase noise modulation on the sigma-tau plots shown in Figure 6.1. At short enough timescales, the GNSS signal noise due to tracking error in the PLL is primarily the result of thermal and oscillator error [46]. Therefore, the AD of the satellite clock can be analyzed in greater detail at shorter time intervals, and especially over the short-term transitional periods, if the thermal noise is removed.

Two approaches are discussed to model the white phase modulation due to the thermal noise contribution: 1) using the data to predict the amplitude of the white phase noise slope on a log-log plot, and 2) theoretically deriving the relationship between the signal C/N_0 and MAD values. The thermal noise contribution for two receivers are analyzed here: 1) a SDR developed by the CU, and 2) the Trimble NetR9 commercial off-the-shelf (COTS) receiver. As the hardware and processing software differ for these two systems, the thermal noise contribution to the MAD will not be the same. The underlying satellite clock performance, however, should be similar.

6.4.1 Heuristic Approach

The goal of eliminating the thermal noise contribution is to isolate the clock contribution to the MAD at the shortest time intervals possible. When using the software receiver, the PLL bandwidth can be decreased, which results in decreased noise and a lower reported MAD at time scales where the thermal noise is an important contributor to the measured noise. However, as the bandwidth is reduced, there exists a bandwidth threshold below which the software receiver loses lock on tracking the signal. The inherent stability of the receiver clock and relative satellite dynamics are essential in determining the lower limit on the bandwidth; an atomic reference could allow tracking at a lower bandwidth. Experimentally, it was found that PLL bandwidths less than 20 Hz caused tracking issues for these particular data sets with the software receiver.

At longer timescales, the MAD of a GNSS cesium frequency standard (CFS) or RFS typically behaves as white frequency modulation because these are frequency locked devices, whose characteristic slope of a log-log scale is $\tau^{-1/2}$. The expected slope of the averaged measurements, when dominated by the receiver thermal noise at shorter time intervals is $\tau^{-3/2}$, as seen in Figure 6.5 for $\tau \leq 0.4$ seconds [69]. To isolate and remove the contribution of the white phase noise to the measured MAD, the coefficients of the linear fit (in log-log space) were determined using the data points for the first four values of $\tau = 0.05, 0.1, 0.15,$ and 0.2 seconds. The uncertainty of the MAD estimates at these shorter time intervals is small because of their large number of phase observations over the entire data acquisition period.
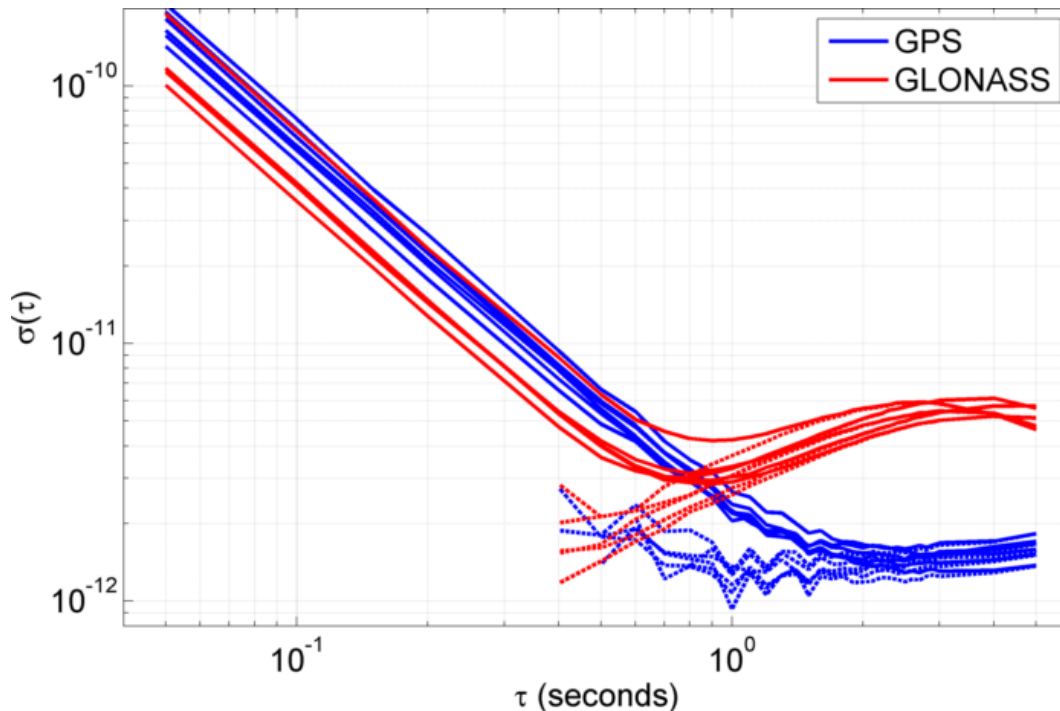
Figure 6.5: Short-term MAD values for satellites in the GPS and GLONASS constellations before and after thermal noise removal. The dashed values are the MAD after subtraction of the linear model of the white phase noise. Better isolation of the satellite clock contribution is shown over the transition period between the white phase and white frequency modulation slopes.

Under the assumption that thermal noise and satellite clock noise are the only contributors to the measured variance at these timescales, the thermal noise can be removed statistically using

the linear model (in log-log space) to extrapolate the white phase noise contribution to longer time intervals, leaving only the satellite AFS contribution. Figure 6.5 illustrates the results when the thermal noise contribution to the MAD is removed with a $\tau^{-3/2}$ model of the white phase noise. The smooth, straight line behavior shown for all satellites for $\tau \leq 0.4$ seconds is an artifact of the data collection and sampling hardware and is removed to reveal the underlying performance of the satellite clock.

To ensure that the clock noise estimate was really from the clock, time scales are reported only if the residual between the total measured MAD and the white phase noise fitted lines was at least three times larger than the RMS uncertainty in the white phase noise contributions. The dashed values shown in Figure 6.5 are the MAD with thermal noise variance removed. Note that not all GPS satellites have MAD values at $\tau = 0.4$ and 0.5 seconds because of the 3σ quality check.

6.4.2   Analytic Approach

An analytic approach was developed to relate the MAD behavior at sub-second time intervals to the C/N_0 of the signal. From the formulas presented in Riley (2008), the MAD can be related to the phase noise power spectral density function, $S_\phi(f)$, as follows [69]:

$$\sigma_{MOD,y}(\tau) = \frac{\sqrt{3 f_h S_\phi(f)}}{2\pi\tau\nu_0\sqrt{n}} \tag{6.15}$$

where f_h is the upper cutoff frequency of the measurement system (PLL bandwidth), τ is the MAD averaging interval, n is the number of averaged samples (optimally set to $\tau \times f_h$), and ν_0 is the signal carrier frequency. Further simplification leads to the following relationship:

$$\sigma_{MOD,y}(\tau) = \frac{\sqrt{3}}{2\pi\tau^{3/2}\nu_0} SNR_0^{-1/2} \tag{6.16}$$

where the $SNR_0 = C/N_0/f_h$.

An example of the estimated white phase noise contribution derived from the C/N_0 of the signal is shown for four satellites collected with the Trimble NetR9 in Figure 6.6. Because the C/N_0 varies over the course of the 3-hour long arc for a single satellite, the calculated thermal noise MAD

values are shown as a range. As expected, the MAD from the measured clock phase values falls within the range of thermal noise MAD for shorter averaging intervals, where the signal variation is dominated by white phase modulation. The contribution of noise from the satellite AFS causes the measured MAD to rise above the white phase noise at longer averaging intervals.
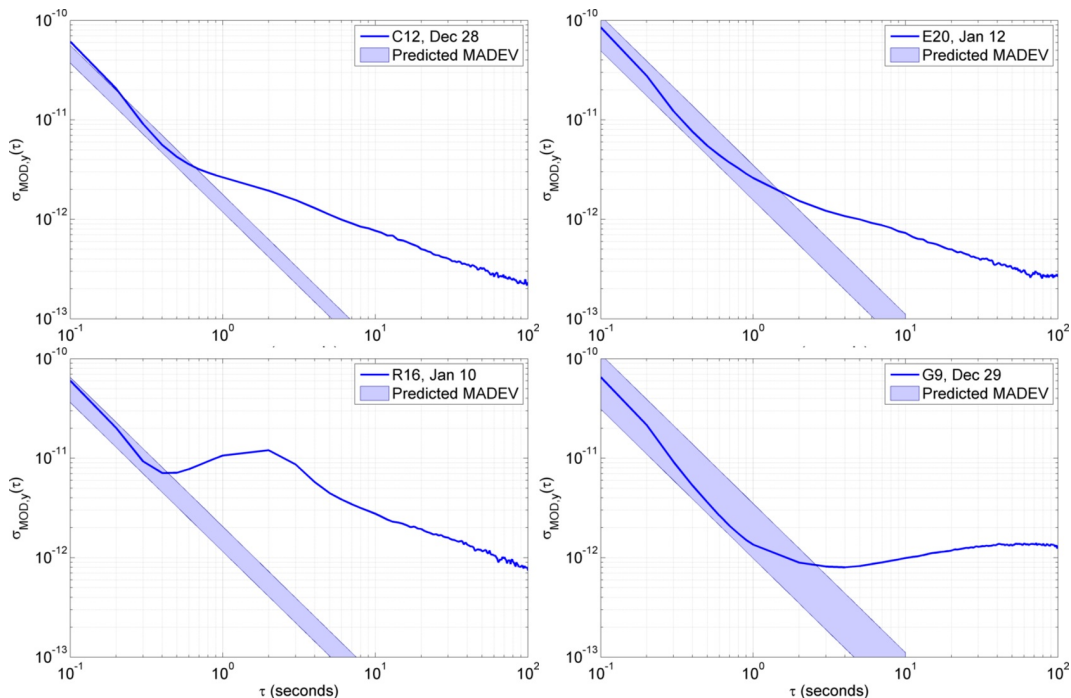
Figure 6.6: Theoretical vs. observed MAD based upon the range of C/N_0 measured for the received signal of example satellites in each GNSS constellation. The measured MAD results are obtained with the Trimble receiver which causes the curvature to the MAD at time scales less than about 0.6 seconds. Top left: BeiDou C12 (46-49.5 dB-Hz), top right: Galileo E20 (40-47 dB-Hz), bottom left: GLONASS R16 (45-49.5 dB-Hz), bottom right: GPS G09 (40-51 dB-Hz).

The plots in Figure 6.6 exhibit a distorted white phase noise response for sub-second τ, indicating some unknown filtering or loop adjustment is being made in the COTS receiver. Although the NetR9 reported observations at 50 Hz, a power spectral density of the clock phase observations from GPS PRN 2, shown in Figure 6.7, indicates independent measurements at approximately 1 Hz. At frequencies greater than 1 Hz, the power density exhibits a bump instead of the expected flat slope, typical of white phase noise. The NetR9 appears to apply unknown internal filtering at sub-second timescales, thus the short term white phase noise signature is distorted due to the filter

response in the receiver.

Without better knowledge of the internal processing functionality of the COTS receiver, the sub-second MAD results obtained with the commercial receiver must be discarded. In addition, the estimated white phase noise contribution cannot be removed in the manner described in Section 6.4.1, because of the non-white phase noise slope of the sub-second MAD results. Therefore, the Trimble NetR9 MAD analysis is limited to $1 \leq \tau \leq 200$ seconds, as the COTS receiver performance is best understood at these averaging intervals. Linear estimation and detrending of the white phase noise is only possible with the software receiver.
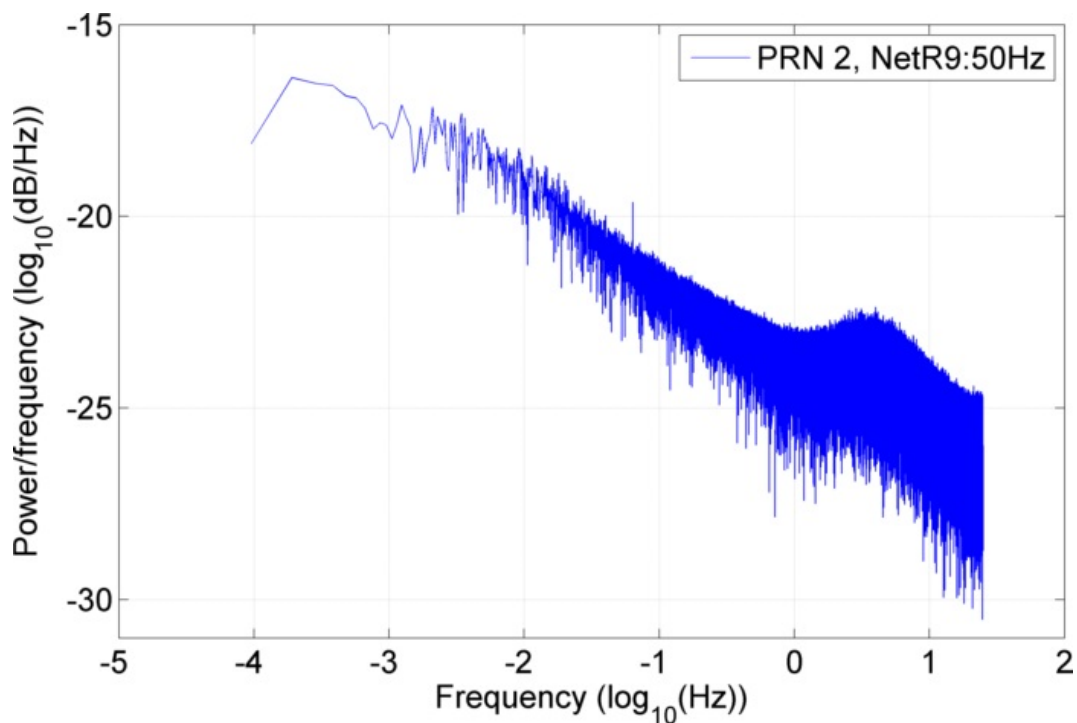
Figure 6.7: Example power spectral density plot (on a log-log scale) for the clock phase data produced by the Trimble NetR9 for GPS PRN 2 (SVN 61).

6.5   Sub-second Analysis

A different method to overcome the signal processing noise is to increase the C/N_0 of the signal. The strength of the GNSS signals could be increased by using an antenna with higher gain.

However, higher gain antennas become increasingly directional, which limits the ability to capture signals from multiple satellites concurrently and eliminates the ability to use paired differencing to isolate individual satellite clocks. The 1WCP algorithm better suits measurements from a high-gain collection system.

The MAD analysis at sub-second time intervals of data collected by the high-gain radio telescope in Green Bank, West Virginia is presented in Appendix C. This preliminary study was not done at the same level as the studies shown in Chapter 7, however it provides some insight into the development of a system capable of sub-second GNSS oscillator analysis. A lower bound of sub-second stability for the oscillator on SVN 24 (PRN 24 in 2006) was found that no longer depended on the signal power. The necessary signal power to reveal this lower stability bound was on the order of $70\,$dB-Hz, which is a C/N_0 that is difficult to attain without significant gain and can be provided most easily with a very large collection antenna.

Chapter 7

SATELLITE CLOCK EXPERIMENTS

Due to the limited resources on GNSS clock stability for time intervals relevant to RO, collection experiments were proposed to focus on the short-term stability of the GNSS clocks. As the primary measurement of the RO event is the carrier phase, small variations to the signal, either from the atmospheric disturbances or from the source clock, are going to be interpreted similarly when translated to atmospheric quantities. Therefore, the characterization of the clock errors is crucial to the proper identification of structures in the atmosphere.

Several data collection experiments were conducted to assess the GNSS oscillator stability at timescales relevant to RO. The outcome of this oscillator characterization study is important, as the short-term stability affects the quality of the occultation data products. As all future GNSS RO missions plan to use some subset of the GNSS as a signal source, the results presented here can serve as a guide as to which constellation is best for atmospheric observations.

7.1   Background

GNSS AFS stability studies are common throughout the literature, although limited references exist that analyze the oscillators to such short timescales as required for RO. Daly and Kitching (1990) characterized GPS and GLONASS clocks by performing an AD analysis using the time adjustment parameter given by the broadcast ephemerides [16]. The clock correction given in the broadcast message is reported once every two hours, an interval too infrequent for remote sensing applications. Other publications have used carrier phase based interpolation and detrend-

ing methods to obtain AD values for averaging intervals less than 30 seconds, however all utilized clock correction data from reference stations with ultra-stable clocks instead of their own collected data [40, 18, 28]. Hauschild et al. (2012) presents an in depth analysis of the AD for nearly every GNSS satellite, but concerns exist about the Kalman-filtered results. For instance, their Kalman-filtered clock estimation is significantly higher at $\tau \geq 10$ seconds than the one-way and three-way carrier phase methods for the Block IIF satellite, PRN 25 [36]. In addition, the thermal noise of the collection and processing equipment becomes a relevant source of error for time intervals less than and equal to 1 second, and is not accounted for by any of these references.

The satellite clocks analyzed are CFS, RFS, and PHM onboard the present GNSS satellites. As all atomic clocks onboard the GNSS satellites are passive frequency standards, a voltage-controlled crystal oscillator (VCXO) is frequency locked to the free-running atomic standard via a control loop. As a result, they tend to exhibit white frequency noise. The phase, frequency, and frequency drift of the time keeping system (TKS) output on the GPS satellites are fine-tuned from ground control and adjusted to cancel drifts in the atomic frequency output or anomalous frequency departures. A comparison is made between the absorption lines of the VCXO and the atomic reference, and the relative difference is used to adjust the frequency of the VCXO [68]. It has been noted that the existing phase meter is the primary cause of short-term timing instability in the Block IIR TKS for times less than 100 seconds [17].

Several collection experiments were conducted to assess the stability of the various GNSS AFS. Two carrier phase collections were made at CU, one at the National Institute of Standards and Technology (NIST), and one at NASA JPL. The collections at NIST and JPL used AHM as receiver references, allowing for the 1WCP technique of Section 6.3.1 to be employed. The collections at CU had no maser ground references available; thus, the 3CH method was employed.

7.2   Data Collections

The data collections described here support the analysis of the GNSS constellation AFS over $0.5 \leq \tau \leq 200$ seconds. Processing the raw IF samples with an SDR provides the greatest

possible flexibility in the receiver configuration for satellite clock analysis. It also requires additional processing time and complexity. Many COTS receivers have limited flexibility in the choice of loop bandwidth and measurement rate, both of which are easily adjustable in the software receiver. The variable bandwidths of the software receiver allow for the detection of white phase modulation at short timescales, where it dominates the noise variation and is easily detectable in the AD/MAD. The flexibility of the loop bandwidth allows for Allan analysis at a minimal timescale, up to and including the loop bandwidth.

Collection campaigns conducted with the software receiver allow for better knowledge of the internal processing mechanisms, however, are limited to the GPS and GLONASS constellations. The analysis of the Galileo and BeiDou constellations with the software receiver is not yet available. Algorithms and software packages exist to process these systems with the SDR developed at CU, but the accuracy of the carrier phase measurements has not been extensively tested. Thus, the SDR Allan analysis is limited to the GPS and GLONASS constellations. Collections conducted with the COTS receiver (Trimble NetR9) allowed for analysis of satellite clocks from all four constellations. However, the overall quality of the analysis of the data from the COTS receiver is limited because of the unknown internal processing procedures of the NetR9.

7.2.1   University of Colorado

On 25-Jun-2012, raw GPS data were collected from a rooftop antenna at CU in Boulder, Colorado. A Trimble Zephyr Geodetic antenna capable of collecting GPS L1, L2, and L5, as well as GLONASS L1, L2, and L3, was used. The GPS SiGe module, developed by CU, collected the raw IF samples [10]. Approximately 1,000 seconds of raw signal data were collected at a sampling rate of 4 Msps. Figure 7.1 depicts the geometry of the collected satellites and Table 7.1 shows the GPS clock types and satellite blocks of the collected data.

Raw GLONASS data were collected on 27-Jul-2012 from the same location. The same antenna was utilized, however a USRP front-end was used to collect and sample the raw signal. The nominal frequency of the GLONASS signals is outside the capability of the SiGe module used in
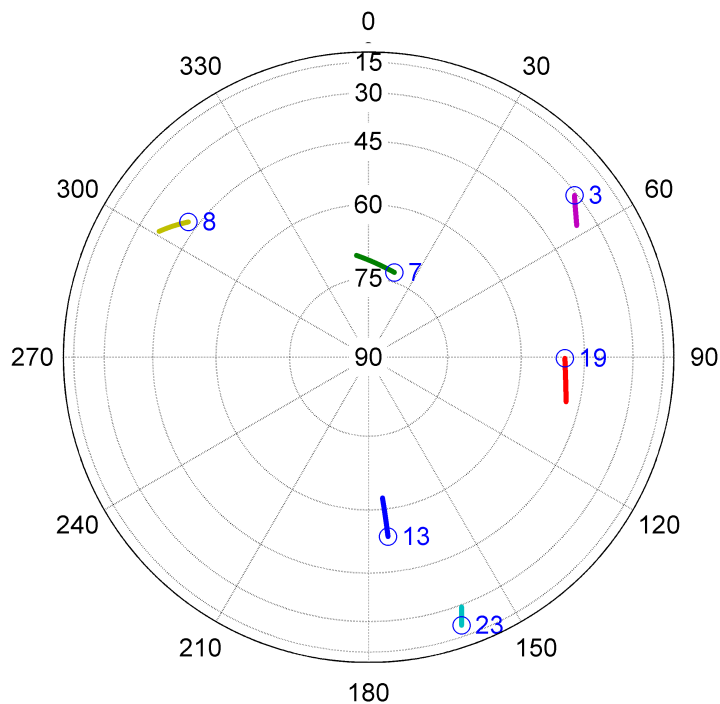
Figure 7.1: Azimuth/elevation plot of the 1000-second GPS data collection on 25-Jun-2012 in Boulder, Colorado. PRNs 3, 7, 8, 13, 19, and 23 were present and analyzed.

Table 7.1: Shown are the PRN number of the satellite, SVN, satellite block, satellite launch date, and atomic clock type for the GPS satellites collected on 25-Jun-2012 in Boulder, Colorado [64, 83].

PRN	SVN	Block	Launch Date	Clock Type
7	48	IIR-M	15-Mar-2008	Rb3
8	38	IIA	06-Nov-1997	Cs4
13	43	IIR	23-Jul-1997	Rb1
23	60	IIR	23-Jun-2004	Rb2
19	59	IIR	20-Mar-2004	Rb3
3	33	IIA	28-Mar-1996	Cs4

the first collection. The raw signal was sampled at a rate of 10 Msps, and a longer data set of approximately 1,500 seconds was collected. The satellite sky geometry is shown in Figure 7.2 and the clock types, frequency channels and almanac numbers are shown in Table 7.2.
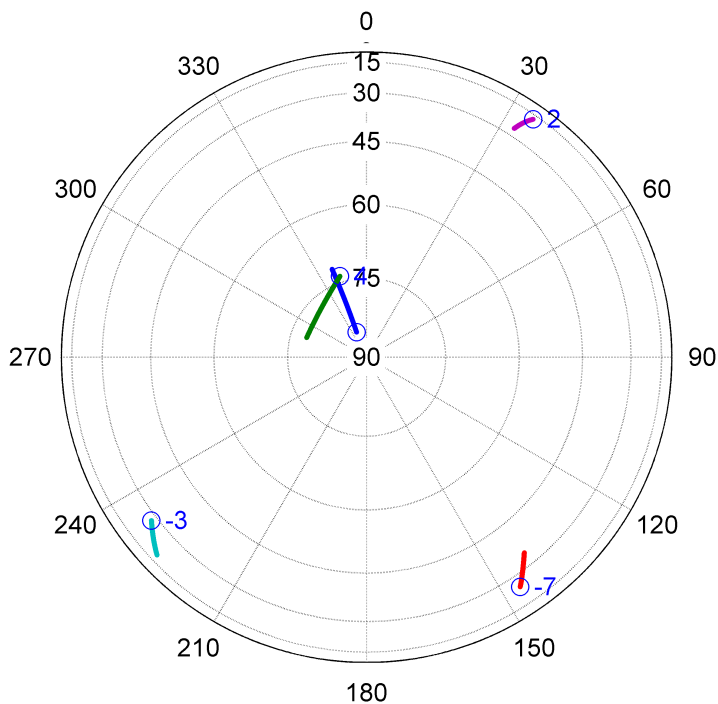
Figure 7.2: Azimuth/elevation plot of the 1500-second GLONASS data collection on 27-Jul-2012 in Boulder, Colorado. Almanac numbers 10, 11, 20, 21, and 22 were present and analyzed. The labels shown are the frequency channel of particular GLONASS satellite.

Table 7.2: Shown are the orbital slot/almanac number, SVN, frequency channel, satellite launch date, and atomic clock type for the GLONASS satellites collected on 27-Jul-2012 in Boulder, Colorado. Note that SVN 701 is also assigned orbital slot number 21, but was marked as in "Flight Tests" and was not used [42].

Almanac	SVN	Frequency Channel	Launch Date	Clock Type
11	723	0	25-Dec-2007	Cs
21	725	4	25-Sep-2007	Cs
10	717	-7	25-Dec-2006	Cs
22	731	-3	02-Mar-2010	Cs
20	719	2	26-Oct-2007	Cs
21	701	-5	26-Feb-2011	Cs

These collections represent a subset of the GPS and GLONASS constellations. Because of the short duration of the collections, the data shows only a snapshot of the constellation stability

performance in time. Comparisons can be made between the GPS and GLONASS satellites to provide guidance on the plausible stability characteristics of the other satellites in the constellation. Again, these collections were made with the SiGe and USRP samplers and processed by the SDR. The internal oscillators on the sampling devices served as the references to maintain lock on the signals, however, the 3CH method is employed to remove the egregious receiver clock error.

7.2.2   Timing Facilities

Two additional long-term collection campaigns were conducted between December 2013 and July 2014 at facilities with available unsteered AHM feeds. Single-frequency carrier phase measurements were used in conjunction with interpolated orbital data from the IGS to obtain clock phase estimates for the MAD calculations, as described in Section 6.1. Long arcs of at least 10,000 seconds were acquired to assess values at averaging intervals of 100-200 seconds with higher certainty. When possible, data were collected at night to minimize the possible influence of the ionosphere. The semi-permanent hardware systems at each of these facilities allowed for collection of all satellites in the GLONASS and Galileo systems, all operating MEOs in BeiDou, and most of the orbiting satellites in the GPS constellation.

For the first collection campaign, a Trimble Zephyr Geodetic antenna was employed on a roof mount on top of the NIST facility in Boulder, Colorado. The signal from the antenna was split and fed to two GNSS receivers: a Trimble NetR9 receiver and a USRP. The external AFS input to both receivers was supplied by one of the unsteered masers at NIST. The maser signal was supplied at 5 MHz, which required a doubler to be compatible with the receivers. A block diagram for the NIST collection setup is shown in Figure 7.3.

The software receiver was used in conjunction with the Trimble NetR9 for verification of the COTS receiver's performance. Since the internal bandwidth of the commercial receiver is not well known, the USRP served to evaluate the NetR9 MAD results, especially for short (sub-second) time intervals. Figure 7.4 compares the MAD values for GPS PRN 4 as produced from the 50 Hz carrier phase observations from the NetR9 to the 1 kHz carrier phase data with PLL bandwidth of
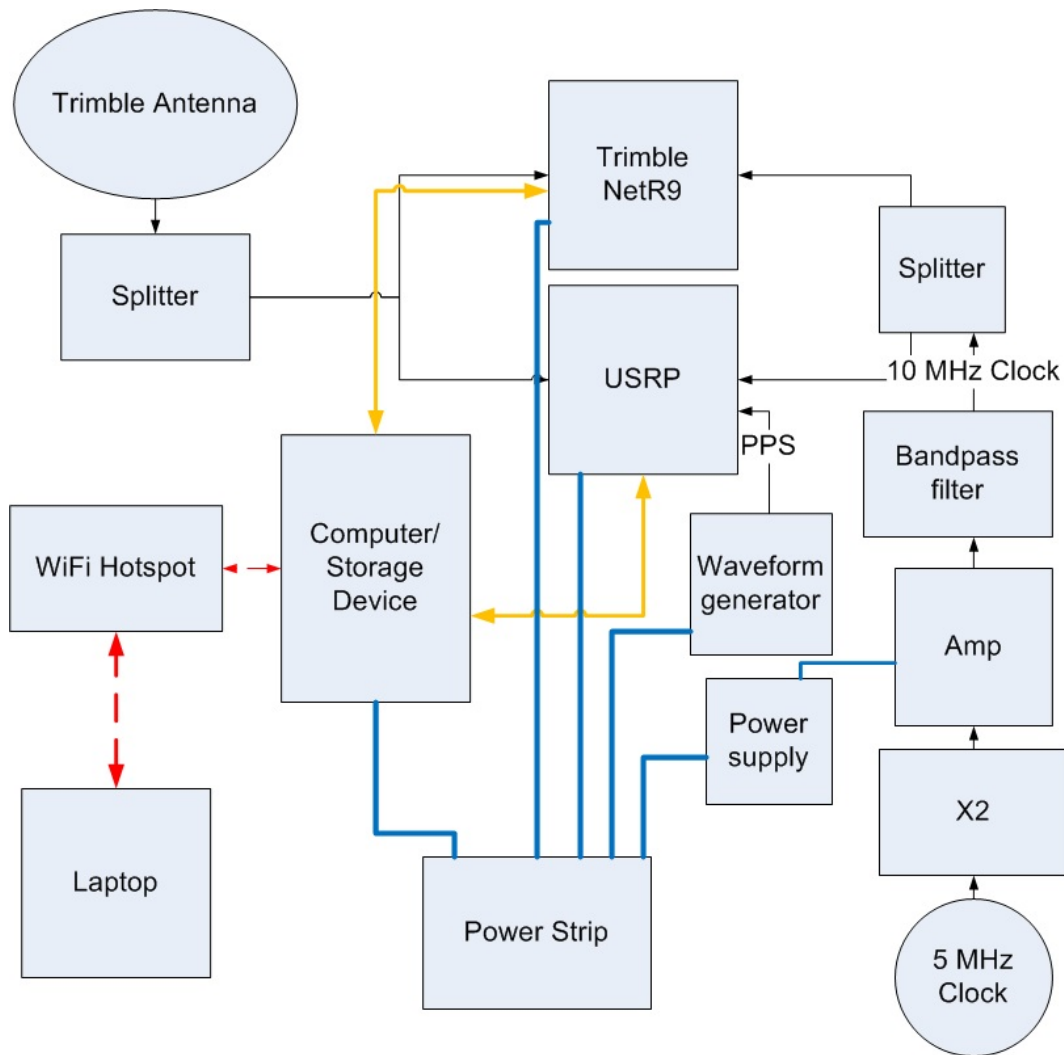
Figure 7.3: Block diagram of the GNSS data collection setup at NIST. The blue lines represent power, yellow represent wired data, and red represent wireless data.

50 Hz from the software receiver. Comparable results from the receivers are seen between averaging intervals of $0.3 \leq \tau \leq 200$ seconds. The sub-second MAD values as produced from the Trimble NetR9 shown in Figure 7.4 do not follow the designated slope of $\tau^{-3/2}$ as predicted for white phase modulation, but rather some unknown filtered response of white phase noise through the COTS receiver [69]. The slope is steeper than $\tau^{-3/2}$ for $0.2 \leq \tau \leq 0.4$ seconds, then subsequently rounds off for $\tau \leq 0.2$ seconds.

Given the very similar results for timescales greater than 0.3 seconds and the desire the
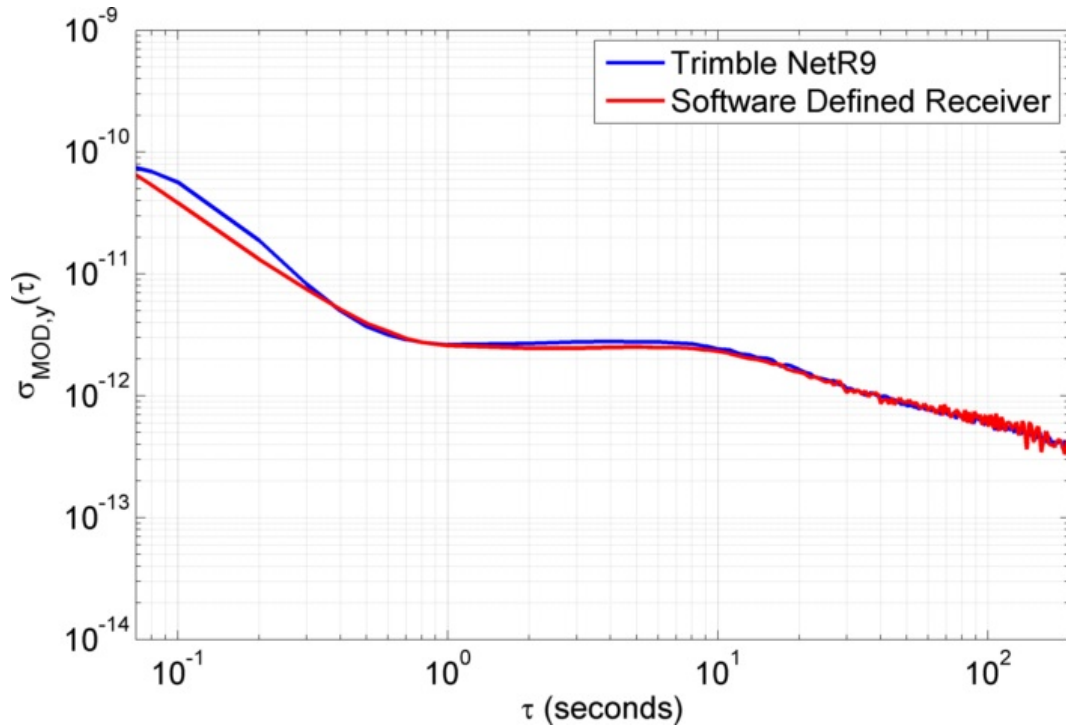
Figure 7.4: Comparison of MAD results over the averaging intervals of $0.07 \leq \tau \leq 200$ seconds from clock phase data from PRN 4 (SVN 34) between the SDR and Trimble NetR9 receivers. The SDR has a PLL bandwidth of $50\,\text{Hz}$, while the NetR9 receiver reported measurements at a $50\,\text{Hz}$ rate.

simplify the processing and computational loads, carrier phase measurements from the Trimble NetR9 were used to obtain clock phase estimates for the MAD results from NIST. The MAD results obtained with the Trimble NetR9 are limited to $1 \leq \tau \leq 200$ seconds. Nevertheless, this analysis range is still important for GNSS RO, as uncorrected satellite clock instabilities cause variations to the carrier phase, which degrade the atmospheric profiles.

For the second collection campaign, conducted at JPL in Pasadena, California, signals were collected by an Allan Osborne narrow-band choke ring antenna placed upon the roof of the timing building on the JPL campus. The antenna feed was fed into the lab where it was split to four different GNSS receivers, one of which was the Trimble NetR9. For the receiver's external AFS, a direct $10\,\text{MHz}$ connection to JPL's AHM was supplied. The hardware setup was much simpler for the collection based at JPL and is shown in Figure 7.5. To ease with computational loads and

processing time, the software receiver was not used in this collection, again limiting the analysis interval to $1 \leq \tau \leq 200$ seconds.
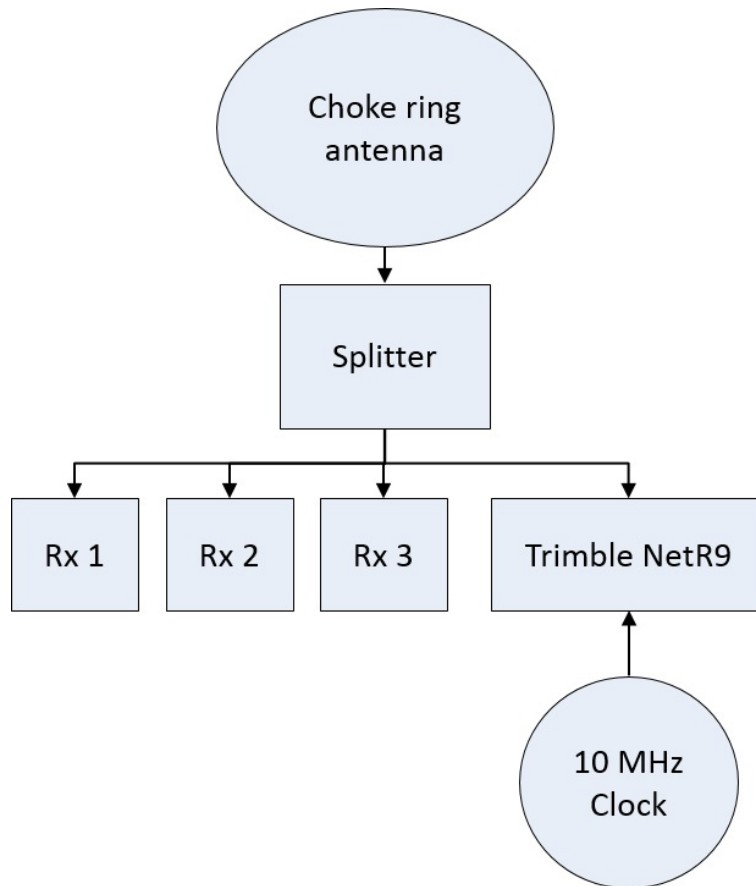
Figure 7.5: Block diagram of the GNSS data collection setup at JPL. The SDR was not employed for this collection location.

Both NIST and JPL supplied direct feeds to Sigma Tau masers, whose AD are well below the AFS of the GNSS constellations for the time scales of interest here [79]. Although data were collected utilizing two different AHM, no discernable differences were found between the MAD results from the two facilities.

7.3   Data Validation

7.3.1   Comparison to Reference Stations

For these studies, delay variations induced on the signal phase due to propagation through the ionosphere and troposphere were assumed to be constant for each satellite over the short observation intervals. The delays were not assumed equal between pairs of satellites, however. Multipath was minimized through unobstructed rooftop placement of the antenna. Residual ionospheric, tropospheric, and multipath errors are assumed to be small and were removed with polynomial detrending [36, 18].

Without multiple data arcs to evaluate against and to average with, short-term ionospheric path delay variations due to scintillation could be interpreted as clock variations in the data sets collected at CU. Therefore, to justify this simplification, the quality of the detrended clock measurements was compared against clock corrections produced by the IGS and Center for Orbit Determination in Europe (CODE). When the receiver clock is less stable than the GNSS clock, as with the CU data sets, the error generated by the receiver clock masks the underlying GNSS satellite clock variation. Under these conditions, comparison of clock phase from a single satellite is not feasible. Single differenced pairs of satellites remove the receiver clock error and can be compared directly to the same single differenced pairs from IGS or CODE. The IGS produces a precise clock correction for the GPS satellites at a 30-second rate and CODE at a 5-second rate [75]. Agreement between the data collected at CU and the reference stations serves as a validity check on the clock phase obtained from the carrier phase measurements from the software receiver.

Figure 7.6 shows the GPS clock offsets as produced by the IGS (30 seconds), CODE (5 seconds), and the SDR at a 20 Hz PLL bandwidth (0.05 seconds) for the PRN 7/PRN 13 difference pair. Senior et al. (2008) states that the precision of the IGS clock products is approximately 1 cm (33 ps) and an accuracy of about 3 cm (100 ps) [75]. The RMS differences shown in Table 7.3 are within these stated precision limits, thus validating the assumption that the variations in the differential ionospheric, tropospheric, and multipath delays were negligible during these collections.
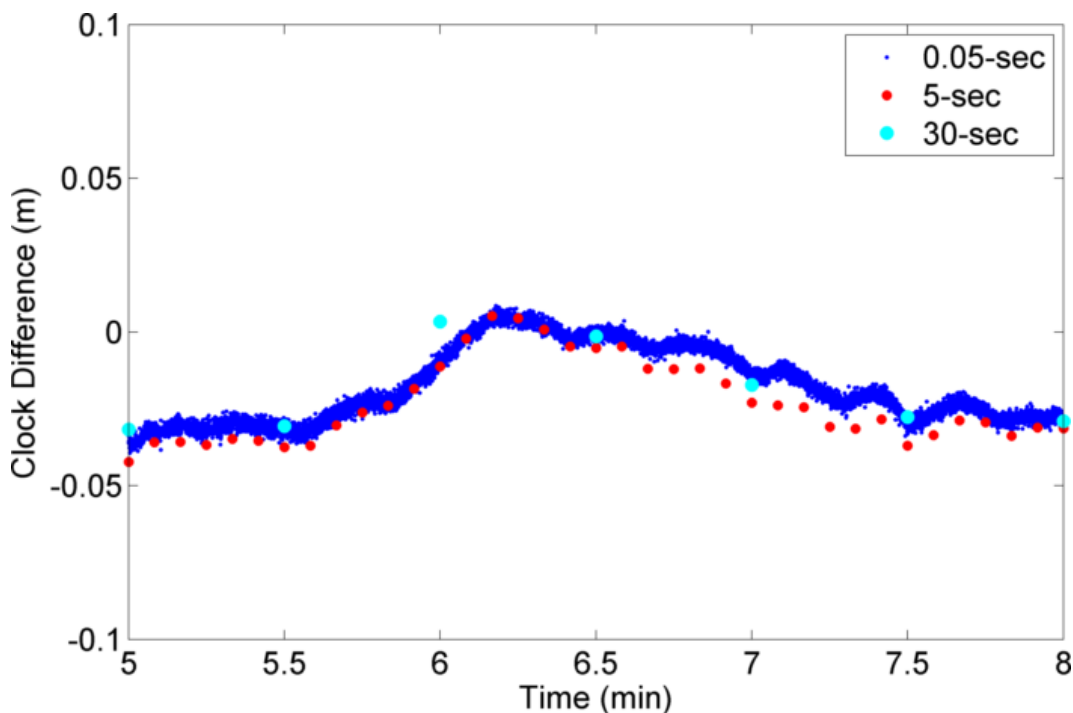
Figure 7.6: Plot of 0.05-second (SDR), 5-second (CODE), and 30-second (IGS) GPS clock differ-ences for the PRN7/PRN13 difference pair for 3 minutes on 25-Jun-2012. The software receiver is able to show higher resolution fluctuations in the clock phase not present in the CODE and IGS data.

Table 7.3: The RMS of the differences between the CU GPS experiment and values for concurrent times reported by IGS and CODE, in picoseconds. Single differencing with data from PRN 7 was performed for all data sets.

Difference pair (PRN)	IGS (ps)	CODE (ps)
7/19	30	14
7/23	34	24
7/3	26	22
7/8	64	24
7/13	27	17

Unlike the data sets collected at CU, the atomic references provided by NIST and JPL allow

for the analysis of the carrier phase series of each individual satellite and the ability to single out

irregular data arcs. Additionally, 37 days of data were collected at NIST and 24 days at JPL.

The quantity of data collected enabled extensive quality assurance as individual outlying data sets

were removed and multiple arcs of the same satellite were averaged to provide the most consistent estimate of the clock performance.

7.3.2   Sample Size Compensation

The triangulation technique of Gray and Allan (1974) modified with single- differenced clock phase data, known as the 3CH method, can often times yield underestimates of the Allan variance when the number of samples is limited [30]. Such a negative bias in the estimate occurs when the number of samples is insufficient to make the cross-correlation terms in Equation 6.9 be negligible. Under these conditions, the Allan variance estimate can be abnormally low or even negative.

To mitigate the insufficient sample problem, a simple approach was developed via simulations. When negative values appear in the summation operator in Equation 6.9, two different summations are performed. In the first summation, the negative values in the summation operator in Equation 6.9 are set to zeros, such that the summation in Equation 6.9 produced an underestimate of the Allan variance. In the second summation, only the positive values are summed, which reduced the number of terms in the summation and yields an overestimate of the Allan variance. These two estimates are then averaged, producing an estimate closer to the true Allan variance. This approach was found to significantly improve the Allan variance estimates based on simulations.

The MAD values can vary significantly over short time intervals, especially for larger values of τ where fewer data points exist for the averaging intervals. To reduce the spread, the measurements were smoothed using a spline interpolator of order three to better reveal the general behavior represented by the noisy estimates of the MAD.

7.4   Allan Deviation Results

The MAD results derived from all collections are presented in the following sections. Comparisons are made between results calculated by the 3CH and 1WCP methods for common satellite types and blocks. For all results, the clock phase values were averaged to reduce signal processing noise and cubic spline interpolation was used to smooth over noisy results due to the limited length

of the data sets. The thermal noise was characterized as white phase noise and removed statistically for sets collected by the software receiver, but not for the COTS receiver results.

7.4.1   GPS and GLONASS

7.4.1.1   Three Cornered Hat

Results for the Allan analysis of the six GPS satellite data sets collected at CU are shown in Figure 7.7. Between $\tau = 1$ and 20 seconds, the MAD values exhibit a positive slope. This differs distinctly from the white frequency noise of passive atomic standards at longer timescales. The positive slope for these time periods is presumably the result of frequency locking a crystal oscillator to a passive atomic standard. Although not entirely obvious from the timescales shown, the slope of the MAD closely approaches $\tau^{-1/2}$ for averaging intervals larger than 30 seconds. This is expected for white frequency noise that results from frequency locking in passive standards [44]. This is typical longer-term behavior of CFS and RFS. The upturn in the MAD at timescales shorter than 1 second suggests white frequency or phase noise [69].

Despite the different GPS satellite blocks being compared here, the MAD values are similar for all averaging intervals. At the time of the collection, PRNs 3 and 8 were both Block IIA satellites and used cesium oscillators, while the remaining satellites were Block IIR and IIR-M satellites with RFS. At longer timescales, PRN 3 exhibits the worst MAD, likely due to a combination of degraded performance with age and improved clock technology over the 17 years since its launch.

MAD results for the five measured GLONASS satellite clocks are shown in Figure 7.8. A positive slope for the MAD occurs for values of τ less than and including $\tau = 3.5$ seconds. This noise is not characteristic of the atomic portion of the CFS and is likely due to a combination of the crystal oscillator frequency locked to the cesium standard and the response of the frequency locked control loop. For timescales larger than approximately $\tau = 10$ seconds, the MAD decreases with an approximate slope of $\tau^{-1/2}$, corresponding to white frequency noise [44].

Figure 7.9 compares the GLONASS and GPS MAD results, including the maximum 3σ error
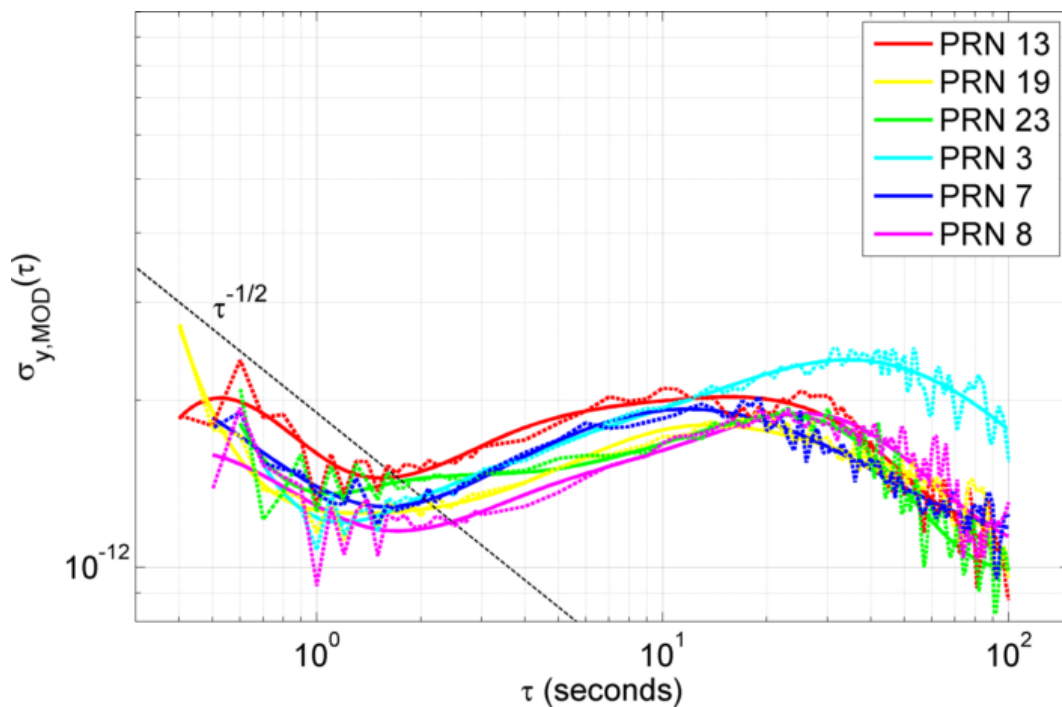
Figure 7.7: Individual GPS satellite MAD, as calculated by the 3CH method, for PRNs 13, 19, 23, 3, 7, and 8. The dashed raw values are smoothed by cubic spline interpolation. The slope of $\tau^{-1/2}$ is shown for reference.
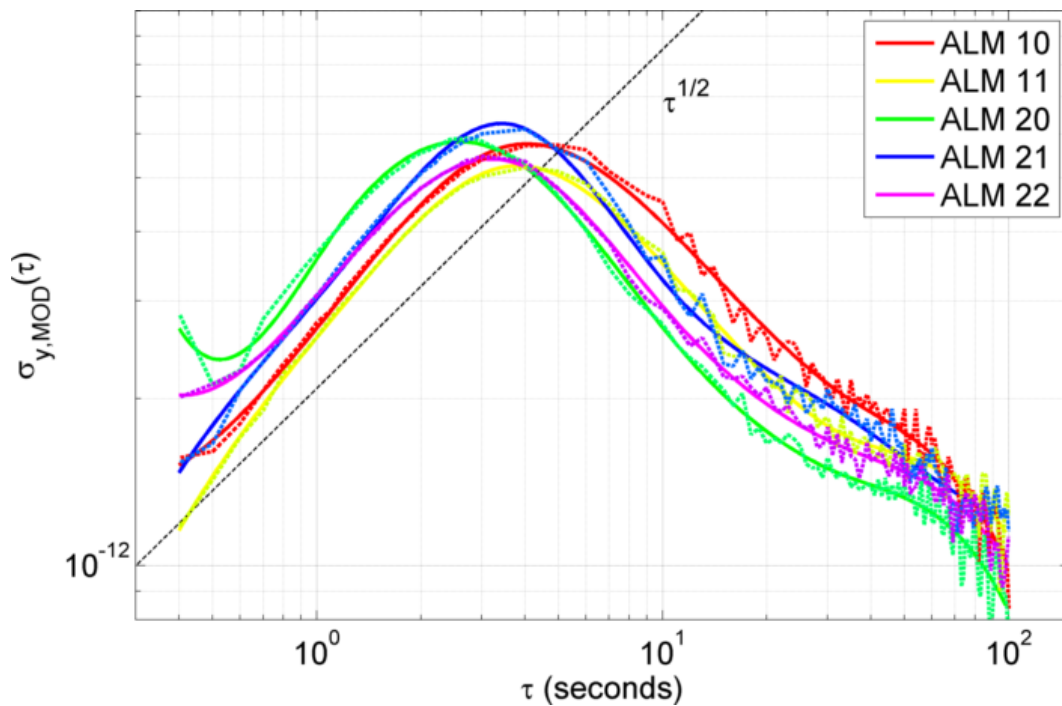
Figure 7.8: Individual GLONASS satellite MAD, as calculated by the 3CH method, for ALMs 10, 11, 20, 21, and 22. The dashed raw values are smoothed by cubic spline interpolation. The slope of $\tau^{1/2}$ is shown for reference.

envelope based upon the raw estimates. The MAD estimates for both constellations overlap for larger values of τ, where the white frequency noise corresponding to atomic clock stability is the primary source of phase error. The $\tau^{-1/2}$ slope is also shown for comparison with MAD values at longer timescales. The fundamental difference between the two GNSS constellations is apparent in the interval of $0.6 \leq \tau \leq 20$ seconds, where the clock stability of the GLONASS satellites is notably worse than GPS.
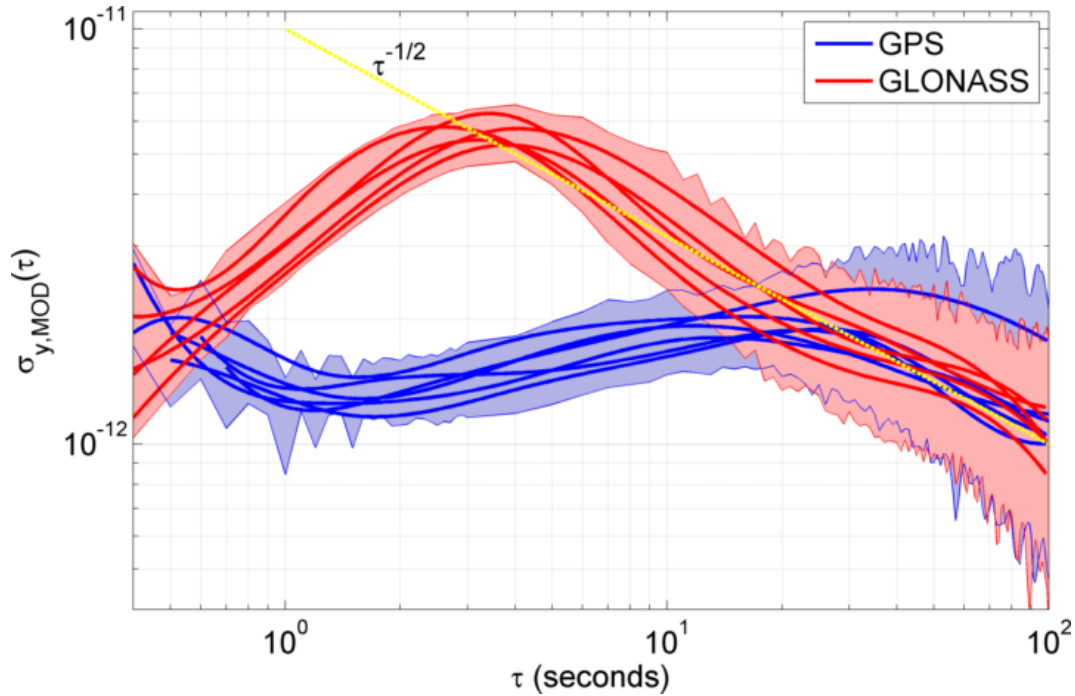
Figure 7.9: Comparison of the smoothed GPS and GLONASS MAD values. Color coordinated 3σ error bar envelopes calculated from the raw measurements are shown for each constellation. The characteristic slope for white frequency noise, $\tau^{-1/2}$, is plotted for comparison.

Estimates from this set of collections can be compared to other published results with AD/MAD estimates corresponding to values of τ that overlap with the short-term results found here. At $\tau = 100$ seconds, it is assumed that the clock noise is behaving as white frequency modulation. Thus, a rough comparison can be made to other studies at this interval, noting that the results from this analysis behave as a MAD, which is approximately $1/\sqrt{2}$ of the traditional AD [69]. Table 7.4 displays the AD/MAD values, all normalized by 10^{-12}, at $\tau = 100$ seconds for two

other studies for comparison.

Table 7.4: Comparison of MAD values as reported by this study, the traditional AD in Hauschild et al. (2012), and MAD in Senior et al. (2008) at $\tau = 100$ seconds [36, 75]. Values are round to the nearest 10^{-13} value. PRN 7 is not reported in the latter study because SVN 37 was replaced by SVN 48 in 2008.

GPS Satellite	Hauschild et al. (2012)	Senior et al. (2008)	Griggs et al. (2014)
PRN 3	2.0	1.6	1.8
PRN 7	1.6	-	1.2
PRN 8	2.2	1.6	1.1
PRN 13	1.7	1.1	1.1
PRN 19	1.5	1.1	1.1
PRN 23	1.4	1.1	1.0

The largest discrepancy appears to be with the Block IIA satellites, where Griggs et al. (2014) yields a lower estimate of the 100 s MAD for PRN 8 and a higher estimate for PRN 3 [32]. The MAD for the Block IIR and IIR-M are within 10% of the results from the other studies at this time interval.

At $\tau = 1$ second, the MAD results cannot be directly compared with studies that use a traditional AD, as the difference between white and flicker phase modulation is not discernible. It is noted, however, that results in Hesselbarth and Wanninger (2008) show similar characteristics in their GLONASS AD results between $\tau = 1$ and 10 seconds to what is shown in this thesis [40]. In contrast to other studies, the noise generated from the receiver's internal processing was reduced here, allowing for a better estimate of the satellite clock stability at $\tau = 1$ second to be exposed.

7.4.1.2 One Way Carrier Phase

The MAD curves for $1 \leq \tau \leq 200$ seconds for the satellites in the GPS constellation are shown in Figure 7.10. A variety of MAD results are found for the different satellites in the GPS constellation, largely dependent upon the satellite block and AFS type. The stability of the Block IIF satellites differs from that of the previous blocks. The Block IIF RFS show the lowest MAD values of the GPS constellation for $\tau \geq 10$ seconds. The white frequency noise slope ($\tau^{-1/2}$) is ap-

parent for timescales as low as one second. The largest difference between the stability performance of the new Block IIF RFS and the older GPS constellation oscillators occurs at averaging intervals between $\tau = 30 - 50$ seconds. The short-term stability improvements shown by the Block IIF RFS are likely due to a stronger discriminator signal and new secondary loop synthesizer, rather than the enhanced physics package [21].
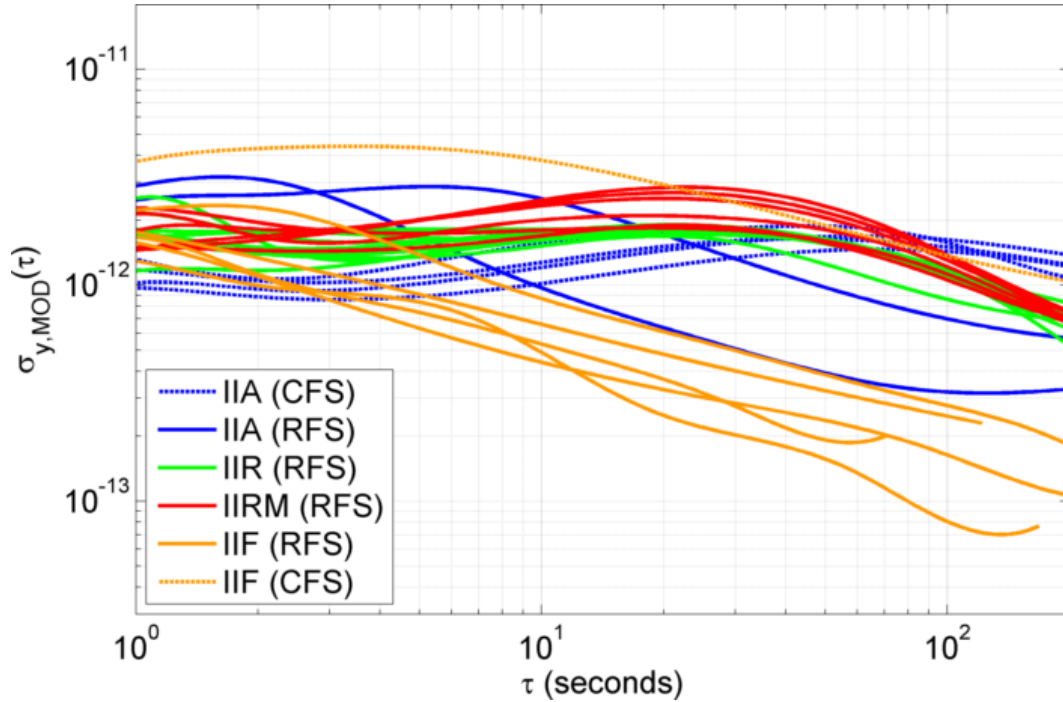
Figure 7.10: MAD, as calculated by the 1WCP method, for GPS satellites, differentiated by satellite block and AFS. Solid lines represent RFS and dashed lines represent CFS.

The RFS on GPS Block IIR, IIR-M, and the IIA satellites carrying CFS have similar stability curves that exhibit a flat or increasing MAD curve for τ values less than 30 seconds. For $\tau \geq 30$ seconds, the stability profiles of these satellites show a decreasing $\tau^{-1/2}$ slope, typical of white frequency modulation at these timescales. The stability curves for the Block IIA RFS show more similarities to the Block IIF RFS than the IIA CFS.

Three groups of behavior can be identified from the stability curves of the GPS constellation, shown in Figure 7.10: the first (Group A) which include the RFS on Block IIA and IIF satellites,

the second (Group B) which include the RFS on the Block IIR and IIR-M and the CFS on IIA, and finally the third (Group C) which includes the sole CFS utilized on a Block IIF satellite, PRN 24 (SVN 65). The Group A AFS show peak instability at $1 \leq \tau \leq 4$ second, while peak instability for Group B occurs between $\tau = 30 - 40$ seconds. Instabilities at longer timescales, such as those from Group B, can be corrected in post-processing by the IGS 30-second clock products. Group C shows the highest short term MAD for averaging intervals less than 20 seconds. PRN 24 has been operating on a CFS since its launch in 2012, which included a fix to its Xenon tube that caused problems previously on PRN 1 (SVN 63) [12].

The MAD curves for the satellites in the GLONASS constellation are shown in Figure 7.11. The GLONASS MAD values for the entire constellation are noticeably higher than all satellites of the GPS constellation for averaging intervals between 1-10 seconds. The characteristic slope of $\tau^{-1/2}$ for the CFS onboard the GLONASS satellites is apparent for averaging intervals $\tau \geq 10$ seconds, however, the dominant noise for shorter averaging intervals appears to be that of the crystal oscillator in the frequency control loop.

Two groups of satellite performance are revealed by Figure 7.11. There exists a distinct change in stability performance between the two groups of satellite clocks based upon the peak instability. These groups can be differentiated by launch date, where satellites launched prior to June 2010 show a peak instability at $\tau \geq 2$ seconds, and satellites launched after this date generally show a higher peak instability at $\tau \leq 2$ seconds. The fact that the groups are distinguishable by launch date indicates a change to hardware, software, and/or construction of the satellite AFS in 2010.

Although the MAD curves generally show better stability at longer timescales for the newer GLONASS satellites, the larger phase errors at short timescales will degrade applications, such as GLONASS RO, that require stability comparable to GPS at 1-second timescales. Such applications will require clock corrections to estimate and remove the oscillator-based errors to achieve stabilities comparable to the other GNSS constellations.
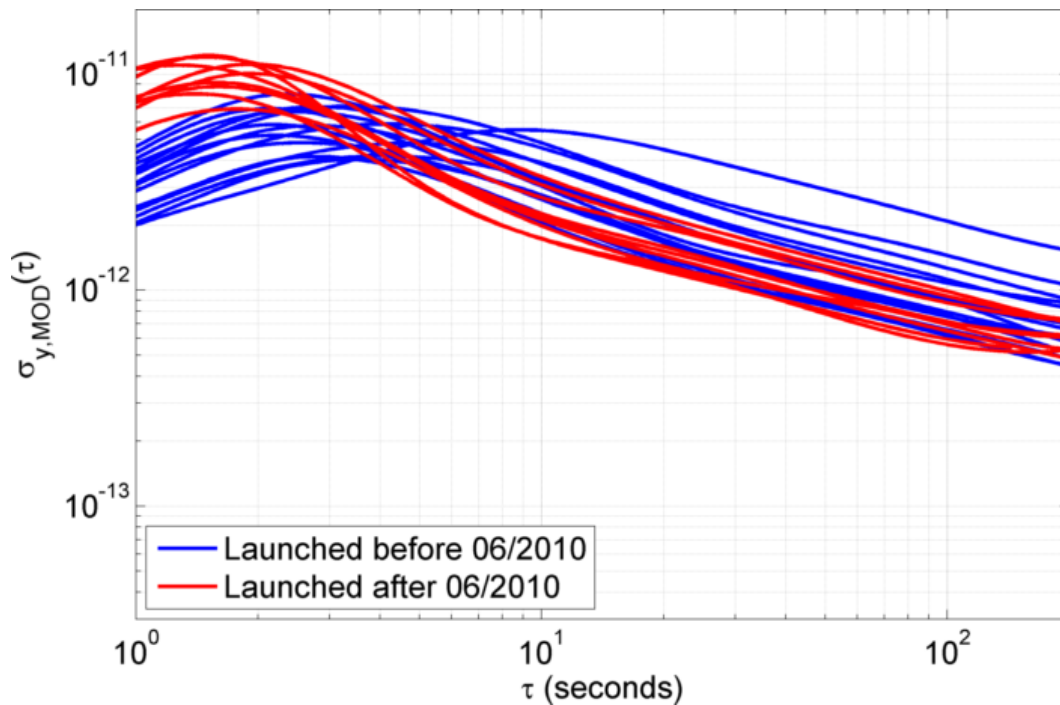
Figure 7.11: MAD, as calculated by the 1WCP method, for GLONASS satellites, differentiated by launch period. All GLONASS satellites carry CFS.

7.4.1.3   Analysis Method Comparison

Despite different processing techniques, the collections from CU and the timing facilities showed very similar results for overlapping time intervals and satellites. The plots in Figure 7.12 isolate the different satellite blocks and types and directly compare the MAD values as computed by the 1WCP and 3CH methods. To minimize confusion in the plots, the error bars for the estimates are not shown here, but are similar to those shown in Figure 7.9.

Although computationally expensive and requires long data arcs of similarly stable oscillators, the 3CH technique is a robust method that allows assessment of satellite clock stability without an atomic reference at the receiver. The 3CH methodology does have severe limitations when comparing oscillators of differing stabilities, as shown in Section 6.3.2.

Both methods also indicate a large discrepancy in stability between the GPS and GLONASS constellations for time intervals between 1-10 seconds. The larger MAD values across these time

(a) GPS Block IIA satellites

(b) GPS Block IIR satellites

(c) GPS Block IIR-M satellites

(d) GLONASS satellites
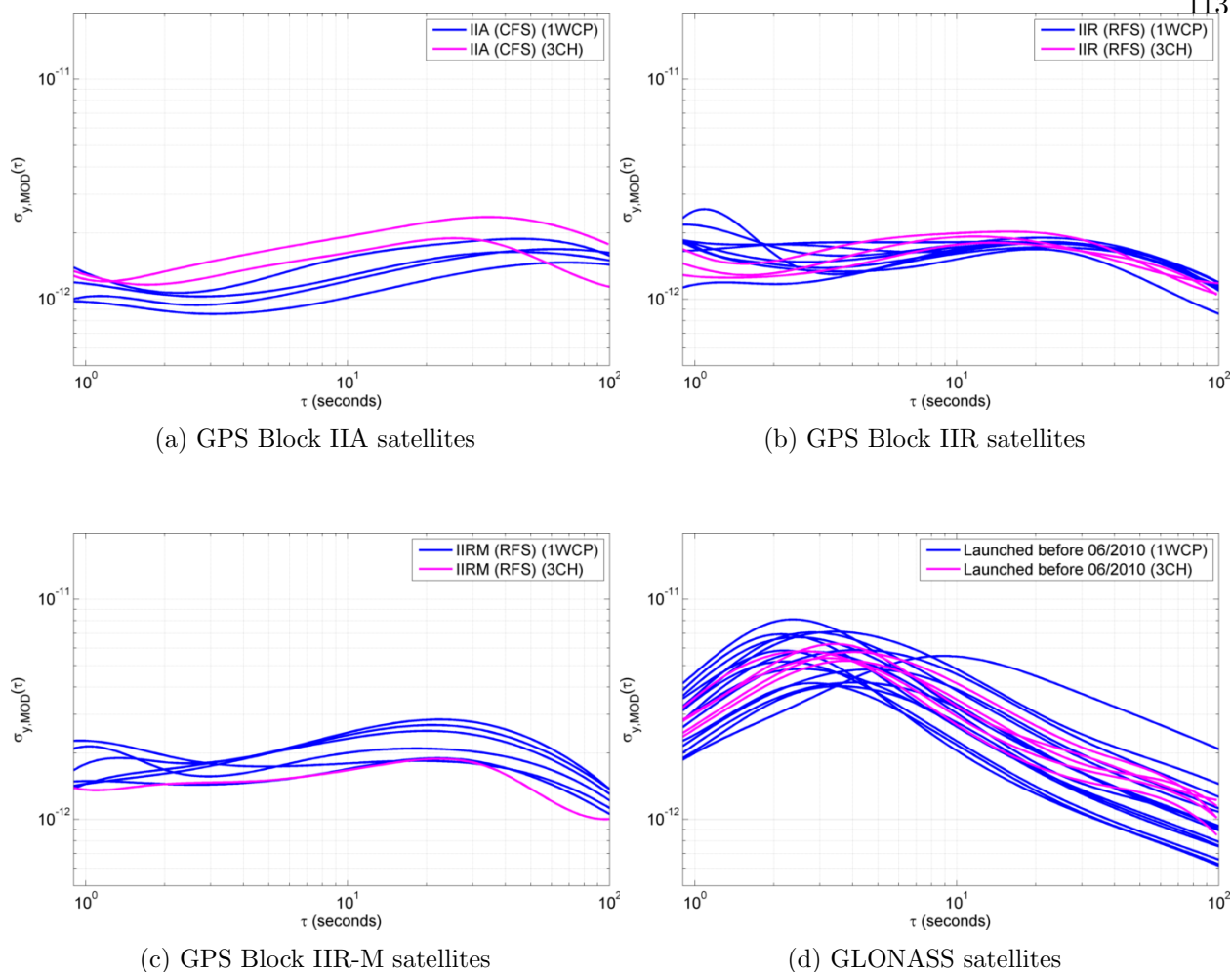
Figure 7.12: Comparison of the MAD results from common groups of satellites as computed by the 1WCP and 3CH methods. The blue curves are calculated by the 1WCP, while the fuchsia curves are calculated with the 3CH method.

intervals are likely due to a combination of the crystal oscillators locked to the CFS and the performance of the frequency locking control loop in the GLONASS CFS.

7.4.2   Galileo and BeiDou

The MAD results for the Galileo In Orbit Validation (IOV) and BeiDou MEO satellites are shown in Figures 7.13 and 7.14, respectively. The Galileo and BeiDou signals were collected only with the COTS receiver at NIST and JPL, thus limiting the analysis to 1WCP for intervals between $1 \leq \tau \leq 200$ seconds. No thermal noise detrending was performed because of the Trimble NetR9
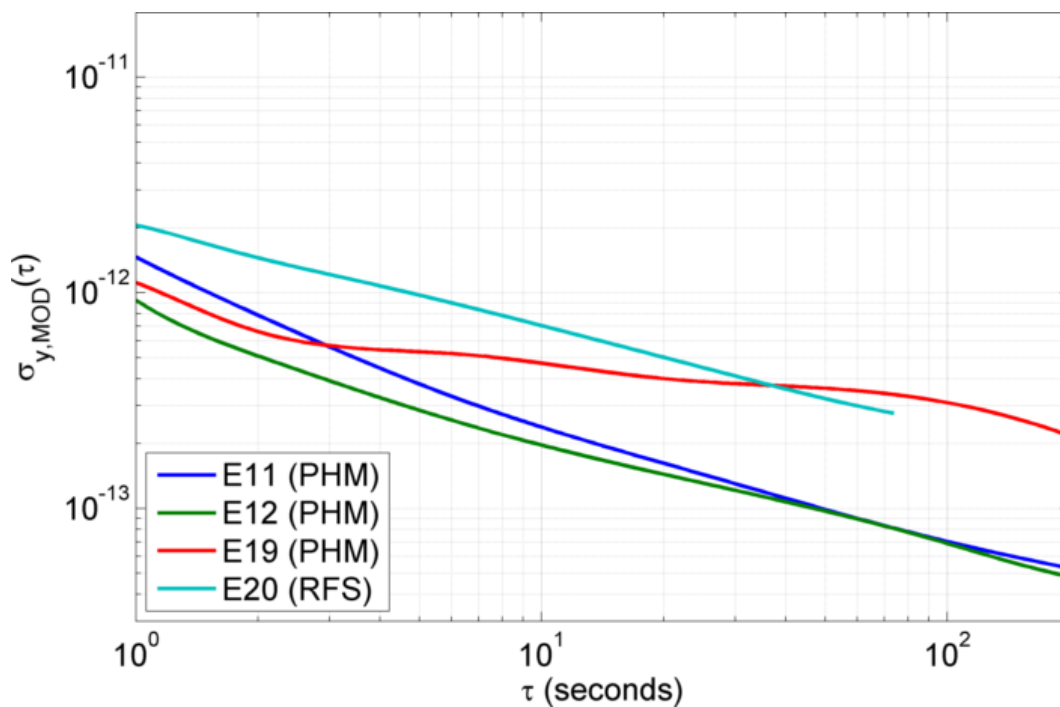
Figure 7.13: MAD, as calculated by the 1WCP method, for Galileo IOV satellites, differentiated by satellite ID and AFS.
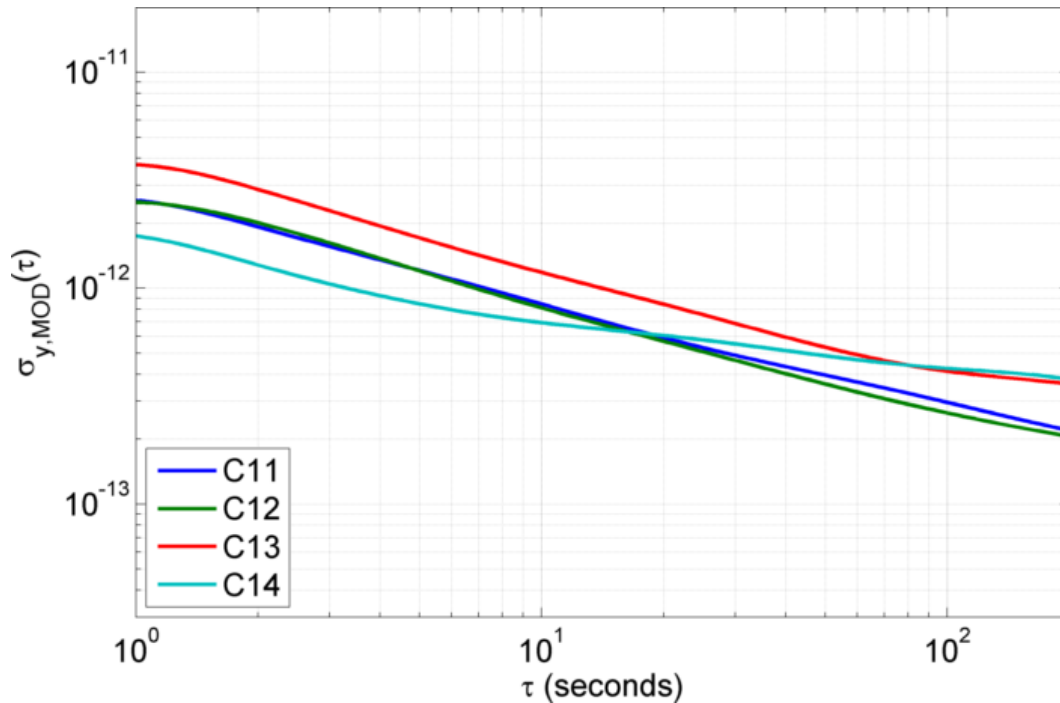
Figure 7.14: MAD, as calculated by the 1WCP method, for BeiDou MEO satellites, differentiated by satellite ID. All BeiDou satellites carry RFS.

response to white phase noise at sub-second time intervals.

Comparison of the MAD results from the various GNSS constellations show that the PHM onboard Galileo E11 and E12 are the most stable signal source at short timescales. The MAD of $\sigma_{y,\text{MOD}} = 10^{-13}$ at $\tau = 50$ seconds for the PHM on E11 and E12 is an order of magnitude better than most GLONASS and GPS Group B and C satellite AFS. The PHM on E19 shows a somewhat different stability profile relative to the other two Galileo satellites carrying PHM, which may have been associated with multiple signal outages for that particular satellite in early 2014 [22].

The stability results of the MAD analysis for the operational MEO satellites of the BeiDou constellation rivaled, or in many cases were better than, the AFS in the GPS constellation. The four MEO AFS showed similar stability results to the Galileo RFS on E20 and the GPS Block IIF RFS, which supports the statement by Lague (2013) of Chinese AFS technology acquisition from SpectraTime [52]. Regardless of the source, the AFS onboard the BeiDou MEO satellites show better stability characteristics for RO than the older GPS blocks and the entire GLONASS constellation.

The short-term MAD values collected at the timing facilities for individual satellites from each constellation shown in the previous subsections are summarized in Appendix B. τ values of 1, 3, 10, 30, and 100 seconds are highlighted for easy comparison between constellations at common intervals. A few MAD values are missing at $\tau = 100$ seconds, due to uncertainty in the estimates with data arcs at lower elevations.

7.5   Implications

While long-term AFS stability is key for navigation utilizing the GNSS, many remote sensing applications require high-rate carrier phase measurements, and subsequently, short-term AFS stability. The GNSS oscillator instabilities presented in the previous section affect the quality of the RO products derived from their signals. The AFS errors translate to a carrier phase error, which can then be mapped to errors in refractivity, pressure, and temperature as the RO technique derives these quantities from the carrier phase of the signal. The maximum carrier phase error due

to oscillator instability is described in the following section.

7.5.1   Carrier Phase Error

Carrier phase errors caused by satellite clock instability can be reduced with periodic correc-
tions. For example, clock corrections given by the IGS allow for the GPS and GLONASS clock error
to be corrected every 30 seconds. The maximum residual error between applied clock corrections
can be estimated using linear interpolation of the clock phase measurements. The following set of
equations relates the residual error in the linear interpolation to the MAD.

The linearly interpolated estimate of a clock phase at the midpoint between two phase mea-
surements separated in time by 2τ is given as follows.

$$\epsilon_{\phi(t)} = \hat{\phi}(t) - \phi(t) \tag{7.1}$$

where

$$\hat{\phi}(t) = \frac{\phi(t+\tau) + \phi(t-\tau)}{2} \tag{7.2}$$

Equation 7.1 can be rewritten as

$$\epsilon_{\phi(t)} = \frac{\phi(t+\tau)}{2} - \phi(t) + \frac{\phi(t-\tau)}{2} \tag{7.3}$$

Equation 7.3 is similar in format to the definition of the AD, given in Equation 6.4. However, since
the MAD is the primary statistic used throughout the thesis, the following relates the maximum
error between two phase estimates to the MAD.

The definition of the MAD, as given by [1] is

$$\sigma_{y,\text{MOD}}^2(\tau) = \frac{1}{2\tau^2} \left\langle \left(\frac{1}{n} \sum_{i=1}^{n} \phi(t_i + n) - 2\phi(t_i) + \phi(t_i - n) \right)^2 \right\rangle \tag{7.4}$$

where $n = \frac{\tau}{\tau_0}$ and τ_0 is the minimum averaging interval (the PLL bandwidth). The definition can
be combined with Equation 7.3 and further reduced to

$$\sigma_{y,\text{MOD}}^2(\tau) = \frac{1}{2\tau^2} \left\langle \left(\frac{1}{n} \sum_{i=1}^{n} 2\epsilon_{\phi(t_i,\tau/\tau_0)} \right)^2 \right\rangle = \frac{2}{n^2\tau^2} \left\langle \left(\sum_{i=1}^{n} \epsilon_{\phi(t_i,\tau/\tau_0)} \right)^2 \right\rangle \tag{7.5}$$

If $\tau = \tau_0$, then this leads to $n = 1$ and Equation 7.5 is reduced to the typical AD case. For cases when τ is a n multiple of τ_0, then the summation term in 7.5 becomes the sum of the error of the phase estimates for larger and larger values of τ. For phase values that are distributed as white Gaussian noise, the assumption can be made that the errors are independent and zero mean, with the following approximately true:

$$\sum_{i=1}^{n} \epsilon_{\phi(t_i, \tau/\tau_0)} \approx n \cdot \epsilon_{\phi(t_i, \tau/\tau_0)} \tag{7.6}$$

Plugging this result back into Equation 7.5 gives

$$\sigma^2_{MOD,y}(\tau) \approx \frac{2}{n^2\tau^2} \left\langle \left(n\epsilon_{\phi(t_i, \tau/\tau_0)} \right)^2 \right\rangle = \frac{2}{\tau^2} \left\langle \epsilon^2_{\phi(t_i, \tau/\tau_0)} \right\rangle \tag{7.7}$$

Since the error term $\epsilon_{\phi(t_i, \tau/\tau_0)}$ is a scalar, the expected value of the square is equal to the square of the expected value. The expected value of the maximum error between two phase points separated by τ becomes

$$\left\langle \epsilon_{\phi(t_i, \tau/\tau_0)} \right\rangle \approx \frac{\tau}{\sqrt{2}} \sigma_{y,MOD}(\tau) \tag{7.8}$$

in units of seconds. If the units desired are cycles, multiply Equation 7.8 by the frequency. If length, multiply Equation 7.8 by the speed of light, c.

7.5.2   Network Corrections

A MAD at a certain time interval can be used to determine the maximum error in clock phase. From this, the rate of clock corrections required to obtain a desired error threshold can be determined. Figure 7.15 presents a plot of the rate of corrections required for the various GLONASS clocks to maintain a particular phase error. The dotted horizontal lines represent phase error requirements corresponding to the best- and worst-case results from the GPS satellites collected (without the IIF CFS) with 30-second IGS clock corrections applied. The red and blue colors correspond to the before/after June 2010 launch date, originally shown in Figure 7.11.

The time interval necessary between corrections of the GLONASS clocks can be inferred from Figure 7.15 for equivalent phase error. In general, more frequent corrections of the GLONASS

Figure 7.15: Necessary clock corrections for phase error thresholds for collected GLONASS satellite clocks. The blue curves represent GLONASS satellites launched prior to June 2010, while the red curves are for those satellites launched after. For reference, the phase error for the worst- and best-case GPS results with 30-second IGS clock corrections applied is shown.

satellite clocks are necessary to achieve the same phase error levels as GPS. Corrections at 12-second intervals would be needed (instead of 30-second corrections) if the phase errors from all GLONASS clocks were required to match those of the worst-case GPS satellite clock collected. To achieve the same carrier phase accuracy the best-case GPS satellite collected here, 1 Hz clock corrections would be needed for the GLONASS satellites.

7.5.3   One-second Errors

While long-term AFS stability is key for GNSS navigation, the short-term stability is, again, imperative for the functionality of RO collections. Future RO missions desire to utilize the signals from the other GNSS constellations, as they will improve the quantity and global distribution of the occultation measurements. Therefore the AFS stability for all GNSS constellation over short

time intervals is critical to the design and performance of present and future occultation missions.

As shown in Section 7.5.1, the maximum carrier phase error (in meters) given a clock correction interval of 2τ is related intrinsically to the MAD as follows.

$$\langle \epsilon_{\phi(t)} \rangle \approx \frac{c\tau}{\sqrt{2}} \sigma_{y,\text{MOD}}(\tau) \tag{7.9}$$

Because of the relatively large instability of the GLONASS constellation versus the other constellations for timescales less than 10 seconds, the focus here is on the residual errors of GLONASS clocks at $\tau = 1$ second. Equation 7.9 requires a MAD at $\tau = 0.5$ seconds to resolve the phase error at $\tau = 1$ second. Therefore, an estimate of the MAD at 0.5 seconds for the GLONASS satellites is needed, without the thermal and receiver noise contribution. Following the data collections at CU, the SDR could provide sub-second results with white phase noise removal, however the USRP used during collections at NIST had limited bandwidth that did not encompass the nominal GLONASS frequency. Instead, the GLONASS MAD estimates at $\tau = 0.5$ seconds are obtained by normalizing and subtracting the sub-second Galileo MAD results from the GLONASS results, which removes the common NetR9 response to the white phase noise contribution.

Figure 7.16 displays the 1-second maximum carrier phase errors calculated by Equation 7.9 for the GLONASS constellation. As in Figure 7.11, the constellation is separated by launch date, with the more recently launched satellites depicted in red. Based on the two modes of behavior that are apparent in the figure, it appears that a change in the GLONASS AFS design was made after June 2010 that degraded the short term performance of GLONASS AFS.

Since the signal phase is the principle component in RO observations, the carrier phase errors from oscillator instabilities can be related to errors in the occultation products. Kursinski Ph.D. dissertation (1997) described the transformation of clock noise in the Fourier frequency domain and presented the fractional error in refractivity, pressure, and temperature from white frequency (WF) and flicker frequency (FF) noises, which are typical of quartz and GPS cesium oscillators [48]. The resulting fractional errors in RO products are translated and scaled for the noise types and magnitudes found this in study.
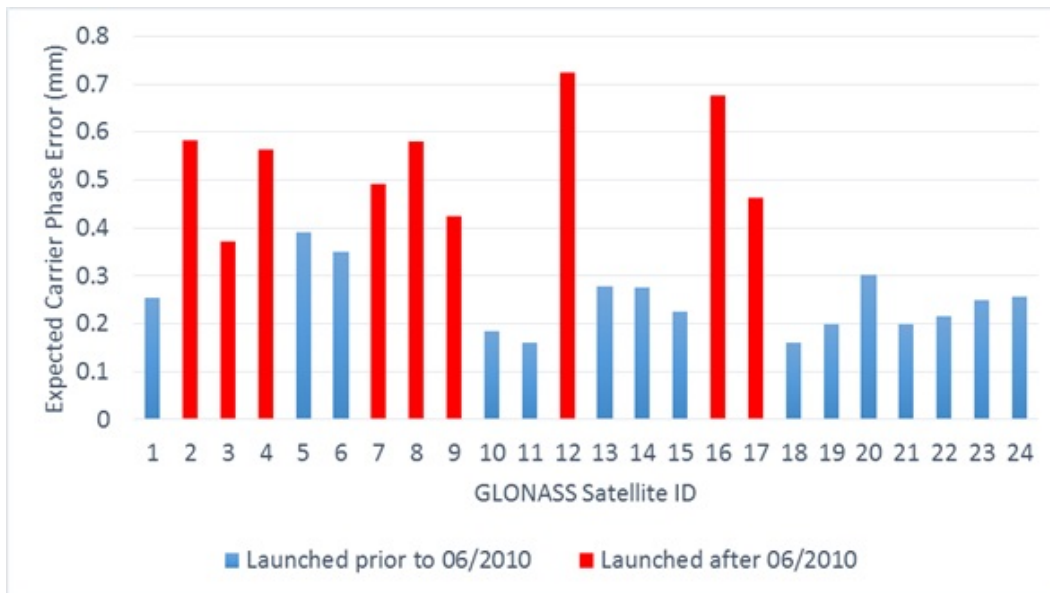
Figure 7.16: Maximum 1-second carrier phase error due to onboard oscillator instabilities for the current GLONASS constellation.

The shape of the MAD due to the GLONASS clock noise for timescales less than 10 seconds appears to be due to a combination of cesium, crystal oscillator, and control loop parameters. The simplest approximation of this noise behavior is FF, which is flat in terms of the MAD [69]. To understand the implications of this noise for atmospheric profiling via RO, the FF results of Kursinksi et al. (2000) are linearly scaled using an average value of $\sigma_{y,\mathrm{MOD}}(\tau = 1 \ \mathrm{sec}) = 5 \times 10^{-12}$ for the GLONASS satellites launched before June 2010, and $\sigma_{y,\mathrm{MOD}}(\tau = 1 \ \mathrm{sec}) = 9 \times 10^{-12}$ for the satellites launched after [50]. The resulting fractional errors in refractivity, pressure, and temperature for the two groups of GLONASS satellites are shown in Figure 7.17, with the same blue/red color scheme for the satellites launched before and after June 2010. These errors are large at high altitudes. While errors from GPS AFS are a relatively minor contribution to the overall RO errors [50], errors of the magnitude of the GLONASS AFS in Figure 7.17 would be the dominant source of RO error above 20 km altitude.

Because of the large magnitude of these GLONASS AFS errors, it is highly desirable to reduce them via high-rate corrections. These corrections must be made sufficiently fast to remove the
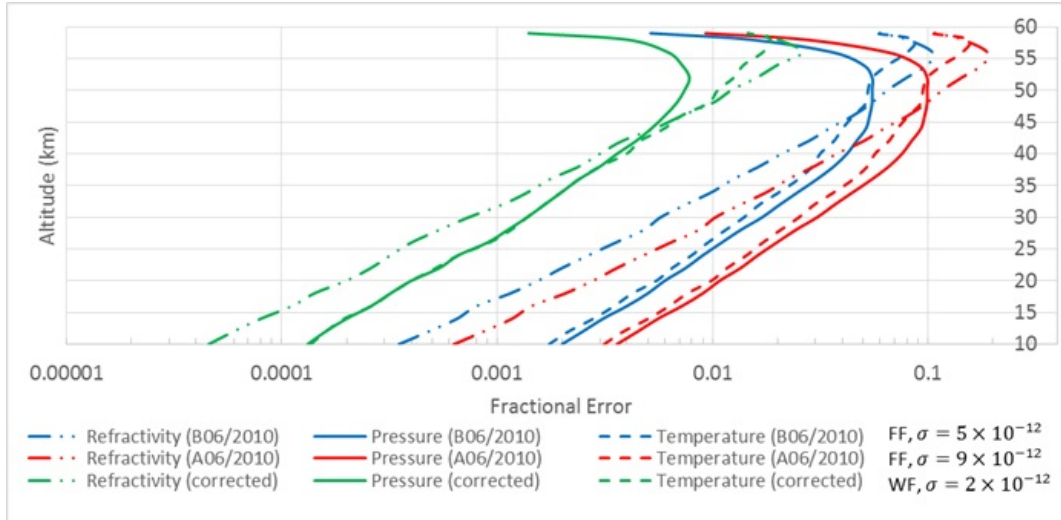
Figure 7.17: Fractional refractivity, pressure, and temperature errors resulting from GLONASS oscillator instabilities based upon the results from Kursinski et al. (2000). A FF with $\sigma_{y,\text{MOD}}(\tau = 1\ \text{sec}) = 5 \times 10^{-12}$ is assumed for the satellites launched before June 2010 (B06/2010) shown in blue, and $\sigma_{y,\text{MOD}}(\tau = 1\ \text{sec}) = 9 \times 10^{-12}$ for the satellites launched after June 2010 (A06/2010) shown in red. The corrected values, assuming a correction system utilizing a CFS with $\sigma_{y,\text{MOD}}(1\ \text{sec}) = 2 \times 10^{-12}$ are shown in green.

worst of the GLONASS phase instabilities. To make high rate corrections during the occultations, a second receiver on the ground or in orbit must be tracking the occulted GLONASS satellite simultaneously during each occultation, as shown in Figure 7.18. By forming the difference, the GLONASS instability cancels for timescales equal to and greater than the differencing rate. After the high rate corrections are applied to eliminate the GLONASS clock errors, there will be residual errors, the GLONASS AFS errors at still shorter time intervals, the instability of the frequency driving the high-rate receiver, and the thermal noise of the two receivers. The residual GLONASS noise is given by Equation 7.9.

If 1-second corrections are supplied by a reference station with a sufficiently good frequency standard, then the sub-second carrier phase errors from the GLONASS oscillators will be bounded by the values given in Figure 7.16. Utilization of a typical cesium or quartz ground reference with $\sigma_{y,\text{MOD}}(1 = \text{sec}) = 2 \times 10^{-12}$ (as shown in Allan et al. (1988)) for 1-second clock corrections will result in WF noise for times scales between $1 \leq \tau \leq 200$ seconds [2]. The subsequent fractional
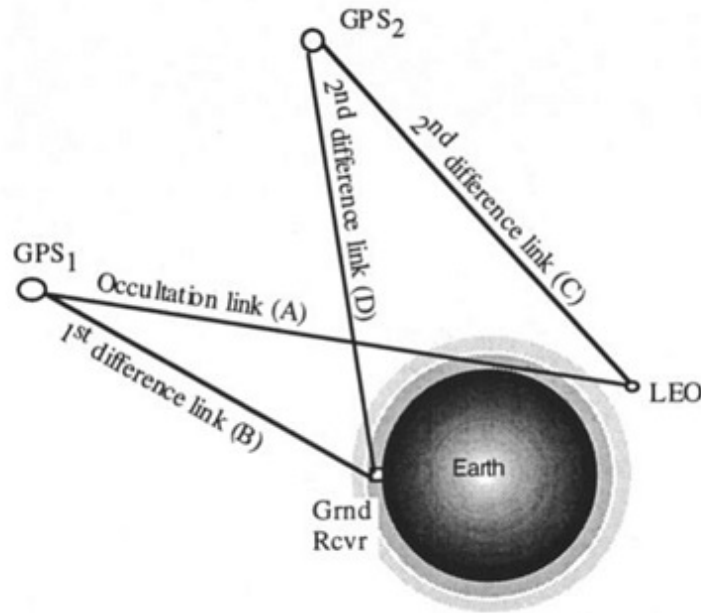
Figure 7.18: Required satellite geometry for clock differencing. Reproduced from Figure 16 in Kursinski et al. (1997) [51].

errors in refractivity, pressure, and temperature can be scaled from Kursinski et al. (2000) and are shown in green in Figure 7.17 [50]. Considerable improvements to the oscillator-induced error are shown in all occultation products.

To obtain the necessary high-rate corrections, a global network of GLONASS capable GNSS receivers are needed. The Crustal Dynamics Data Information System (CDDIS) archive reports a system of permanent GNSS receivers that operate at a 1-second sampling rate [66]. A subset of the network employ a precision external reference and collect GLONASS data and are shown in Table 7.5 [20]. Utilization of high rate clock data from this fraction of the IGS network may provide a satisfactory solution to the 1-10 second clock instabilities of the GLONASS constellation for RO purposes.

7.6   Stability Conclusions

GNSS satellite clock stability results are presented from several collection events. Despite the different hardware configurations and processing schemes, the overall oscillator stability results

Table 7.5: GLONASS capable IGS sites with high rate data collection capabilities and precision receiver clock [66, 20].

Site Name	Location	Clock
arev	Arequipa, Peru	Rb
daej	Daejeon, South Korea	Cs
gmsd	Nakatane Town, Japan	Cs
godz	Greenbelt, U.S.A.	H-maser
gope	Ondřejov, Czech Republic	Cs
hrao	Krugersdorp, South Africa	H-maser
jplm	Pasadena, U.S.A.	Rb
kokv	Kōke'e Park, U.S.A.	H-maser
mas1	Maspalomas, Spain	Cs
mgue	Malargüe, Argentina	H-maser
nnor	New Norcia, Australia	crystal
pie1	Pie Town, U.S.A.	H-maser
vill	Villafranca, Spain	Cs

for overlapping satellites were nearly identical. The single-differenced/3CH methodology provided means to do AFS analysis without a precision oscillator at the receiver with the added computational complexity and processing time. Access to raw AHM output enables a straightforward method to analyze the GNSS clocks through measurements of the carrier phase. GNSS AFS stability curves were created from measurements from both commercial and in-house GNSS receivers. Although the COTS receiver provided an equivalent and simpler method to obtain clock results from averaging intervals from $1 \leq \tau \leq 200$ seconds, the internal mechanisms of the Trimble Net R9 were not understood well enough to allow for sub-second clock analysis. The SDR provides an optimal solution for sub-second AFS analysis, and is explored further in Appendix C.

Comparison of the MAD results for the various GNSS constellations show that the PHM onboard several of the Galileo satellites are the most stable signal source of averaging intervals less than 200 seconds. In both studies, the MAD results for the GLONASS satellites exhibit larger instabilities that peak near $\tau = 1$ second, which will degrade high-rate GNSS applications, including GLONASS RO, if left uncorrected. When using uncorrected GLONASS signals, the RO profile errors at high altitudes may be so large that the maximum altitude of the atmospheric profiles

may have to be lower than the maximum altitude when the other three GNSS constellations are used. Corrections from a subset of the GLONASS capable IGS stations would provide significant improvement to the fractional errors caused by GLONASS clock instabilities if corrections could be made at 1-second intervals.

The GPS Block IIF, BeiDou MEO, and Galileo E20 RFS show comparable MAD results, which if extrapolated to future satellites for these constellations, will benefit GNSS RO because of the better AFS performance at short time intervals. RO performance could be improved further with the use of signals transmitted with mechanical resonators. The sapphire dielectric resonators have achieved AD of between $2-5 \times 10^{-16}$ for integration times between 1-10 seconds [54]; however, further work is necessary to produce space-ready versions of this oscillator.

Chapter 8

SUMMARY AND CONCLUSIONS

The work and results presented here describe studies relevant to the development of a modernized RO receiver and system. The focus of this thesis is to recommend design components of a modernized receiver and constellation which have desirable characteristics for RO collections. With techniques detailed here, we can improve the quantity and quality of measurements made by a future RO receiver and provide algorithms to schedule and make appropriate occultation collections. Studies presented vary from a receiver-level design project to larger scale investigations that affect the design and capability of future occultation constellations. The thesis begins with a ground-based occultation data collection experiment to facilitate receiver algorithm development. Future RO constellations and collection opportunities are simulated and autonomous occultation prediction and scheduling routines are developed. Finally, an in-depth characterization of the GNSS signal quality, in terms of the transmitting clock stability at time intervals relevant to RO, is conducted. Each of the activities presented in the thesis is summarized in turn.

A ground-based RO experiment was conducted to demonstrate the capabilities of a software receiver to process occultation observations from heritage and modernized GNSS signals. Signals from two setting GNSS satellites were taken from the summit of Pikes Peak, CO in October 2011. A recording system was used to capture a digital representation of the signals collected by the antennas. This allowed for post-processing of the data and utilization of a convenient computing environment for algorithm development.

Both open-loop and closed-loop tracking algorithms were employed to process the GNSS

signals. The closed-loop tracking used a PLL to adjust the frequency of the replica signal for correlation based upon the results of the previous measurement. Generally, the closed-loop tracking works well for scenarios with low signal dynamics and an adequate SNR; however, the closed-loop method failed in this setting during tracking in the lower troposphere. The open-loop methodology relied on the accuracy of modeled satellite orbits, receiver clock, and estimates of the atmospheric Doppler shift and delay rather than a feedback loop. Exploiting the open-loop tracking methodology, legacy and modernized GPS signals from the mountain top collection were tracked below the visible horizon.

The focus of the ground-based occultation experiment was to provide insight into the core receiver implementation for an RO-specific GNSS receiver including an understanding of the different tracking loops, scaled data requirements, and signal modulation differences. An increased path delay incurred by the signal due to interaction with the atmosphere was measured in the accumulated phase difference from the Doppler model. The accumulated phase delays were recorded on two different frequencies and were shown to be equivalent. This demonstrated both successful tracking to negative elevation angles and measurement of elongated signal paths.

Multiple simulations were then performed to investigate possible RO mission configurations and occultation opportunities. These simulations varied the number of RO satellites and their respective inclinations and altitudes in an attempt to optimize global coverage and per satellite occultations. Coverage of the mid-latitude regions improved from the addition of high-inclination orbits for the RO satellites. Piggy-backing RO studies to other missions, such as communications missions, could provide added benefit to the quantity of occultation measurements produced.

The next chapter described the development of an occultation scheduler. Real-time orbit estimation of the LEO satellite is necessary to perform data collections of occultation events. Investigation into the navigation accuracy requirements of previous occultation missions provided position and velocity estimate guidelines for a future occultation satellite. Assuming a sufficient estimate of the LEO position and velocity states while in orbit, an autonomous occultation prediction and scheduling code package was developed that allowed collection of signals from all GNSS

constellations solely from their broadcast ephemeris message. Combining the pieces of the constellation simulations and scheduler algorithms, statistics for resource planning were found to assist in setting size limitations on the expected incoming data requirements from a typical orbit of the occultation satellite with all GNSS signals considered.

The final study of the thesis involved a comprehensive characterization of the quality of the GNSS signals based upon the stability of their oscillator controlling the transmitted navigation messages. Through careful data collection techniques and precision modeling, the timing contribution to the carrier phase of the signal was isolated. This timing portion is composed of errors due to the transmitting and receiving oscillators, of which the transmitter stability characteristics are desired. This thesis addresses the receiver clock error in two ways: first by single differencing between pairs of GNSS satellites, as this removes the common receiver clock, and second, by using an ultra-stable reference at the receiver.

The first of two studies conducted to analyze the GNSS clock performance used signals from a subset of the GPS and GLONASS constellations. Because of the large timing errors introduced by the receiver to the data, methodology was developed that allowed for accurate satellite clock stability analysis without an ultra-stable clock at the ground receiver. Variations in the carrier phase caused by the satellite clock were isolated using pairs of single differenced satellites that were multiplied and summed, which reduced the influence of noise from other satellites and isolated the behavior of the clock of interest. Using the 3CH clock isolation method, it was found that the GLONASS atomic frequency standard stability was significantly worse than the GPS stability, warranting a second data collection to verify these results. In addition, the second data collection encompassed all satellites from the GPS and GLONASS constellations, as well as those from the BeiDou and Galileo GNSS constellations.

The second study was conducted to form a comprehensive analysis of clock characteristics for satellite AFS from all GNSS constellations. The data collections, performed at NIST and NASA's JPL facilities, made use of AHM to minimize the impact of the receiver clock and to better isolate the satellite clock contribution to the carrier phase. The oscillators onboard several of the

Galileo satellites were shown to be the most stable signal source for GNSS RO purposes, while the GLONASS oscillators showed the worst short-term stability. Interpolated errors in RO refractivity, temperature, and pressure from the GLONASS oscillators were shown to be the dominant source of RO error, if left uncorrected. As future RO missions have already been designed to use the signals from the GLONASS constellation, it is important to understand that these signals are insufficiently stable and will degrade RO observations. Recommendations for a high-rate GLONASS clock correction network are given, which could provide significant improvement to the fractional errors caused by GLONASS clock instabilities in the derived refractivity, pressure, and temperature values.

With the impending launch of the FORMOSAT-7/COSMIC-2 mission and multiple commercial RO missions awaiting funding, the studies presented here show valuable results necessary for successful utilization of the GNSS signals for atmospheric sensing. Of primary concern is the instability of the GLONASS CFS at timescales important for RO, as it poses a major obstacle in obtaining meaningful data from these satellites. Without high-rate clock corrections to the GLONASS data, the profiles obtained from these satellites by COSMIC-2 and other future missions will be plagued by errors indistinguishable from atmospheric contributions. A clock correction interval of 1-second or less has been shown to achieve the highest quality excess atmospheric phase data for RO using the GPS signals [73]. As the GLONASS constellation makes up a sizable portion of the current GNSS satellites, the amount of useable atmospheric data produced by these RO missions will be significantly reduced without heeding to the suggestions offered here. The signals of the GPS Block IIF, Galileo, and BeiDou satellites, on the other hand, show improved stabilities at time intervals important to RO. The Galileo satellites employing the PHM as a timing reference showed the best stability results over timing intervals important to GNSS RO. The stability analysis of the clocks onboard the BeiDou MEO satellites is the first to show satisfactory oscillator stability at time intervals short enough for RO purposes. Future missions should place higher priority on the collection of the GPS Block IIF, Galileo, and BeiDou satellites, as the clock stability is more favorable.

In conclusion, GNSS RO has proven to be very useful for both weather and climate prediction applications. Nevertheless, the quality of data produced by existing constellations of occultation satellites is declining. Replacement fleets of occultation satellites are imperative to sustain the global coverage and operation impact achieved by the current generation of occultation satellites. By applying the results of the studies described here, future RO constellations can improve the quantity and quality of the radio occultation measurement data, yielding more accurate atmospheric profiles.

Bibliography

[1] D. Allan and J. Barnes. A modified "Allan Variance" with increased oscillator characterization ability. In Proceedings of the 35th Annual Frequency Control Symposium, pages 470–474. IEEE Press, 1981.

[2] D. Allan, H. Hellwig, P. Kartaschoff, J. Vanier, J. Vig, G. Winkler, and N. Yannoni. Standard Terminology for Fundamental Frequency and Time Metrology. In Proceedings of the 42nd Annual Frequency Control Symposium, pages 419–425. IEEE Press, 1988.

[3] R. Anthes, D. Ector, D. Hunt, Y. Kuo, C. Rocken, W. Schreiner, S. Sokolovskiy, S. Syndergaard, T. Wee, Z. Zeng, P. Bernhardt, K. Dymond, Y. Chen, H. Liu, K. Manning, W. Randel, K. Trenberth, L. Cucurull, S. Healy, S. Ho, C. McCormick, T. Meehan, D. Thompson, and N. Yen. The COSMIC/FORMOSAT-3 Mission: Early Results. Bulletin of the American Meteorological Society, 89, 2008.

[4] C. Ao, G. Hajj, T. Meehan, D. Dong, B. Iijima, A. Mannucci, and E. Kursinski. Rising and setting GPS occultations by use of open-loop tracking. Journal of Geophysical Research, 114, 2008.

[5] Y. Aoyama, Y. Shojiy, A. Mousa, T. Tsuda, and H. Nakamura. Down looking GPS occultation measurement on the top of Mt. Fuji. In International Workshop on GPS Meteorology, January 2003.

[6] ARINC Incorporated, El Segundo, CA. Navstar GPS Space Segment / User Segment L5 Interfaces, 2 edition, December 2002.

[7] ARINC Research Corporation, El Segundo, CA. Navstar GPS Space Segment / Navigation User Interfaces, C edition, January 2003.

[8] H. Bock, A. J'aggi, R. Dach, S. Schaer, and G. Beutler. GPS single-frequency orbit determination for low Earth orbiting satellites. Advances in Space Research, 43:783–791, 2009.

[9] G. Born. Coordinate Systems. ASEN 3200 Notes, 2001.

[10] K. Borre, D. Akos, N. Bertelsen, P. Rinder, and S. Jensen. A Software-Defined GPS and Galileo Receiver: A Single-frequency Approach. Birkhäuser, Boston, MA, 2007.

[11] Broad Reach Engineering. Radio Occultation. https://www2.ucar.edu/news/cosmic-visuals-multimedia-gallery, 2006.

[12] A. Butler. Third GPS Satellite in Orbit. http://aviationweek.com/awin/third-gps-iif-satelite-orbit, 2012.

[13] C. Cardinali and S. Healy. Impact of GPS radio occultation measurements in the ECMWF system using adjoint-based diagnostics. Quarterly Journal of the Royal Meteorological Society, 140:2315–2320, 2014.

[14] China Satellite Navigation Office. Interface Control Document, 2.0 edition, December 2013.

[15] L. Cucurull, J. Derber, R. Treadon, and R. Purser. Preliminary Impact Studies Using Global Positioning System Radio Occultation Profiles at NCEP. Monthly Weather Review, pages 136:1965–1877, 2008.

[16] P. Daly and I. Kitching. Characterization of NAVSTAR GPS and GLONASS On-Board Clocks. IEEE AES Magazine, pages 3–9, July 1990.

[17] T. Dass, G. Freed, J. Petzinger, and J. Rajan. GPS Clocks in Space: Current Performance and Plans for the Future. In Proceedings of the 34th Annual Precise Time and Time Interval Meeting, pages 175–192, 2002.

[18] J. Delporte, C. Boulanger, and F. Mercier. Simple Methods for the Estimation of the Short-term Stability of GNSS On-board Clocks. In Proceedings of the 42nd Annual Precise Time and Time Interval Meeting, pages 215–224, 2010.

[19] D. Divis and G. Gibbons. ESA Outlines Efforts to Rescue Wayward Galileo Satellites. http://www.insidegnss.com/node/4179, September 2014.

[20] J. Dow, R. Neilan, and C. Rizos. The International GNSS Service in a changing landscape of Global Navigation Satellite Systems. Journal of Geodesy, 83:191–198, 2009.

[21] R. Dupuis, T. Lynch, and J. Vaccaro. Rubidium frequency standard for the GPS IIF program and modifications for the RAFSMOD program. In Proceedings of the Joint IEEE Frequency Control Symposium and European Frequency and Time Forum, 2008.

[22] European GNSS Service Centre. Constellation Status Information. http://www.gsc-europa.eu/system-status/Constellation-Information, cited March, 2015.

[23] European Space Agency. Galileo Fact Sheet. http://download.esa.int/docs/Galileo_IOV_Launch/Galileo_factsheet_2012.pdf, 2013.

[24] European Union. Interface Control Document, 1.2 edition, 2014.

[25] G. Gibbons. China Plans to Complete BeiDou Ahead of Schedule. http://www.insidegnss.com/node/4040, 2014.

[26] S. Gleason and D. Gebre-Egziabher. GNSS-Applications and Methods. Artech House, Norwood, MA, 2009.

[27] Global Positioning Systems Directorate. Interface Specification, is-gps-200h edition, September 2014.

[28] F. Gonzales and P. Waller. Short term GNSS clock characterization using One-Way carrier phase. IEEE, pages 517–522, 2007.

[29] M. Gorbunov and A. Gurvich. Comparative analysis of radioholographic methods of processing radio occultation data. Radio Science, 35(4):1025–1034, 2000.

[30] J. Gray and D. Allan. A Method of Estimating the Frequency Stability of an Individual Oscillator. In Proceedings of the 8th Annual Symposium on Frequency Control, 1974.

[31] E. Griggs. modifiedallan.m. http://www.mathworks.com/matlabcentral/fileexchange/48217-modifiedallan-data-rate-tau-varargin-, October 2014.

[32] E. Griggs, E. Kursinski, and D. Akos. An investigation of GNSS atomic clock behavior at short time intervals. GPS Solutions, 18:443–452, 2014.

[33] V. Gubenko, A. Pavelyev, I. Kirillovich, V. Andreev, and R. Salimzyanov. Radio occultation studies of internal gravity waves in the Earth's and planetary atmospheres. In Proceedings of the 4th Moscow Solar System Symposium, 2013.

[34] G. Hajj, E. Kursinski, L. Romans, W. Bertiger, and S. Leroy. A technical description of atmospheric sounding by GPS occultation. Journal of Atmospheric and Solar-Terrestrial Physics, 64:451–469, 2002.

[35] F. Harnish, S. Healy, P. Bauer, and S. English. Scaling of GNSS radio occultation impact with observation number using an ensemble of data assimilations. Technical report, ECMWF Technical Memorandum, 2013.

[36] A. Hauschild, O. Montenbruck, and P. Steigenberger. Short-term analysis of GNSS clocks. GPS Solutions, 2012.

[37] S. Healy, J. Haase, and O. Lesne. Abel transform inversion of radio occultation measurements made with a receiver inside the Earth's atmosphere. Annales Geophysicae, 20:1253–1256, 2002.

[38] S. Healy, A. Jupp, and C. Marquardt. Forecast impact experiment with GPS radio occultation measurements. Geophysical Research Letters, 32, 2005.

[39] B. Henson. UCAR Quarterly, Fall 2007: Signal accomplishments. http://www.ucar.edu/communications/quarterly/fall07/cosmic.jsp, 2007.

[40] A. Hesselbarth and L. Wanninger. Short-term Stability of GNSS Satellite Clocks and its Effects on Precise Point Positioning. In Proceedings of ION GNSS 2008, pages 1855–1863, 2008.

[41] X. Hu, X. Gong, C. Xiao, X. Zhang, Y. Fu, and X. Fu. An introduction of mountain-based GPS radio occultation experiments in China. Journal of Advanced Space Research, 2008.

[42] Information-Analytical Centre. GLONASS Constellation Status. www.glonass-center.ru/en/GLONASS/, cited September, 2012.

[43] International GNSS Service. IGS Products. ftp://cddis.gsfc.nasa.gov/, cited August, 2012.

[44] International Radio Consultative Committee. Characterization of Frequency and Phase Noise. Technical Report 580-2, International Radio Consultative Committee, 1986.

[45] J. Jung. Implementation of Correlation Power Peak Ratio Based Signal Detection Method. In GNSS 17th International Technical Meeting of the Satellite Division, September 2004.

[46] E. Kaplan and C. Hegarty. Understanding GPS: Principles and Applications. Artech House, 2005.

[47] Y. Kuo, W. Schreiner, J. Wang, D. Rossiter, and Z. Zhang. Comparison of GPS radio occultation soundings with radiosondes. Geophysical Research Letters, 32, L05817, March 2005.

[48] E. Kursinski. The GPS radio occultation concept: theoretical performance and initial results. PhD thesis, California Institute of Technology, 1997.

[49] E. Kursinski and T. Gebhardt. A Method to Deconvolve Errors in GPS RO-Derived Water Vapor Histograms. Journal of Atmospheric and Oceanic Technology, 31(12):2606–2628, 2014.

[50] E. Kursinski, G. Hajj, S. Leroy, and B. Herman. GPS Radio Occultation Technique. Journal of Terrestrial, Atmospheric, and Oceanic Sciences, 1:53–114, March 2000.

[51] E. Kursinski, G. Hajj, and R. Schofield. Observing Earth's atmosphere with radio occultation measurements using the Global Positioning System. Journal of Geophysical Research, 102:23429–23465, 1997.

[52] D. Lague. In satellite tech race, China hitched a ride from Europe. http://www.reuters.com/article/2013/12/22/breakout-beidou-idUSL4N0JJ0J320131222, 2013.

[53] T. Lulich, J. Garrison, J. Haase, F. Xie, and P. Muradyan. Open Loop Tracking of Radio Occultation Signals from an Airborne Platform. In Proceedings of ION GNSS 2010, 2010.

[54] A. Mann, C. Sheng, and A. Luiten. Cryogenic Sapphire Oscillator with Exceptionally High Frequency Stability. IEEE Transactions on Instrumentation and Measurement, 50(2):519–521, April 2001.

[55] A. Mannucci, S. Lowe, C. Ao, G. Franklin, T. Meehan, F. Xie, Y. Kuo, and W. Schreiner. New Science Opportunities of COSMIC-2/FORMOSAT-7. In Sixth FORMOSAT-3/COSMIC Data Users' Workshop, 2012.

[56] C. McCormick, B. Holz, R. Kursinski, and E. Griggs. Beyond GPS-RO: Mission and Payload Concepts for Atmospheric Remote Sensing for Weather, Climate and Space Weather Monitoring. In OPAC-5, International Workshop on Occultations for Probing Atmosphere and Climate, September 2013.

[57] W. Melbourne. Radio Occultations Using Earth Satellites. Wiley-Interscience, Hoboken, NJ, 2005.

[58] P. Misra and P. Enge. Global Positioning System, Signals, Measurements, and Performance. Ganga-Jamuna Press, Lincoln, MA, 2001.

[59] O. Montenbruck, Y. Andres, H. Bock, R. van Helleputte, J. van den Ijssel, M. Loiselet, C. Marquardt, P. Silvestrin, P. Visser, and Y. Yoon. Tracking and orbit determination performance of the GRAS instrument on MetOp-A. GPS Solutions, 12:289–299, April 2008.

[60] O. Montenbruck, A. Hauschild, Y. Andres, A. von Engeln, and C. Marquardt. (Near-)real-time orbit determination for GNSS radio occultation processing. GPS Solutions, 17:199–209, June 2012.

[61] O. Montenbruck and P. Ramos-Bosch. Precision real-time navigation of LEO satellites using global positioning system measurements. GPS Solutions, 12:187–198, October 2007.

[62] O. Montenbruck, P. Swatschina, M. Markgraf, S. Santandrea, J. Naudet, and E. Tilmans. Precision spacecraft navigation using a low-cost GPS receiver. GPS Solutions, 16:519–529, January 2012.

[63] Moog Broad Reach. Spaceborne GPS Receivers. www.broadreachengineering.com/products/ spaceborne-gps-receivers/, cited April, 2013.

[64] National Geospatial-Intelligence Agency. Current GPS Satellite Data. http://earth-info.nga.mil/GandG/sathtml/satinfo.html, cited 2012.

[65] National Weather Service. Tropical Cyclone Formation Regions. http://www.srh.noaa.gov/jetstream/tropics/tc_basins.htm, 2011.

[66] C. Noll. The Crustal Dynamics Data Information System: A resource to support scientific analysis using space geodesy. Advances in Space Research, 45, 2010.

[67] L. Olsen, A. Carlstrom, and P. Hoeg. Ground-Based Radio Occultation Measurements Using the GRAS Receiver. In ION International Technical Meeting, 2004.

[68] J. Petzinger, R. Reith, and T. Dass. Enhancements to the GPS Block IIR Timekeeping System. In Proceedings of the 34th Annual Precise Time and Time Interval Planning Meeting, pages 89–107, 2002.

[69] W. Riley. Handbook of Frequency Stability Analysis, National Institute of Standards and Technology Special Publication. Technical report, U.S. Department of Commerce, Boulder, CO, 2008.

[70] C. Rocken, R. Anthes, M. Exner, D. Hunt, S. Sokolovskiy, R. Ware, M. Gorbunov, W. Schreiner, D. Feng, B. Herman, Y. Kuo, and X. Zou. Analysis and Validation of GPS/MET Data in the Neutral Atmosphere. Journal of Geophysical Research, 102:29849–29866, 1997.

[71] Russian Institute of Space Device Engineering. Interface Control Document, 5.1 edition, 2008.

[72] M. Schenewerk. A brief review of basic GPS orbit interpolation strategies. GPS Solutions, 6:265–267, 2003.

[73] W. Schreiner, C. Rocken, S. Sokolovskiy, and D. Hunt. Quality assessment of COSMIC/FORMOSAT-3 GPS radio occultation data derived from single- and double-difference atmospheric excess phase processing. GPS Solutions, July 2009.

[74] W. Schreiner, S. Sokolovskiy, D. Hunt, C. Rocken, and Y. Kuo. Analysis of GPS radio occultation data from the FORMOSAT-3/COSMIC and Metop/GRAS missions at CDDAC. Atmospheric Measurement Techniques, October 2011.

[75] K. Senior, R. Beard, and J. Ray. Characterization of Period Variations in the GPS Satellite Clocks. Technical Report NRL/FR/8150–08-10,163, Naval Research Laboratory, 2008.

[76] M. Sharawi, D. Akos, and D. Aloi. GPS C/N_0 Estimation in the Presence of Interference and Limited Quantization Levels. IEEE Transactions on Aerospace and Electronic Systems, 43(1):227–238, January 2007.

[77] S. Sokolovskiy. Tracking tropospheric radio occultation signals from low Earth orbit. Radio Science, 36(3):483–498, 2001.

[78] S. Sokolovskiy, C. Rocken, W. Schreiner, D. Hunt, and J. Johnson. Postprocessing of L1 GPS radio occultation signals recorded in open-loop mode. Radio Science, 44, 2009.

[79] T. K. Tucker. Operating and environmental characteristics of sigma tau hydrogen masers used in the very long baseline array (VLBA). In Proceedings of the 20th Annual Precise Time and Time Interval Applications Planning Meeting, page 325:336, 1988.

[80] D. Turbiner, L. Young, and T. Meehan. Phased Array GNSS Antenna for the FORMOSAT-7/COSMIC-2 Radio Occultation Mission. In Proceedings of the 25th International Technical Meeting of the Satellite Division of the Institute of Navigation, 2012.

[81] G. Tyler. Radio Occultation Experiments in the Outer Solar System with Voyager. Proc. IEEE, 75:1404–1431, 1987.

[82] United States Department of Defense, Washington, D.C. GPS Standard Positioning Service Performance Standard, 4th edition, September 2008.

[83] United States Naval Observatory. GPS Constellation Status. ftp://tycho.usno.navy.mil/pub/gps/gpstd.txt, cited 2012.

[84] University Corporation for Atmospheric Research. FORMOSAT-7/COSMIC-2 (COSMIC-2) Science Mission. http://www.cosmic.ucar.edu/cosmic2/index.html, 2014.

[85] University Corporation for Atmospheric Research. Constellation Observing System for Meteorology, Ionosphere, and Climate. http://www.cosmic.ucar.edu/ro.html, cited April, 2014.

[86] D. Vallado and P. Crawford. SGP4 Orbit Determination. In Proceedings of AIAA/AAS Astrodynamics Specialist Conference and Exhibit, 2008.

[87] V. Vorob'ev and T. Krasil'nikova. Estimation of the accuracy of the atmospheric refractive index recovery from Doppler shift measurements at frequencies used in the NAVSTAR system. Atmospheric and Oceanic Physics, 29:602–609, 1994.

[88] J. Walker. Satellite constellations. British Interplanetary Society, 37:559–572, December 1984.

[89] S. Wallner. GNSS frequency bands. http://www.navipedia.net/index.php/GNSS_signal, 2014.

[90] E. Weisstein. Point-Line Distance: 3-Dimensional. http://mathworld.wolfram.com/Point-LineDistance3-Dimensional.html, cited 2014.

[91] J. Wickert, G Michalak, T. Schmidt, G. Beyerle, C. Cheng, S. Healy, S. Heise, C. Huang, N. Jakowski, W. K'ohler, C. Mayer, D. Offiler, E. Ozawa, A. Pavelyev, M. Rothacher, B. Tapley, and C. Arras. GPS radio occultation: Results from CHAMP, GRACE and FORMOSAT-3/COSMIC. Terrestrial Atmospheric and Oceanic Sciences, 20:35–50, 2009.

[92] T. Yunck, G. Lindal, and C. Liu. The Role of GPS in Precise Earth Observations. In Location and Navigation Symposium. IEEE Position, Nov.29-Dec.2 1988.

[93] T. Yunck, B. Parkinson, and J. Spilker. Global Positioning System: Theory and Applications. AIAA, Washington, D.C., 1996.

[94] C. Zuffada, G. Hajj, and E. Kursinski. A novel approach to atmospheric profiling with a mountain-based or airborne GPS receiver. <u>Journal of Geophysical Research</u>, 104, 1999.

Appendix A

OCCULTATION SCHEDULER SIMULATION RESULTS

The detailed scheduling results from Chapter 5 are shown here. Figure A.1 depicts the scheduling results as a timeline for all constellations for one orbit of the occultation satellite. Overlapping occultation events between constellations are more easily found in this combined figure. Table A.1 shows the first 30 minutes of tabular results from the same occultation simulation.
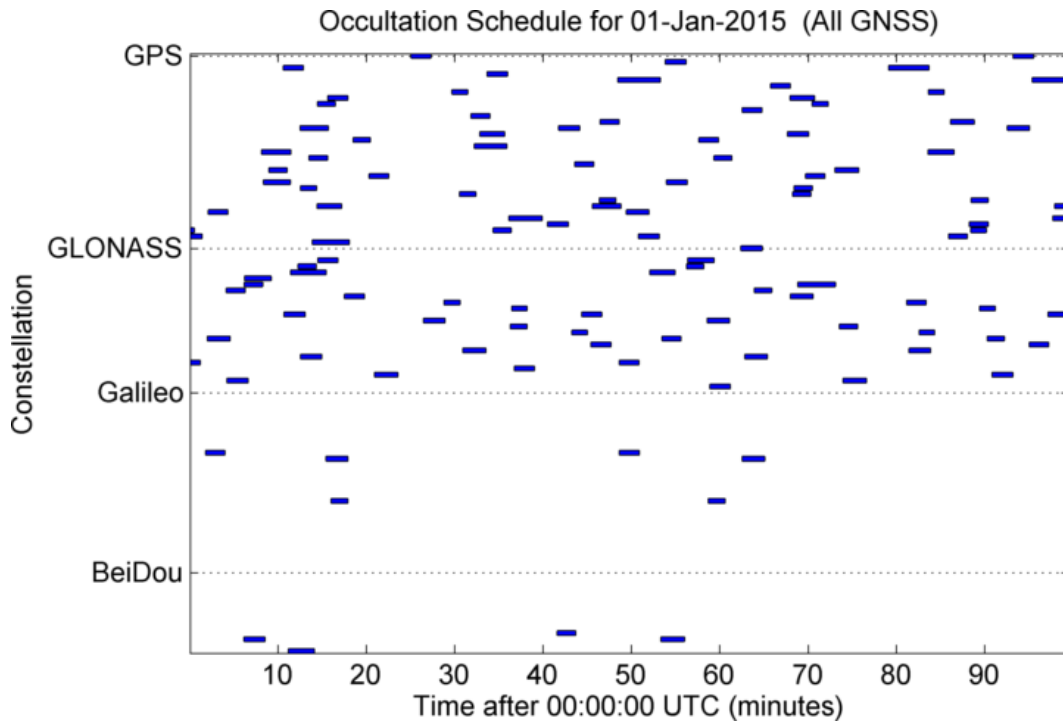

Figure A.1: Timeline of geometric occultation events between a potential RO satellite and all GNSS constellations on 1-Jan-2015 for the period of one LEO orbit.

Table A.1: Tabular occultation scheduling results from the first 30-minutes of the simulated RO orbit. Listed are the occultation start date and time, occultation duration (in seconds), the source constellation and satellite identification number, the occultation type, and the latitude and longitude drift values (in degrees) over the course of the occultation event.

Start time	Dur (sec)	Constellation	Sat ID	Occ Type	Lat Drift (°)	Lon Drift (°)
01-Jan-2015 00:00:02	83	GPS	31	Rising	2.250	3.471
01-Jan-2015 00:00:02	71	GLONASS	20	Setting	0.906	0.494
01-Jan-2015 00:01:49	131	Galileo	11	Setting	2.340	-0.793
01-Jan-2015 00:02:00	156	GLONASS	16	Rising	4.336	6.732
01-Jan-2015 00:02:06	135	GPS	27	Setting	2.918	-1.169
01-Jan-2015 00:04:09	130	GLONASS	8	Rising	3.334	-1.807
01-Jan-2015 00:04:14	143	GLONASS	23	Rising	3.249	-0.642
01-Jan-2015 00:06:09	143	BeiDou	12	Setting	3.782	-1.668
01-Jan-2015 00:06:11	126	GLONASS	7	Rising	1.082	2.910
01-Jan-2015 00:06:13	181	GLONASS	6	Rising	7.864	5.243
01-Jan-2015 00:08:09	199	GPS	17	Rising	8.312	0.553
01-Jan-2015 00:08:21	183	GPS	22	Setting	6.942	-2.495
01-Jan-2015 00:08:58	124	GPS	20	Rising	1.038	1.322
01-Jan-2015 00:10:36	137	GPS	3	Rising	1.750	5.104
01-Jan-2015 00:10:39	147	GLONASS	12	Setting	2.517	6.179
01-Jan-2015 00:11:10	178	BeiDou	14	Rising	5.529	8.059
01-Jan-2015 00:11:25	242	GLONASS	5	Setting	11.494	-3.975
01-Jan-2015 00:12:16	124	GLONASS	4	Setting	1.867	-1.145
01-Jan-2015 00:12:29	193	GPS	13	Setting	5.088	9.220
01-Jan-2015 00:12:32	110	GPS	23	Rising	0.601	-0.085
01-Jan-2015 00:12:33	145	GLONASS	19	Setting	3.495	-1.473
01-Jan-2015 00:13:30	127	GPS	18	Setting	1.820	-0.676
01-Jan-2015 00:13:52	252	GPS	32	Rising	11.227	9.011
01-Jan-2015 00:14:24	168	GPS	26	Setting	3.173	7.984
01-Jan-2015 00:14:27	122	GPS	9	Rising	3.573	-0.594
01-Jan-2015 00:14:30	137	GLONASS	3	Setting	1.380	4.346
01-Jan-2015 00:15:25	151	Galileo	12	Setting	4.313	-2.537
01-Jan-2015 00:15:38	136	GPS	8	Rising	3.215	12.062
01-Jan-2015 00:15:59	116	Galileo	19	Setting	0.973	-0.213
01-Jan-2015 00:17:31	137	GLONASS	9	Rising	3.780	15.978
01-Jan-2015 00:18:29	118	GPS	15	Setting	0.213	3.268
01-Jan-2015 00:20:18	134	GPS	21	Setting	1.967	0.231
01-Jan-2015 00:20:54	160	GLONASS	22	Rising	2.946	8.077
01-Jan-2015 00:25:03	135	GPS	1	Rising	-2.239	1.098
01-Jan-2015 00:26:27	147	GLONASS	13	Setting	-1.751	-350.617
01-Jan-2015 00:28:46	110	GLONASS	10	Rising	-1.323	-3.074
01-Jan-2015 00:29:40	108	GPS	7	Rising	0.445	2.401

Appendix B

GNSS ALLAN DEVIATION ANALYSIS

Table B.1: Clock MAD values for averaging intervals of $\tau = 1, 3, 10, 30$, and 100 seconds for satellites collected from the GPS constellation using 1WCP.

PRN	SVID	Series	Clock	Averaging Intervals of MAD				
				1s	3s	10s	30s	100s
G01	63	IIF	RB	2.18E-12	1.87E-12	8.34E-13	4.98E-13	2.66E-13
G02	61	IIR	RB	1.15E-12	1.22E-12	1.58E-12	1.71E-12	1.10E-12
G03	33	IIA	CS	1.29E-12	1.10E-12	1.54E-12	1.86E-12	1.55E-12
G04	34	IIA	RB	2.44E-12	2.77E-12	2.52E-12	1.34E-12	6.95E-13
G05	50	IIR-M	RB	1.42E-12	1.80E-12	2.32E-12	2.44E-12	1.36E-12
G06	67	IIF	RB	1.59E-12	8.51E-13	4.48E-13	2.73E-13	1.49E-13
G07	48	IIR-M	RB	2.24E-12	1.58E-12	1.95E-12	2.03E-12	1.20E-12
G08	38	IIA	CS	9.93E-13	9.44E-13	1.21E-12	1.58E-12	1.62E-12
G09	39	IIA	CS	9.70E-13	8.61E-13	1.02E-12	1.34E-12	1.42E-12
G10	40	IIA	CS	1.14E-12	1.03E-12	1.28E-12	1.61E-12	1.50E-12
G11	46	IIR	RB	2.40E-12	1.35E-12	1.63E-12	1.76E-12	1.14E-12
G12	58	IIR-M	RB	1.81E-12	1.84E-12	2.46E-12	2.75E-12	1.35E-12
G13	43	IIR	RB	1.78E-12	1.34E-12	1.70E-12	1.82E-12	1.06E-12
G15	55	IIR-M	RB	2.43E-12	1.80E-12	1.77E-12	1.81E-12	1.14E-12
G17	53	IIR-M	RB	1.54E-12	1.73E-12	2.40E-12	2.57E-12	1.35E-12
G18	54	IIR	RB	2.24E-12	1.60E-12	1.78E-12	1.82E-12	1.17E-12
G19	59	IIR	RB	1.66E-12	1.25E-12	1.55E-12	1.53E-12	8.68E-13
G20	51	IIR	RB	1.86E-12	1.70E-12	1.66E-12	1.75E-12	1.17E-12
G23	60	IIR	RB	1.70E-12	1.78E-12	1.78E-12	1.75E-12	1.14E-12
G24	65	IIF	CS	3.68E-12	4.42E-12	3.78E-12	2.42E-12	1.38E-12
G25	62	IIF	RB	1.30E-12	8.91E-13	4.94E-13	2.06E-13	7.89E-14
G26	26	IIA	RB	2.85E-12	2.49E-12	9.42E-13	5.06E-13	3.17E-13
G27	66	IIF	RB	1.74E-12	1.17E-12	6.60E-13	3.85E-13	2.37E-13
G28	44	IIR	RB	2.41E-12	1.31E-12	1.63E-12	1.76E-12	1.10E-12
G29	57	IIR-M	RB	1.50E-12	1.44E-12	1.70E-12	1.82E-12	1.01E-12
G30	64	IIF	RB	1.67E-12	9.07E-13	5.26E-13	3.22E-13	-

Table B.2: Clock MAD values for averaging intervals of $\tau = 1$, 3, 10, 30, and 100 seconds for satellites collected from the GLONASS constellation using 1WCP.

ALM	SVID	Series	Clock	Averaging Intervals of MAD				
				1s	3s	10s	30s	100s
R01	730	M	CS	3.12E-12	5.75E-12	2.98E-12	1.56E-12	9.64E-13
R02	747	M	CS	9.10E-12	7.20E-12	1.77E-12	1.01E-12	5.81E-13
R03	744	M	CS	5.39E-12	6.19E-12	1.95E-12	1.11E-12	6.85E-13
R04	742	M	CS	7.72E-12	6.95E-12	2.23E-12	1.23E-12	6.99E-13
R05	734	M	CS	4.60E-12	7.48E-13	3.13E-12	1.60E-12	9.14E-13
R06	733	M	CS	3.48E-12	6.86E-12	4.83E-12	2.50E-12	1.41E-12
R07	745	M	CS	7.37E-12	9.96E-12	3.33E-12	1.78E-12	1.03E-12
R08	743	M	CS	7.46E-12	5.27E-12	1.80E-12	1.02E-12	5.56E-13
R09	736	M	CS	6.70E-12	9.01E-12	3.05E-12	1.66E-12	9.15E-13
R10	717	M	CS	2.32E-12	4.41E-12	3.87E-12	2.00E-12	1.10E-12
R11	723	M	CS	2.17E-12	3.97E-12	3.20E-12	1.63E-12	8.69E-13
R12	737	M	CS	1.05E-11	6.81E-12	2.33E-12	1.28E-12	7.06E-13
R13	721	M	CS	3.63E-12	6.85E-12	3.74E-12	1.91E-12	1.08E-12
R14	715	M	CS	2.49E-12	4.03E-12	2.12E-12	1.08E-12	6.15E-13
R15	716	M	CS	1.99E-12	3.77E-12	5.42E-12	3.73E-12	2.11E-12
R16	738	M	CS	1.05E-11	8.40E-12	2.78E-12	1.57E-12	8.61E-13
R17	746	M	CS	7.20E-12	6.85E-12	2.19E-12	1.17E-12	6.51E-13
R18	724	M	CS	2.08E-12	3.85E-12	2.71E-12	1.35E-12	7.54E-13
R19	720	M	CS	3.27E-12	5.07E-12	2.16E-12	1.13E-12	6.46E-13
R20	719	M	CS	3.80E-12	5.50E-12	1.99E-12	1.07E-12	6.08E-13
R21	725	M	CS	2.85E-12	5.54E-12	4.52E-12	2.31E-12	1.26E-12
R22	731	M	CS	2.90E-12	4.84E-12	2.55E-12	1.31E-12	7.48E-13
R23	732	M	CS	3.86E-12	6.67E-12	3.17E-12	1.65E-12	9.22E-13
R24	735	M	CS	4.09E-12	6.57E-12	2.53E-12	1.36E-12	7.78E-13

Table B.3: Clock MAD values for averaging intervals of $\tau = 1$, 3, 10, 30, and 100 seconds for satellites collected from the Galileo constellation using 1WCP.

ID	SVID	Series	Clock	Averaging Intervals of MAD				
				1s	3s	10s	30s	100s
E11	101	IOV	PHM	1.48E-12	5.52E-13	2.39E-13	1.33E-13	6.92E-14
E12	102	IOV	PHM	9.14E-13	3.84E-13	1.99E-13	1.23E-13	6.74E-14
E19	103	IOV	PHM	1.09E-12	5.74E-13	4.75E-13	3.80E-13	3.03E-13
E20	104	IOV	RB	2.05E-12	1.20E-12	7.10E-13	4.08E-13	-

Table B.4: Clock MAD values for averaging intervals of $\tau = 1$, 3, 10, 30, and 100 seconds for satellites collected from the BeiDou constellation using 1WCP.

ID	SVID	Series	Clock	Averaging Intervals of MAD				
				1s	3s	10s	30s	100s
C11	M3	MEO	RB	2.52E-12	1.58E-12	8.34E-13	4.91E-13	2.98E-13
C12	M4	MEO	RB	2.48E-12	1.62E-12	8.11E-13	4.62E-13	2.69E-13
C13	M5	MEO	RB	3.68E-12	2.31E-12	1.18E-12	6.79E-13	4.02E-13
C14	M6	MEO	RB	1.72E-12	1.05E-12	6.91E-13	5.60E-13	4.30E-13

Appendix C

SUB-SECOND GPS CLOCK ANALYSIS

A GNSS carrier phase data set was collected and analyzed from the radio telescope in Green Bank, West Virginia. The large antenna provided high enough gain to isolate the GNSS clock at a sub-second intervals, although the analysis is not at the level of the longer term studies described in Chapter 7. The development shown here proposes a method to isolate the variation from the GNSS satellite clock in the carrier phase of the signal received at the ground. Additional data collections at facilities with high-gain antennas and precise receiver clocks could provide further insight into the sub-second stability of the current and future GNSS satellites.

C.1   Derivation

C.1.1   Carrier Tracking Error

The main sources of error in a GNSS receiver PLL are phase jitter and dynamic stress error, which are products of thermal and oscillator error [46]. The error due to thermal noise for an arctangent PLL is given as

$$\sigma_{\Delta\phi} = \sqrt{\frac{BW}{C/N_0}\left(1 + \frac{1}{2TC/N_0}\right)} \text{ (rad)} \tag{C.1}$$

where BW is the loop bandwidth (in Hz), T is the integration time (in seconds), and C/N_0 is the carrier-to-noise ratio, which is usually given in dB-Hz, but needs to be converted to non-decibel units for this calculation.

As a back of the envelope calculation for comparison, if an assumption of 1 ms integration time is made (a good worst-case scenario), with a PLL bandwidth of 100 Hz and a C/N_0 of 40 dB-Hz, then the carrier tracking error due to the thermal noise is calculated as the following.

$$\sigma_{\Delta\phi} = \sqrt{\frac{100}{10000}\left(1 + \frac{1}{2 \cdot 0.001 \cdot 10000}\right)} = 0.1025 \text{ rad} = 3.1 \text{ mm} = 1.0336 \times 10^{-11} \text{ seconds} \quad \text{(C.2)}$$

Because the focus of this analysis is phase error at such short time intervals, the dominant error source is expected to be thermal noise. If the phase error behaves as white phase noise, then the carrier tracking error given by Equation C.1 and the AD, $\sigma_y(\tau)$, should produce similar results. One would expect a phase tracking error of approximately 10^{-11} seconds at $\tau = 1$ second for a signal with $C/N_0 = 40$ dB-Hz. If a constant τ^{-1} slope for white phase noise is assumed, the error at $\tau = 0.01$ seconds would approximately be 10^{-9} seconds. If a MAD is used, then the slope follows $\tau^{-3/2}$, and the error at $\tau = 0.01$ seconds would be closer to 10^{-8} seconds.

C.1.2 Power Law Domain Conversions

The following analysis is derived from Riley (2008) [69]. For a white phase power law noise model, the following relationship holds for the conversion from the power spectral density (PSD) to the Allan variance.

$$\sigma_y^2(\tau) = \frac{3f_h}{4\pi^2}f^{-2}S_y(f)\tau^{-2} = \frac{3f_h S_y(f)}{4\pi^2 f^2 \tau^2} \quad \text{(C.3)}$$

where f_h is the high corner frequency and $S_y(f)$ is the power spectral density of the fractional frequency fluctuations in the frequency domain. The following relationships allow for the transformation to a phase noise power spectral density.

$$S_y(f) = (2\pi f)^2 S_z(f) \quad \text{(C.4)}$$

$$S_\phi(f) = (2\pi\nu_0)^2 S_z(f) \quad \text{(C.5)}$$

$$S_y(f) = \frac{f^2}{\nu_0^2}S_\phi(f) \quad \text{(C.6)}$$

The AD equation, in terms of the power spectral density of the phase noise, is then

$$\sigma_y(\tau) = \frac{\sqrt{3f_h \frac{f^2}{\nu_0^2}S_\phi(f)}}{2\pi\tau} = \frac{\sqrt{3f_h S_\phi(f)}}{2\pi\nu_0\tau} \quad \text{(C.7)}$$

where ν_0 is the carrier frequency and τ is the averaging interval for the AD calculation. The high corner frequency, f_h is taken to be the PLL bandwidth. The phase noise spectral density, S_ϕ, is the inverse of the power SNR at 1 Hz (SNR_0). S_ϕ will vary as a function of frequency.

As additional means to verify the derivation shown in Equation C.7, the unit conversion is evaluated. f_h has units of Hz, S_ϕ has units of squared radians per Hz, and the denominator is in radian-Hz-seconds. The units cancel, leaving a unitless quantity, which agrees with the dimensionality of the AD.

Using Equation C.7, a PLL bandwidth of 100 Hz, and a signal with C/N_0 of 40 dB-Hz, the resulting phase error in terms of the AD is $\sigma_y(\tau = 1 \text{ second}) = 1.75 \times 10^{-11}$. This is slightly higher than the carrier tracking error, $\sigma_{\Delta\phi}$, calculated earlier, but is on the same order of magnitude. At $\tau = 0.01$ seconds, if assuming white phase noise, the AD would be $\sigma_y(\tau = 0.01 \text{ seconds}) = 1.75 \times 10^{-9}$.

C.1.3   Modified Allan Deviation

As described in Section 6.2.1, the MAD optimizes the software bandwidth coinciding to the sample interval, allowing for differentiation between white and flicker phase noises at short time intervals. The MAD can also be related to power law for white phase noise modulation, as shown in the following relationship.

$$\sigma^2_{y,\text{MOD}}(\tau) = h_2 \frac{3 f_h}{(2\pi)^2 n \tau^2} \tag{C.8}$$

where $h_2 = \frac{S_y(f)}{f^2}$. If the phase power spectral density function is plugged in, Equation C.8 can be simplified to

$$\sigma^2_{y,\text{MOD}}(\tau) = \frac{\sqrt{3 f_h S_\phi(f)}}{2\pi \tau \nu_0 \sqrt{n}} \tag{C.9}$$

Equation C.9 differs from C.7 by a factor of $\sqrt{n}$ in the denominator. Using Equation C.9, various values of SNR_0 can be used to derive the theoretical MAD curves associated with the white phase noise modulation. If a PLL bandwidth of 100 Hz is assumed, the modified and traditional AD values should be equivalent at $\tau = 100$ seconds. At $\tau = 1$ second and a $C/N_0 = 40$ dB-Hz, however, the

MAD deviates and is $\sigma_{y,\text{MOD}}(\tau) = 1.75 \times 10^{-12}$.

C.2   Theoretical vs. Measured Results

High-rate GPS data sets were taken with a 100-meter diameter radio telescope in Green Bank, West Virginia in 2005 and 2006. The data sets were short (approximately 5-6 seconds in length), and contain L1 data from several GPS satellites. The data were processed with a software receiver developed at CU. The raw IF data for PRN 24 (SVN 24) were transformed into carrier phase observations at a sampling rate of 1 kHz with PLL bandwidth of 100 Hz. The L1 carrier phase measurements for PRN 24 are modeled with the carrier phase equation, as follows.

$$\lambda_{L1}\phi_{24} = R + c(\delta t_u - \delta t^{24}) - I_{L1} + T + N + M_{L1} + \epsilon_{L1} \tag{C.10}$$

The term of interest in Equation C.10 is the satellite clock, δt^{24}. Because of the length of the data set, an assumption is made that a simple polynomial fit to the carrier phase data will remove the majority of the non-clock components to the variation of the signal (range (R), ionosphere (I_{L1}), troposphere (T), and multipath (M_{L1})). Delporte et al. (2010) shows good agreement between the polynomial fit and full-model residual methods for short time intervals [18]. Over time intervals of 5-6 seconds, these terms are typically constant, given a high elevation satellite with strong signal SNR. The polynomial detrending will remove the low frequency effects, leaving behind the combination of the receiver and satellite clock error.

To better analyze the high frequency behavior (averaging intervals between 0.01 and 0.1 seconds), the MAD is used. Before applying the MAD to the detrended carrier phase observations, the signal from PRN 24 was intentionally degraded to different levels of C/N_0. The initial C/N_0 of the signal from PRN 24 was calculated to be approximately 99 dB-Hz by the VSM. However, a link budget analysis of the transmitted signal, environment, and gain of the large antenna placed that estimate at 9 dB higher, around 108 dB-Hz. Limitations of the dynamic range for the C/N_0 estimation are suspected for the low SNR estimation. After estimation of the initial signal power, white Gaussian noise was digitally added to the signal at different amplitudes to reduce the C/N_0

to values of 104, 99, 89, 69, and 49 dB-Hz.

The MAD for averaging intervals of $\tau = 0.01 - 0.1$ seconds was applied to the original and degraded signals, whose results are shown in Figure C.1. Also plotted in corresponding colors but dashed lines, are the theoretical MAD values as calculated by Equation C.9 for each of the various C/N_0 values.
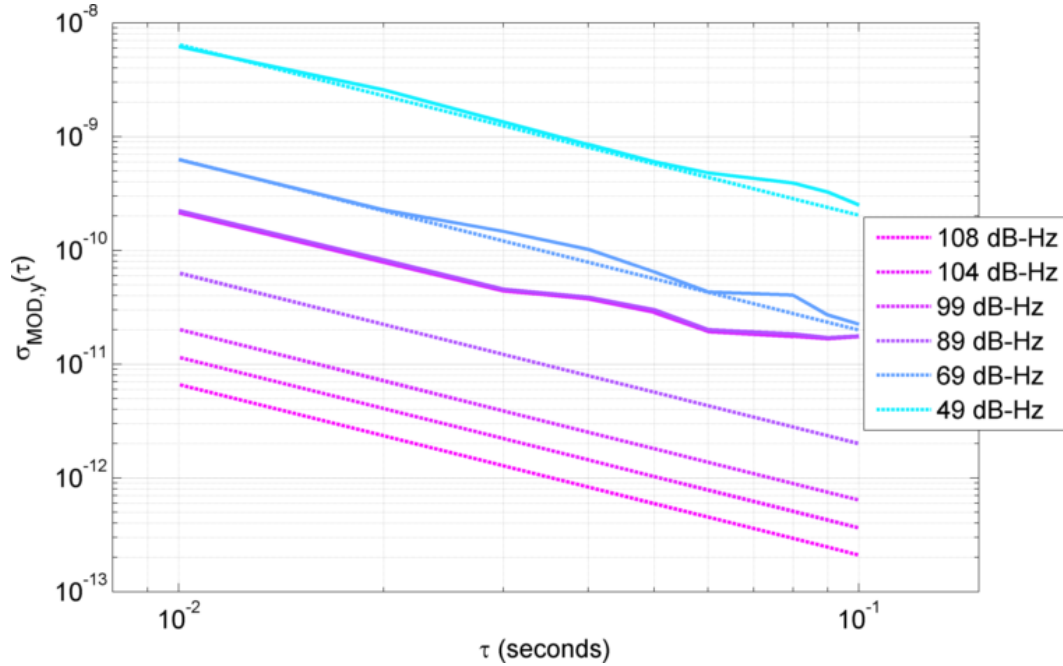

Figure C.1: MAD values for a high SNR signal from the radio telescope at Green Bank, West Virginia. Measured values of the MAD are depicted as solid lines, while the theoretical values derived from the C/N_0 of the signal are represented by dashed lines.

This figure shows that some lower level of stability is reached that no longer depends on the power of the received signal. For the noisier signals at 49 and 69 dB-Hz, the theoretical and measured values show good agreement. Then for signals with C/N_0 values higher than approximately 75 dB-Hz, the measured variation no longer decreases as the thermal noise predicts. This result may indicate that some lower stability bound is found for the combination of clocks (both the PRN 24 atomic reference and the external rubidium used at the ground receiver). Sub-second AD analyses are rarely shown in the literature, as it is difficult to isolate the clock contribution to

the variation of the signal without signal power levels of at least 70 dB-Hz. Typical values for a ground-based COTS system with geodetic antenna range between 45-55 dB-Hz. Therefore, a signal gain of at least 15 dB is needed for sub-second clock analysis from a ground-based receiver. This can most easily be provided by a high-gain antenna, such as the radio telescopes available at Green Bank.